

**MINISTRY OF EDUCATION AND TRAINING
QUY NHON UNIVERSITY**

NGUYEN NGOC TRI

**STUDY ON THE ADSORPTION ABILITY OF ORGANIC
MOLECULES ON TiO₂ AND CLAY MINERAL MATERIALS USING
COMPUTATIONAL CHEMISTRY METHODS**

DOCTORAL DISSERTATION

BINH DINH - 2021

**MINISTRY OF EDUCATION AND TRAINING
QUY NHON UNIVERSITY**

Nguyen Ngoc Tri

**STUDY ON THE ADSORPTION ABILITY OF ORGANIC
MOLECULES ON TiO₂ AND CLAY MINERAL MATERIALS USING
COMPUTATIONAL CHEMISTRY METHODS**

Major : Physical and Theoretical Chemistry

Code No. : 9.44.01.19

Reviewer 1 : Assoc. Prof. Pham Tran Nguyen Nguyen

Reviewer 2 : Assoc. Prof. Tran Van Tan

Reviewer 3 : Assoc. Prof. Pham Vu Nhat

Supervisors:

1. Assoc. Prof. Nguyen Tien Trung

2. Prof. Minh Tho Nguyen

BINH DINH - 2021

Declaration

This thesis was completed at the Department of Chemistry, Faculty of Natural Sciences, Quy Nhon University (QNU) under the supervision of Assoc. Prof. Nguyen Tien Trung (QNU, Vietnam) and Prof. Minh Tho Nguyen (KU Leuven, Belgium). I hereby declare that the results presented in this thesis are new and original. While most of them were published in peer-reviewed journals, the other part has not been published elsewhere.

Binh Dinh, 2021

Supervisors

Ph.D. student

Assoc. Prof. Nguyen Tien Trung

Prof. Minh Tho Nguyen

Nguyen Ngoc Tri

Acknowledgements

First of all, I would like to express my sincerest thanks to the supervisors, Assoc. Prof. Nguyen Tien Trung and Prof. Minh Tho Nguyen, for their patient guidance, genius support, and warm encouragement. I would also like to thank them for their valuable comments, suggestions, and corrections. In fact, without their help, this thesis could not have been achievable.

I am grateful to all LCCM members for their help and valuable discussion during my research time. I am very thankful to my friend, Dai Q. Ho, for his help during my graduate study. I would like to thank Prof. A.J.P. Carvalho, University of Evora, Portugal, for his valuable comments, revisions, and computing facilities.

I am thankful to Quy Nhon University and KU Leuven for providing me with such a great opportunity to pursue my doctoral program. My thanks are extended to all staff at the Faculty of Natural Sciences, Quy Nhon University and the Department of Chemistry, KU Leuven for their help and supports during my PhD time. My acknowledgements also go to my friends and colleagues for their time and friendship.

Furthermore, I would also like to thank the VLIR-TEAM project awarded to Quy Nhon University with Grant number ZEIN2016PR431 (2016-2020) and the VINIF scholarship with code number VINIF.2019.TS.73 for the financial supports during my doctoral studies.

Lastly and most importantly, I am forever grateful to my family for all their love and support through the numerous difficulties I have been facing.

Binh Dinh, 2021
Nguyen Ngoc Tri

TABLE OF CONTENTS

List of Symbols and Notations

List of Figures

List of Tables

INTRODUCTION	1
1. Motivation	1
2. Research purpose	3
3. Object and scope of this study	3
4. Research contents.....	4
5. Methodology	4
6. Novelty, scientific and practical significance	5
PART 1. DISSERTATION OVERVIEW	7
1. Organic pollutants and antibiotics residues in wastewaters.....	7
2. TiO ₂ nanomaterial and its applications	8
3. Clay minerals and their applications in the treatment of pollutants.....	10
4. Investigations on materials surfaces using computational chemistry	12
PART 2. THEORETICAL BACKGROUND AND COMPUTATIONAL METHODS	13
1. Quantum chemical approaches	13
1.1. Schrödinger equations.....	13
1.2. The Born - Oppenheimer approximation and Pauli's exclusion principle	15
1.2.1. Born – Oppenheimer approximation	15
1.2.2. Pauli's exclusion principle.....	15
1.3. The variational principle	16
1.4. Basis sets	17
1.4.1. Slater and Gaussian orbitals.....	17
1.4.2. Some popular basis sets	18
1.5. Hartree-Fock approximation	19

1.6. Density functional theory	20
1.6.1. <i>The Hohenberg-Kohn theorem</i>	20
1.6.2. <i>Kohn-Sham equations</i>	21
1.6.3. <i>Local density approximation</i>	22
1.6.4. <i>General gradient approximation</i>	23
1.6.5. <i>Hybrid functionals</i>	24
1.6.6. <i>Van der Waals functionals</i>	25
1.7. Pseudopotential and plane-wave methods	26
1.8. Atoms In Molecules and Natural Bond Orbitals approaches	29
1.8.1. <i>Atoms In Molecules analysis</i>	29
1.8.2. <i>Natural Bond Orbitals analysis</i>	31
2. Computational methods	33
2.1. TiO ₂ systems	33
2.2. Clay mineral systems	34
2.2.1. <i>Adsorption of organic molecules on kaolinite surfaces</i>	34
2.2.2. <i>Adsorption of antibiotics on vermiculite surface</i>	35
2.3. Quantum chemical analyses	36
PART 3. RESULTS AND DISCUSSION	38
CHAPTER 1. ADSORPTION OF ORGANIC MOLECULES ON MATERIALS SURFACES	38
1.1. Adsorption of organic molecules on rutile-TiO ₂ (110) surface	38
1.1.1. <i>Optimized structures</i>	38
1.1.2. <i>Energetic aspects</i>	40
1.1.3. <i>The quantum chemical analysis for the interactions on surface</i>	42
1.1.4. <i>Summary</i>	44
1.2. Adsorption of benzene derivatives on rutile-TiO ₂ (110) and anatase-TiO ₂ (101) surfaces	44
1.2.1. <i>Geometrical structures</i>	44
1.2.2. <i>Energetic aspects of the adsorption process</i>	48

1.2.3. Formation and role of intermolecular interactions	50
1.2.4. Summary.....	56
1.3. Adsorption of benzene derivatives on kaolinite (001) surface	57
1.3.1. Optimized geometries.....	57
1.3.2. Energetic aspects of the adsorption process.....	59
1.3.3. Formation and role of intermolecular interactions	60
1.3.4. Summary.....	64
1.4. Adsorption of benzene derivatives on a K ⁺ -supported kaolinite (001) surface	65
1.4.1. Stable complexes	65
1.4.2. Adsorption energy	66
1.4.3. AIM and NBO analyses	67
1.4.4. Summary.....	70
CHAPTER 2. ADSORPTION OF ANTIBIOTIC MOLECULES ON TiO₂ AND VERMICULITE SURFACES	71
2.1. Adsorption of enrofloxacin molecule on rutile-TiO ₂ (110) surface.....	71
2.1.1. Stable structures.....	71
2.1.2. Energetic aspects of the adsorption process.....	73
2.1.3. Characteristics of interactions on the surface	74
2.1.4. Summary.....	76
2.2. Adsorption of ampicillin, amoxicillin, and tetracycline molecules on rutile-TiO ₂ (110) surface.....	76
2.2.1. Stable complexes	76
2.2.2. Energetic aspects of the adsorption process.....	79
2.2.3. Characteristic properties of intermolecular interactions	82
2.2.4. Summary.....	86
2.3. Adsorption of ampicillin and amoxicillin molecules on anatase-TiO ₂ (101) surface	86
2.3.1. Stable structures.....	86
2.3.2. Adsorption energy	89

2.3.3. <i>AIM and NBO analyses</i>	90
2.3.4. <i>Summary</i>	92
2.4. Adsorption of chloramphenicol molecule on a vermiculite surface	93
2.4.1. <i>Geometrical structures</i>	93
2.4.2. <i>Adsorption, interaction, and deformation energies</i>	95
2.4.3. <i>Characteristics of stable interactions upon adsorption process</i>	97
2.4.4. <i>Summary</i>	102
2.5. Adsorption of β -lactam antibiotics on vermiculite surface	103
2.5.1. <i>Stable structures</i>	103
2.5.2. <i>Energetic aspects of the adsorption process</i>	107
2.5.3. <i>Existence and role of different interactions upon complexation</i>	110
2.5.4. <i>Summary</i>	116
CONCLUSIONS AND OUTLOOK	117
1. Conclusions	117
2. Outlook	119
LIST OF PUBLICATIONS CONTRIBUTES TO THIS THESIS	120
REFERENCES	121
<i>Appendix</i>	

LIST OF SYMBOLS AND NOTATIONS

<i>Symbol</i>	<i>Description</i>
$\nabla^2(\rho(\mathbf{r}))$: Laplacian of electron density
AIM	: Atoms in Molecules theory
AP	: Ampicillin
a-TiO ₂	: Anatase-TiO ₂ (101) surface
AX	: Amoxicillin
BCP	: Bond critical point
BP	: Benzylpenicillin
CP	: Chloramphenicol
d	: Distance of contact
DFT	: Density Functional Theory
DPE	: Deprotonation enthalpy
E _{ads}	: Adsorption energy
E _B	: Hydrogen bond energy
E _{def-mol}	: Deformation energy for molecules
E _{def-surf}	: Deformation energy for surfaces
EDT	: Electron density transfer
E _{int}	: Interaction energy
ER	: Enrofloxacin
H(r)	: Total of electron density energy
H-slab	: Hydrogen-rich facet of kaolinite (kaolinite (001) surface)
K ⁺ -slab	: K ⁺ -supported kaolinite (001) surface
MEP	: Molecular Electrostatic Potential
NBO	: Natural Bond Orbitals
O-slab	: Oxygen-rich facet of kaolinite (kaolinite (00 $\bar{1}$) surface)
PA	: Proton affinity
PBE	: Perdew–Burke–Ernzerhof (density functional)

q	:	Net charge at atom
r-TiO ₂	:	Rutile-TiO ₂ (110) surface
TC	:	Tetracycline
VASP	:	Vienna Ab initio Simulation Package
vdW	:	Van der Waals
α	:	Bond angle
Δr	:	Change of bond length
$\rho(r)$:	Electron density (at BCP)

LIST OF FIGURES

	Page
Figure 1. The radial part of the 3s atomic orbit of the Na atom	27
Figure 2. Schematic drawing of a 3s-derived Bloch function of one-dimensional crystals of Na atoms	27
Figure 3. The graph shows the first random substitution for two alkali metals Na, Cs according to Hellmann	28
Figure 4. The slab models of rutile-TiO ₂ (110) and anatase-TiO ₂ (101) surfaces	33
Figure 5. The structure of kaolinite surfaces	35
Figure 6. The model slab of vermiculite surface (red, yellow, grey, pink, and white colors displayed for O, Mg, Si, Al, and H atoms, respectively)	36
Figure 1.1. Stable complexes for the adsorption of organic molecules on rutile-TiO ₂ (110) surface	38
Figure 1.2. The charge density between adsorbent and adsorbates in stable complexes	42
Figure 1.3. The topological analysis for the first-layered structures	42
Figure 1.4. Stable complexes of adsorption of benzene derivatives on rutile-TiO ₂ (110) surface	45
Figure 1.5. Stable structures of adsorption of benzene derivatives on anatase-TiO ₂ (101) surface	47
Figure 1.6. MEP maps of benzene derivatives (isovalue = 0.02 au, charge region taken in the range of $2 \cdot 10^{-3}$ to 0.15 e)	50
Figure 1.7. Topological geometry of the first-layered structures of the most stable complexes for rutile systems	53
Figure 1.8. Topological geometry of the first-layered structures of the most stable complexes for anatase systems	53
Figure 1.9. EDT maps of investigated structures for rutile system	53
Figure 1.10. EDT maps of investigated structures for anatase system	53

Figure 1.11. Stable structures of adsorption of derivatives on H-slab	57
Figure 1.12. Topological geometry of the most stable complexes for adsorption of organic molecules on H-slab	62
Figure 1.13. Schematic of total electron density of complexes at the B3LYP/6-31+G(d,p) level	64
Figure 1.14. The stable complexes of molecules adsorption on K ⁺ -slab	65
Figure 1.15. The topological geometries of the stable complexes for K ⁺ -slab systems	68
Figure 1.16. The EDT maps of the stable complexes for K ⁺ -slab systems	68
Figure 2.1. Optimized structures of enrofloxacin, rutile-TiO ₂ (110) surface, and two stable adsorption configurations	71
Figure 2.2. The topology and electron density transfer maps for the first-layered structures of ER1 and ER2 at the B3LYP/6-31+G(d, p) level	75
Figure 2.3. Stable complexes for adsorption of antibiotic molecules on rutile-TiO ₂ (110) surface	77
Figure 2.4. DOS plot of rutile-TiO ₂ (110) surface and HOMO, LUMO levels of adsorbed antibiotic molecules	84
Figure 2.5. a) Topological critical points and b) electronic charge density transfer of the most stable complexes	85
Figure 2.6. Optimized structures of anatase-TiO ₂ (101) surface and ampicillin, amoxicillin molecules	87
Figure 2.7. The optimized structures of ampicillin, amoxicillin adsorbed on anatase-TiO ₂ (101) surface	87
Figure 2.8. The topological geometries and EDT maps of the first-layered structures	90
Figure 2.9. Optimized structures of a) vermiculite surface, and b) chloramphenicol molecule, and c) the MEP map of chloramphenicol (electron density of 0.02 au, from -5.10^{-5} to 0.15 au region).	93

Figure 2.10. Stable adsorption configurations of chloramphenicol on the vermiculite surface	94
Figure 2.11. Topological features for the first layered structures of complexes	99
Figure 2.12. Total electron density distributions of the first-layered structures	101
Figure 2.13. Stable complexes of adsorption of AP, AX and BP on a vermiculite surface	104
Figure 2.14. Molecular electrostatic potential (MEP) of free antibiotic molecules	110
Figure 2.15. Topological features for the most stable adsorption configurations	112
Figure 2.16. Total electron density maps of most stable complexes	115

LIST OF TABLES

	Page
Table 1.1. Charge distribution in molecules at the B3LYP/6-31+G(d,p) level	38
Table 1.2. Some selected parameters of stable complexes at PBE functional (distance (r) in Å; angle (α) in degree)	39
Table 1.3. Adsorption, interaction, and deformation energies (all in kcal.mol ⁻¹) for the adsorption processes on rutile-TiO ₂ (110) surface	40
Table 1.4. The characteristic parameters for topological analysis (all in au)	43
Table 1.5. Some selected parameters of molecules and TiO ₂ surfaces	45
Table 1.6. Interaction distance (d, Å), bond angle (α , °), and changes in length of bonds (Δr , Å) following the adsorption process for rutile systems	46
Table 1.7. Distance of intermolecular interactions (d, Å), bonding angle (α , °), and changes of bond length (Δr , Å) upon adsorption process for anatase systems	46
Table 1.8. Adsorption, interaction, and deformation energies of adsorption of benzene derivatives on rutile-TiO ₂ (110) surface (all in kcal.mol ⁻¹)	48
Table 1.9. Energetic aspects of adsorption of benzene derivatives on anatase-TiO ₂ (101) surface (all in kcal.mol ⁻¹)	49
Table 1.10. NBO charges at atoms in functional groups involved in interactions in complexes	51
Table 1.11. Proton affinity (PA) at O and N atoms and deprotonation enthalpy (DPE) of O-H and N-H bonds in functional groups and C-H bonds in the benzene ring of derivatives (in kcal.mol ⁻¹)	52
Table 1.12. Characteristic parameters for topological geometry ($\rho(r)$, $\nabla^2(\rho(r))$, H(r), in au), EDT (in e) for rutile systems	54
Table 1.13. Characteristic parameters for topological geometry ($\rho(r)$, $\nabla^2(\rho(r))$, H(r), in au), EDT (in e) for anatase systems	55

Table 1.14. Distances of intermolecular contacts (d), changes in the bond lengths (Δr) involved in interactions in complexes (all in Å)	58
Table 1.15. Energetic parameters of complexes, molecules and surface upon adsorption processes (in kcal.mol ⁻¹)	59
Table 1.16. Characteristics of topological geometries ($\rho(r)$, $\nabla^2\rho(r)$, $H(r)$, in au) and EDT (in e) at the B3LYP/6-31+G(d,p) level	62
Table 1.17. The adsorption energy of the stable complexes (in kcal.mol ⁻¹)	66
Table 1.18. The characteristics for topology analysis and total of electron density transfer (EDT) for K ⁺ -slab systems at the B3LYP/6-31+G(d,p) level	69
Table 2.1. Some selected parameters for two stable complexes using PBE functional	72
Table 2.2. Energies for adsorption of Enrofloxacin on rutile-TiO ₂ (110) surface (in kcal.mol ⁻¹)	73
Table 2.3. The topological analysis and EDT of investigated structures at the B3LYP/6-31+G(d, p) level	75
Table 2.4. Some selected parameters for stable adsorption configurations	78
Table 2.5. Energies for adsorption processes using both PBE and optPBE-vdW functionals (kcal.mol ⁻¹) ^{a)}	80
Table 2.6. Some characteristic parameters of the stable complexes	88
Table 2.7. Adsorption energy (E_{ads} , kcal.mol ⁻¹) of stable complexes	89
Table 2.8. The topological analysis ($\rho(r)$, $\nabla^2(\rho(r))$, $H(r)$, au), electron density transfers (EDT, e), and hyper-conjugation energies (E^2 , kcal.mol ⁻¹)	91
Table 2.9. Energetic aspects of adsorption of chloramphenicol on the vermiculite surface (all in kcal.mol ⁻¹)	95
Table 2.10. Proton affinity (PA) at O and Cl atoms and vertical deprotonation enthalpy (DPE) of O-H and C-H bonds of chloramphenicol molecule (in kcal.mol ⁻¹)	98

Table 2.11. Topological analysis at the bond critical points (BCPs) of intermolecular contacts (in au), hydrogen bond energy (in kcal.mol ⁻¹) and total electron density transfer (EDT, in e) of complexes	100
Table 2.12. Some selected parameters for optimized complexes shown in Figure 2.13 (bond distances in Angstrom (Å) and angles in degree (°), values from DFT computations) *)	105
Table 2.13. Adsorption energies (E _{ads}), interaction energies (E _{int}) and deformation energies for antibiotics and vermiculite surface (E _{def-mol} , E _{def-surf}) (in kcal.mol ⁻¹)	107
Table 2.14. Proton affinity (PA) at atoms or π-ring and deprotonation enthalpy (DPE) of O(N,C)-H bonds of molecules (kcal.mol ⁻¹ , obtained from B3LYP/6-311++G(d,p) computations)*)	111
Table 2.15. Topological analysis (ρ(r), ∇ ² (ρ(r)), au) at the bond critical points (BCPs), hydrogen bond energy (E _B , kcal.mol ⁻¹) and total electron density transfer (EDT, e) of most stable complexes at the B3LYP/6-31+G(d,p) level	113

INTRODUCTION

1. Motivation

Scientists have constantly been paying considerable attention to problems related to environmental pollution in which the pollution of water resources remains a painful global issue [51], [52]. The development of several large-scale industries leads to a continuous release of toxic compounds into wastewater. They are present in the environments, gradually accumulated in a significant concentration, and hard to be biodegraded. Of the pollutants, the derivatives of phenol, carboxylic acids, and medicinal products are directly and dangerously affecting the organisms' lives [5], [86]. In addition, some antibiotics which are extensively used in shrimp farming and released in wastewater were found to induce negative effects on both environments and living organisms [5], [51], [52], [13]. Over the past few decades, experimental and theoretical studies have been reported on advanced materials and nanomaterials with high applicability in the fields of science, technology, and environments. Among nanomaterials, TiO_2 has been known as an essential semiconductor and is widely applied in various fields of energy and health care [32], [43], [121]. In addition, solid TiO_2 is extensively used in the photocatalysis, adsorption, and decomposition of organic compounds due to its unique surface properties. The processes usually take place on the TiO_2 surfaces and depend on the nature, concentration of the substance, and the material phases [29], [32], [121], [129]. Notably, the interaction of organic molecules on surfaces of TiO_2 was observed in the initial steps of catalysis, sensors, drug transmission processes [30], [118], [130]... However, research on the fundamental nature and role of adsorptive interactions and the mechanism of processes that occurred on TiO_2 surfaces has not been investigated in detail yet.

Many previous reports focused on elimination of harmful substances that cause negative effects on the environment by using nanomaterials or advanced technologies. Several physical, chemical, and biological solutions were proposed to achieve the necessary efficiency. Some recent materials have been examined for the

adsorption and treatment capacity of organic pollutants, including activated carbon, filter membranes, and advanced oxidations. The adsorption of organic molecules onto surfaces of materials is a suitable way for removing amounts of pollutants from a specific environment, including antibiotics presented in wastewaters [32], [121], [122], [136]. However, these approaches require high cost and are too sophisticated to use [4], [5], [94], [140]. Thus, several studies have been performed to find out low-cost, environmentally friendly, and highly effective materials to remove polluted compounds from the environment.

Of the various available materials, scientists have paid a considerable amount of attention to clay minerals due to their high adsorption capacity, convenient fabrication, and abundant availability in nature and environmental friendliness [19], [38], [46], [70], [91], [100], [113], [131], [142], [145]. Clay mineral materials are characterized by layered structures and a large spatial surface. The addition or replacement of suitable cations on their surfaces could increase the adsorption capacity as well as the removal of toxic substances. Investigations of the adsorption of organic substances and antibiotic residues using clay mineral materials are feasible and have scientific and practical significances. Notably, vermiculite is promised to be a potential candidate to treat persistent organic substances, as it eliminates antibiotic residues in aquatic environments [130]. However, the role of intermolecular interactions and adsorption mechanism on surfaces of minerals has not fully been understood yet.

Furthermore, to examine the application ability of TiO_2 and clay minerals materials for an efficient treatment of organic pollutants, we must understand the origin and role of surface interactions, and the inherent stability of geometrical configurations upon the adsorption process. An insight into the adsorptive interactions of organic molecules onto surfaces of materials such as TiO_2 and clay minerals is the basis for further understanding the interactions between molecules and ions with solid-state surfaces. In recent years, modeling studies using molecular dynamics and quantum chemical methods for the surface science field have

increasingly been carried out thoroughly [37], [78], [81], [92]. The development of modern and high-performance computer systems and efficient computer programs helped scientists significantly in theoretical studies. Many scientists examined the characteristics of TiO_2 and clay minerals materials, including structural and electronic properties, spectroscopy, and surface processes [8], [20], [35], [109]. In this context, theoretical investigations on adsorption and decomposition of organic molecules, incredibly polluted compounds on materials surfaces by using quantum chemical calculations appear to be an approach of choice to understand the surface phenomena.

In conclusion, the present theoretical work finds its importance in the detailed insights and thereby applicability in future experimental studies to find potential and efficient materials for treating organic pollutants. Hence, a theoretical investigation with the title: “*Study on the adsorption ability of organic molecules on TiO_2 and clay mineral materials using computational chemistry methods*” is of high scientific and practical significance. Our calculated results can be served to orient subsequent experimental observations and suggest relevant experiments in Vietnam.

2. Research purpose

The purposes of our theoretical studies can be summarized as follows:

- i) Determination of the stable structures upon the adsorption of organic molecules on different surfaces of TiO_2 and clay minerals;
- ii) Investigation and examination of the adsorption ability of various organic molecules, antibiotics on TiO_2 and clay minerals surfaces;
- iii) Obtention of insights into surface interactions, including their formation and role to the stability of complexes and adsorption processes;
- iv) Evaluation of the use of TiO_2 and clay minerals in future experimental studies on the adsorption and removal of antibiotics and organic pollutants in wastewater.

3. Object and scope of this study

The selected organic molecules and antibiotics include benzene and its derivatives, ampicillin, amoxicillin, benzylpenicillin, enrofloxacin, and tetracycline.

The material surfaces considered in this work include TiO₂ (rutile, anatase), kaolinite, and vermiculite.

The scope of this study is theoretical investigations of the adsorption ability of organic compounds, especially antibiotics, on the surfaces of TiO₂ (anatase, rutile) and clay minerals (kaolinite, vermiculite) by using computational chemistry methods.

4. Research contents

Part 1 gives an overview of previous studies related to this work. A brief description of quantum chemical approaches in solving the Schrodinger equations is shown in the first sections of Part 2. In addition, details on computations for selected systems are also given in the later sections.

Chapters 1 and 2 in Part 3 present the calculations and theoretical results on adsorptions of organic molecules, especially antibiotics on different material surfaces of TiO₂ and clay minerals. More particularly, the work that are carried out include i) Optimization of the structures of organic molecules containing different functional groups (-OH, -COOH, -NH₂, -CHO, -NO₂, and -SO₃H), antibiotics, materials including TiO₂ (rutile-TiO₂ (110) and anatase-TiO₂ (101) surfaces), clay minerals (vermiculite and kaolinite); ii) Design and optimization to obtain stable structures for the adsorption of selected molecules on the surfaces of TiO₂ and clay minerals; iii) Calculations of interesting parameters, energetic parameters following the adsorption of molecules onto TiO₂ and clay minerals surfaces; iv) Analysis and evaluation of the adsorption ability of organic molecules, antibiotics on different surfaces of TiO₂, clay minerals and the role of intermolecular interactions formed on the material surfaces in the investigated systems.

In one of the crucial sections, conclusions and outlook, we summarize the significant results achieved in the present work and give some outlooks for further investigations.

5. Methodology

The density functional theory (DFT) methods with suitable and highly correlated functionals, such as the PBE, optPBE-vdW, vdW-DF-C09 [25], [72],

[104], are considered for the optimization and calculation of characteristic parameters, such as geometrical and electronic structures of organic molecules, antibiotics, materials surfaces as well as stable configurations. The energy aspects, including adsorption, interaction, and deformation energies, are then calculated to evaluate molecules' adsorption ability on material surfaces.

The VASP, GPAW packages [39], [57], [68], and some visualized software such as Gaussview, VESTA, and Material Studio are used to simulate the structures of TiO₂, clay minerals materials, and the configurations formed by the adsorption of molecules onto material surfaces. These programs are also used to calculate energetic values and other parameters. In addition, to consider the formation and role of intermolecular interactions, the calculations on DPE, PA, MEP, topological geometry, and EDT are performed by using Gaussian packages (versions 03 and 09), AIM2000 and NBO 5.G programs [9], [12], [42], [134].

Details of calculations and analyses for the investigated systems are presented in the computational methods section.

6. Novelty, scientific and practical significance

Scientists in Vietnam and worldwide have not yet paid sufficient attention to theoretical studies on the adsorption ability of organic molecules containing benzene rings onto TiO₂ and clay minerals surfaces by using computational chemistry. The present results would first provide us with insights into the adsorption ability of organic molecules and antibiotics on the material surfaces such as TiO₂ and clay minerals. It appears that the results of such research in surface phenomena can be used to put forward solutions for environmental problems. A better understanding of surface interactions is vital for the selection and use of suitable materials to treat organic pollutants. The results of this work lead to a good assessment of the adsorption processes that take place on the surfaces of TiO₂ and clay minerals. This study is also an essential investigation for guiding subsequent experimental studies to remove or decompose pollutants in the environments.

Our present work results give insights into the adsorption ability of organic compounds containing different functional groups such as -OH, -COOH, -CHO, >C=O, NO₂, -NH₂, -SO₃H on the material surfaces. Remarkably, the role and origin of intermolecular interactions contributing to the stability of complexes and the adsorption ability of molecules on the TiO₂ and clay mineral surfaces can be clarified by using quantum chemical methods. The obtained results are valuable references for future studies on treatment of polluted compounds in wastewater sources.

The novelty of this work has been demonstrated by the papers published in peer-reviewed journals such as Surface Science, Chemical Physics Letters, Vietnam Journal of Chemistry, Vietnam Journal of Science and Technology, Vietnam Journal of Catalysis and Adsorption, Quy Nhon University Journal of Science.

PART 1. DISSERTATION OVERVIEW

1. Organic pollutants and antibiotics residues in wastewaters

In recent decades, as environmental pollution has emerged as a global and persistent issue, scientists and policy makers have been paying considerable attention to its consequences [45], [146], [149]. Because compounds containing benzene rings were accumulated for a long time in large amounts as part of the human living conditions [71], it was more and more difficult to completely remove them from environments. Besides, several antibiotics that are used for various purposes and released in the wastewaters, induce more negative impacts on the environments [5], [24], [51], [52], [86], [106], [150]. Antibiotics have been used extensively not only for treatment of human and animal diseases but also for industry-scale production of aquatic organisms and in the fields of medicine, biology, biochemistry, life science, and agriculture [1], [3], [28], [41], [47], [95], [99], [105], [114], [135], [140]. The uncontrolled use and release of antibiotics-containing waste are continuously causing many environmental and health problems, such as the pollution of aquatic resources damaging effects on the growth of living organisms [35], [54].

On the other hand, the growth and export of shrimp and other seafood bring in high economic values and benefits contributing to the development of the country. In Vietnam, shrimp farming has been and still is, an essential economic sector [13]. There has been increasing attention on both the quantity and quality of shrimp production. Many solutions, models, and advanced technologies were proposed to achieve the highest results. However, water pollution caused by farming and processing of shrimp are not still treated thoroughly. In wastewater, many harmful substances that strongly pollute the environment, are present such as antibiotic residues, stimulants, nitrogen and phosphorus compounds, and wastes from the metabolism of food's nutrients [27]. Notably, antibiotics such as tetracycline, penicillins, and quinolones family were, and still are, widely used in shrimp farming, especially in Vietnam, but they were, and still are, not strictly controlled [14], [62].

For the well-being of society, it is imperative to safely remove pollutants, especially antibiotics, in wastewater discharged from shrimp farming.

2. TiO₂ nanomaterial and its applications

Nanotechnologies based on nanomaterials have been recently considered effective in solving wastewater problems [14]. Furthermore, nanomaterials contribute to development of more efficient treatment processes among advanced water systems [98]. Some materials such as amorphous silica, calcium silicate, silica-based nanotubes, activated carbon, and graphene oxide were used to remove antibiotics fairly effectively [5], [117], [132], [133], [140]. However, most of these materials are of high cost or facing disadvantages in their regeneration after adsorption processes.

Remarkably, TiO₂ emerges as one of the most important semiconductor materials in photoreaction processes, and it is widely used in the fields of energy, health, and food technology. Specifically, TiO₂ is commonly used in photocatalysis, adsorption, and degradation of toxic compounds to simple molecules based on its unique surface properties [33], [43], [60], [61], [144]. Some applications of TiO₂-based implants in biology, and the adsorption of organic molecules onto the TiO₂ surface have been reported in recent investigations [110], [121], [124]. The adsorption processes usually occur on the nanostructured surface of TiO₂ films, depending on the nature of the substance, concentration, type of the heterogeneous facet, and other environmental conditions. Understanding the structure and properties of TiO₂ surfaces important for designing highly active photocatalysts and solar cells. It is known that three stable phases of TiO₂, including rutile, anatase and brookite, were synthesized and applied for various fields of photocatalysis, sensors, and medicine transmission [32], [122]. The characteristics of the TiO₂ phases were well examined, and results showed that rutile is the most stable one. Of the rutile surfaces, the most stable plane (110) is considered thoroughly in both experimental and theoretical studies [118], [122]. Besides, anatase has recently become the subject of intensive interest with high photocatalytic activity in comparison to rutile. For its part,

the (101) plane of anatase which was investigated extensively in previous work, is the most predominant one [136].

In addition, TiO₂ drives most of photocatalytic and photoelectrocatalytic processes [43], [96], [129]. TiO₂ was also widely studied and used in many applications related to environment because of its strong oxidation abilities, chemical stability, nontoxicity, and low cost [43], [96]. When applied for the removal of pollutants, both adsorption and photodegradation contribute considerably to the purification. Many factors are known to significantly affect on the adsorption step and photocatalytic performance of TiO₂. Notably, the size, specific surface area, crystalline phase, and the exposed plane surfaces, as well as the rate of mass transfer for organic pollutant adsorption, are reported [129]. In fact, adsorption is an important stage in photocatalytic reactions which are based on chemical reactions on the surface of the photocatalyst and also in the operation of sensors [32], [43], [96], [102], [129].

Noticeably, the adsorption of simple molecules has been examined in recent years [80], [81], [138] on different surfaces of TiO₂ including rutile and anatase [102], [118], [121], [129], [136]. Interactions between organic molecules such as carboxylic acids, alcohol, ether, benzene, metals, and metal ions on TiO₂ surfaces were also evaluated in several reports [82], [84], [101], [103], [119], [124], [138]. Also, the investigations of geometrical structures and adsorption ability of amino acids, amines, antibiotic molecules on TiO₂ surfaces were performed using computational chemistry and modelling tools [59], [109], [115], [123], [137], [147]. In recent studies, Mahmood, Parameswari and co-workers have reported the details of geometrical structures and adsorption of some organic molecules on TiO₂ surfaces [82], [103]. Accordingly, functionalized organic compounds containing >C=O, -COOH, -OH, -NH₂, -CHO, -CONH- are favorably adsorbed on TiO₂ surfaces. However, in most of the previous investigations, the authors have neither explained in detail the existence and the role of intramolecular interactions nor evaluated the stability of complexes, adsorption ability of molecules on TiO₂ surfaces. Besides, the nature of processes and the role of surface interactions for the adsorption of antibiotic

molecules on TiO₂ surfaces are not analyzed in detail or received enough attention yet.

3. Clay minerals and their applications in the treatment of pollutants

Recent investigations have been carried out to discover the suitable materials to effectively remove organic pollutants and antibiotics residue from wastewater sources [2], [3], [48], [113], [116], [143], [150]. Notably, clay minerals, which are essential components of most soil types, were often applied as adsorbents for wastewater treatment owing to their exceptional properties such as the high cation exchange capacity, good swelling, and high specific surface areas [20], [30], [31], [55], [111]. Besides, clay minerals have layered structures that may consist of various combinations of tetrahedral and octahedral sheets, which are known as kaolinite (a tetrahedral sheet intercalated by an octahedral sheet, i.e., 1:1) and vermiculite (two tetrahedral sheets sandwiching a central octahedral sheet, or 2:1).

Kaolinite mineral is one of the potential materials used in the water purification industry to reduce soil pollution and catalysis for chemical reactions [6], [7], [63], [111], [145]. Kaolinite includes two unique surfaces in its structure: the hydrogen-rich facet (H-slab) and the oxygen-rich facet (O-slab). Harris and co-workers conducted studies on the adsorption capacity of organic compounds including some dyes on kaolinite and amorphous aluminum oxide [58]. Reported results indicated that the H-slab can efficiently adsorb organic compounds and is better than its counterpart O-slab and aluminum oxide surface. Moreover, the H-slab with a high positive charge density is favorable for the adsorption of organic compounds containing electrophilic functional groups such as -OH, -COOH [23], [58]. Johnson's study on the adsorption of benzene, n-hexane, pyridine and 2-propanol on the two kaolinite surfaces indicated that H-slab has a higher adsorption ability than O-slab [67]. Chen and co-workers investigated the adsorption of different amino/ammonium salts of DDA (Dodecyl amine), MDA (N-methyl dodecyl amine), DMDA (N,N-dimethyl dodecyl amine), and DTAC (Dodecyl trimethyl ammonium chloride) on the kaolinite surface both theoretically and experimentally [23]. Their

results imply that the DDA^+ , MDA^+ , DMDA^+ , and DTAC^+ cations can be firmly adsorbed on H-slab and O-slab by forming hydrogen bonds. A recent report by Awad and co-workers, who examined the adsorption of 5-aminosalicylic acid on kaolinite surface [8], suggested that different amino/ammonium cations, amino derivatives adsorb more firmly onto the H-slab than onto the O-slab. The investigation on the adsorption of benzene derivatives containing $-\text{CHO}$, $-\text{COOH}$, $-\text{OH}$, $-\text{NH}_2$, $-\text{SO}_3\text{H}$ groups on H-slab is thus of importance for further evaluation of the geometrical structure, stability of complexes, effects of functional groups, and the role of intermolecular interactions formed on material surfaces.

In recent studies, clay minerals, especially vermiculite, have been suggested as high-potential adsorbents for removing dyes, organic pollutants, and metal cations due to their hydrophilicity and high charge density surface, and layered crystalline structure [107], [131]. They have recently been used further as excipients in pharmaceutical preparations and therapeutic agents in biomedical applications [112]. Vermiculite-based derivatives are regarded as potential nanomaterials for use in various areas of environmental protection [83], [107], [108], [130]. Some reports indicate that the adsorption capacity of molecules on material surfaces mainly depends on the cation exchange and surface complexation (e.g. hydrogen bonds) between functional groups of organic compounds and the charged sites of adsorbents [65], [66]. Besides, the stable configurations result from interactions between adsorbed molecules and surfaces such as hydrogen bonds, acid-base, and van der Waals forces. Most of the weak interactions, especially hydrogen bonds, play a significant role in determining the arrangement of large systems and the eventual synthesis of useful compounds. The hydrogen bonds formed between organic compounds were extensively investigated in various studies [49], [127], as they remarkably contribute to the complexes' stability. Hence, a better knowledge of the nature of intermolecular interactions is necessary for other important purposes, such as the customized design of adsorbents for controlling the sorption and separation of guest molecules. Moreover, although compounds containing the $-\text{OH}$, $-\text{COOH}$

functional groups [8], [20], [23], [148] are found to be conveniently attached to the clay minerals, the origin and role of the inherent interactions and transformations are not identified and analyzed.

4. Investigations on materials surfaces using computational chemistry

It is well known that quantum chemical computations allow us to elucidate the sites of molecules adsorbed on clay minerals and TiO_2 surfaces. This work can be achieved from determination of the relative stabilities of different binding sites and identification of the geometrical details that occur to the adsorbent and the surface following adsorption. Theoretical investigations into the organic molecules and antibiotics adsorbed on the TiO_2 , kaolinite, and vermiculite surfaces were frequently conducted using density functional theory (DFT). The thermodynamic stabilities of different adsorbate-surface systems and the specific role in interactions were examined in previous studies. However, a deep understanding of the existence and effect of surface interactions on the stability of configurations and adsorption process was still not reported in detail [1], [48], [130].

In Vietnam, studies on clay minerals or TiO_2 materials, especially regarding the adsorption ability of organic pollutants on these material surfaces were not thoroughly conducted. There is still a lack of attention to theoretical studies on these materials. Up to now, some combined experimental and theoretical investigations were focused on other surfaces of graphene, activated carbon, and zeolite [56]. In summary, theoretical and experimental investigations on clay minerals and TiO_2 are still limited. In this context, insights into surface phenomena constitute an attractive subject for theoretical studies leading to promising applications.

PART 2. THEORETICAL BACKGROUND AND COMPUTATIONAL METHODS

1. Quantum chemical approaches

1.1. Schrödinger equations

In 1926, based on the combination of Planck's quantum theory and Louis De Broglie's particle-wave duality, Erwin Schrödinger formulated the time-dependent equation of one-particle system in one dimension, as follows:

$$-\frac{\hbar}{i} \frac{\partial \psi(x,t)}{\partial t} = -\frac{\hbar^2}{2m} \frac{\partial^2 \psi(x,t)}{\partial x^2} + V(x,t)\psi(x,t) \quad (1.1)$$

where \hbar is Planck's constant and $\hbar = \frac{h}{2\pi}$, $V(x,t)$ is the potential field of the system, m is the mass of the single-particle, $i = \sqrt{-1}$, $\Psi(x,t)$ the wavefunction describing the state of the system depended on both the x -coordinate and t -time variables. The $\Psi(x,t)$ is a single-valued, continuous function. In a one-dimensional problem, the probability that particle will be found in the region between x and $x + dx$ at time t is determined by $|\Psi(x,t)|^2$ [64], [78].

Equation (1.1) is quite complex, especially for many-body systems. Particularly in chemistry, most quantum systems are considered in the stationary state (the state in which the probability of finding the particle does not change with time, only depends on special coordinates ($|\Psi(x,t)|^2 = |\Psi(x)|^2$)). Therefore, the simpler model used for these systems is the time-independent Schrödinger equation:

$$-\frac{\hbar}{2m} \frac{\partial^2 \psi(x)}{\partial x^2} + V(x)\psi(x) = E\psi(x) \quad (1.2a)$$

This is simply rewritten as: $\hat{H}\Psi = E\Psi$ (1.2b)

where: \hat{H} is the Hamiltonian operator, E is the energy of the system. The (1.2a) and (1.2b) are Schrödinger equations that independent of time.

The Hamiltonian is the total energy operator of the system. For molecules, it includes the contributions of five components: the kinetic energy of the electrons, the

kinetic energy of the nuclei, the electrostatic attraction of the nucleus to the electron, the repulsive force between the electrons, and the repulsive force between the nuclei, as shown in the expression:

$$\hat{H} = \hat{T}_n + \hat{T}_{el} + U_{en} + U_{ee} + U_{nn} \quad (1.3)$$

where: \hat{T}_n : kinetic energy operator of the nuclei

\hat{T}_{el} : kinetic energy operator of $N\bar{e}$

U_{en} : the potential energy of interactions between electrons and nuclei

U_{ee} : the potential energy of interaction between electrons

U_{nn} : the potential energy of interaction between nuclei

It is fully represented by the following equation:

$$\hat{H} = \sum_{A=1}^M \frac{-1}{2M_A} \nabla_A^2 - \sum_{p=1}^N \frac{1}{2} \nabla_p^2 - \sum_{p=1}^N \sum_{A=1}^M \frac{Z_A}{r_{pA}} + \sum_{p=1}^N \sum_{q>p}^N \frac{1}{r_{pq}} + \sum_{A=1}^M \sum_{B>A}^M \frac{Z_A Z_B}{R_{AB}} \quad (1.4)$$

where: A, B: denote for the nuclei A and B

M_A : mass ratio of nucleus A to one electron

p, q: symbol for electrons in the system

Z_A, Z_B : number of units of nuclear charge A, B

r_{pq} : distance between the electrons p and q

r_{pA} : distance between the electron p and the nucleus A

R_{AB} : distance between two nuclei A and B

$$\nabla^2 = \frac{\partial^2}{\partial x^2} + \frac{\partial^2}{\partial y^2} + \frac{\partial^2}{\partial z^2} : \text{Laplacian operator}$$

In equation (1.4), the fourth term cannot be explicitly determined because of the indistinguishable property of electrons. Thus, the Schrödinger equation can only be solved, except for systems containing a single nucleus and single electron like a hydrogen atom. As for systems with two or more electrons, we can only achieve an approximate solution. Solving the Schrödinger equations would yield wave function Ψ and the total energy E of the investigated system.

1.2. The Born - Oppenheimer approximation and Pauli's exclusion principle

1.2.1. Born – Oppenheimer approximation

The Born – Oppenheimer approximation is the best-known mathematical approximation in molecular dynamics that allows the separation of the motion of the nucleus and the electron in a molecule. When the nucleus is stationary relative to the electron, the movement of the electron slightly depends on the movement of the nucleus [64], [73], [78]. Hence, in equation (1.4), the second term equals zero ($\hat{T}_n = 0$) and the last term is constant ($\hat{U}_{nn} = C$). The Hamiltonian for the whole system becomes the Hamiltonian operator for electrons corresponding to the total electron energy of E_{el} :

$$\hat{H}_{el} = -\sum_{i=1}^N \frac{1}{2} \nabla_i^2 - \sum_{i=1}^N \sum_{A=1}^M \frac{Z_A}{r_{iA}} + \sum_{i=1}^N \sum_{j>i}^N \frac{1}{r_{ij}} + C \quad (1.5)$$

For the movement of nuclei in the average field of the electrons, the nuclei operator has the form:

$$\hat{H}_{nucl} = -\sum_{A=1}^M \frac{1}{2M_A} \nabla_A^2 + E_{elec}(\{\mathbf{R}_A\}) + \sum_{A=1}^M \sum_{B>A}^M \frac{Z_A Z_B}{R_{AB}} \quad (1.6)$$

According to the Born – Oppenheimer approach, the complete wavefunction for the system containing N electrons, M nuclei can be rewritten:

$$\Psi(\{\mathbf{r}_i\}, \{\mathbf{R}_A\}) = \Psi_{el}(\{\mathbf{r}_i\}, \{\mathbf{R}_A\}) \Psi_{nucl}(\{\mathbf{R}_A\}) \quad (1.7)$$

The Schrödinger equation can not be solved accurately for a multi-electron system because the interactions between electrons i and j can not be determined clearly. It is impossible to learn their position in space explicitly. Instead only the electron density can be determined. That is the probability of the existence of a particle at a given position.

1.2.2. Pauli's exclusion principle

The \hat{H}_{el} operator in equation (1.4) only depends on the spatial coordinates of the electrons, meaning that it only acts on the space part of the wave function. However, to fully describe electron properties, it is necessary to specify the spin term

and add the electron spin into the space part of the wave function. Let $\alpha(\omega)$ and $\beta(\omega)$ be two spin functions corresponding to spin-up and spin-down. These two spin functions can be chosen to be orthogonal and normalized (orthonormal) as follows:

$$\int \alpha^*(\omega)\alpha(\omega)d\omega = \int \beta^*(\omega)\beta(\omega)d\omega = 1 \text{ or } \langle \alpha | \alpha \rangle = \langle \beta | \beta \rangle = 1 \quad (1.8)$$

$$\int \alpha^*(\omega)\beta(\omega)d\omega = \int \beta^*(\omega)\alpha(\omega)d\omega = 0 \text{ or } \langle \alpha | \beta \rangle = \langle \beta | \alpha \rangle = 0 \quad (1.9)$$

Hence, an electron is not only described by spatial coordinates r but also spin coordinates ω , denoted by $x = \{r, \omega\}$. The wave function of N -electrons system is then written: $\psi(x_1, x_2, \dots, x_N)$ and must be antisymmetrical with the exchange (swapping) of coordinates x (including space and spin) of any two electrons p, q ($p \neq q$):

$$\psi(x_1, \dots, x_p, \dots, x_q, \dots, x_N) = -\psi(x_1, \dots, x_q, \dots, x_p, \dots, x_N) \quad (1.10)$$

The exclusion principle is the consequence that, if $x_p = x_q$ for $p \neq q$, then $\psi(x_1, \dots, x_p, \dots, x_q, \dots, x_N) = 0$ (1.11). This means that none of the n particles may be in the same state (Pauli's exclusion principle) [64], [73], [78].

1.3. The variational principle

The accurate solution of the Schrödinger equations for systems with many nuclei and electrons is not possible. There are helpful approximated methods that can, in many cases, reduce the complete problem to a much simpler one, which is based on the variational principle [26], [64], [73], [78]. In particular, we consider a Hamiltonian H and a function Ψ with the sole condition that it stays normalized. We can calculate the expectation value of the energy for such function:

$$\langle H \rangle = \int \Psi^* H \Psi dr \quad (1.12)$$

where r represents all the integration coordinates.

The functions Ψ for which $\langle H \rangle$ is stationary – i.e. does not vary to first order in slight variations of Ψ – are the eigenfunctions of the energy. In other words, the Schrödinger equation is equivalent to a stationarity condition. For the eigenfunctions Ψ_n of a Hamiltonian H , with associated eigenvalues E_n :

$$H \Psi_n = E_n \Psi_n \quad (1.13)$$

We label the ground state with $n = 0$ and the ground-state energy as E_0 . The variational principle states, quite simply, for any different function Ψ ,

$$\langle H \rangle = \frac{\int \Psi^* H \Psi dr}{\int \Psi^* \Psi dr} \geq E_0 \quad (1.14)$$

This simple result is significant. It indicates that any function Ψ yields the expected energy an upper estimation of the energy of the ground state. For the unknown ground state, an approximation to the ground state can be found by varying Ψ inside a given set of functions and determining a function that minimizes $\langle H \rangle$.

1.4. Basis sets

The basis set is the set of mathematical functions from which the wave function is constructed. To obtain the best approximate solution for Schrödinger equations we need to improve computational methods and choose the suitable basis sets for investigated systems. The more extensive basis set would yield a closer description of electrons in the system to reality and a better approximation, and vice versa. For each system, a consideration of the basis sets to achieve a good result is necessary and must be done carefully [26], [64], [73], [78].

1.4.1. Slater and Gaussian orbitals

There are two basic function types used in electronic structure calculations: Slater-type orbital (STO) and Gaussian-type orbital (GTO) with corresponding expressions in spherical coordinates:

$$\Psi^{\text{STO}} = \psi_{\xi, n, l, m}(r, \theta, \varphi) = N \cdot Y_{l, m}(\theta, \varphi) \cdot r^{n-1} \cdot e^{-\xi \cdot r} \quad (1.15)$$

$$\Psi^{\text{GTO}} = \psi_{\alpha, n, l, m}(r, \theta, \varphi) = N \cdot Y_{l, m}(\theta, \varphi) \cdot r^{2n-2-1} \cdot e^{-\xi \cdot r^2} \quad (1.16)$$

where N is the normalized factor; $r = |r_{\text{orbital}} - R_A|$, where r_{orbital} is the orbital coordinate vector; R_A is the nuclear coordinate A ; $Y_{l, m}$ is a spherical function; ξ is an exponent of the corresponding STO and GTO functions.

In general, to achieve a comparable accuracy, the number of GTO functions must be three times the number of STO. However, GTO is more advantageous for computational costs than STO because it is convenient to three- and four-centered

integrals. Thus, GTO is often used in electronic structure calculations. Many basis functions have focused only on describing the importance of energy (inner shell electron region) and have not paid attention to the chemically significant composition (valence-shell electron region). In order to describe well the outer valence shell, it is crucial to have a large enough basis set; although it can take a long time for computations. Hence, combining the complete set of primitive gauss type orbital (PGTO) with a smaller basis set is necessary. Such a linear combination is called a contracted basis set and therefore obtains a simplified function (CGTO) as follow:

$$\Psi^{\text{CGTO}} = \sum_i^k a_i \cdot \Psi_i^{\text{PGTO}} \quad (1.17).$$

In equation (1.17), a_i is the reduction coefficients and k is the reduction order. The Ψ^{CGTO} is more similar to Ψ^{STO} .

1.4.2. Some popular basis sets

i) Pople basis sets

STO-nG: a combination of n PGTOs to represent an STO, with $n = 2 \div 6$. The optimum combination of speed and accuracy was achieved for $n = 3$ as compared to calculations using STOs. The STO-3G has been applied for most of the atoms and is known as a 'minimal' basis set.

k -nlmG: (split-valence basis set) where k is the number of PGTO functions used for one core orbital. The set of nlm presents the number of valence shell orbital functions divided into calculations and the number of the PGTO function used in the combination. Each basis set can again add diffusion functions, polarization functions, or both of them. The diffusion function is usually the s - and the p - function that precedes the letter G, denoted by the sign "+" or "++" in which the first sign "+" indicates adding diffusion functions s -, p - for heavy atoms, the second "+" implies the addition of diffusion function s - for H atoms. After the letter G, the polarization function is denoted by lowercase letters (or the * and **). Some basis sets are used widely in quantum chemical calculations such as 6-31+G(d,p); 6-31++G(2d,2p), 6-31G*, 6-311G**.

ii) Correlation consistent basis sets

Dunning and coworkers have proposed a somewhat smaller set of primitives that yields comparable results to the atomic natural orbital basis sets. Several different sizes of correlation consistent (cc) basis set are available, including cc-pVDZ, cc-pVTZ, cc-pVQZ, cc-pV5Z and cc-pV6Z (correlation consistent polarized Valence Double/ Triple/ Quadruple/ Quintuple/ Sextuple Zeta). The basis sets are then created by adding polarization functions to improve the electronic space and better describe the distribution of the electrons. Therefore, the ‘cc-’ basis sets are supplemented by diffusion functions and denoted by aug-cc-pVDZ, aug-cc-pVTZ, aug-cc-pVQZ, aug-cc-pV5Z. These basis sets yield highly approximated results and of course, describe efficiently systems that consist of weak or non-covalent interactions. Besides, these basis sets are used to extrapolate to a complete basis set.

iii) Polarization consistent basis sets

Remarkably, the low angular momentum functions are more critical for the Hartree-Fock (HF)/ Density Functional Theory (DFT) methods than for correlation methods in the case of using large basis sets. The polarization consistent (pc-) basis sets are developed similarly to the cc-, however, they are optimized for the DFT methods. Furthermore, these basis sets focus on describing the polarization of the electron density on the atoms rather than describing the correlation energy. Some types of pc- functions include pc-0, pc-1, pc-2, pc-3, pc-4, and generally denote by pc-n. The -n value corresponds to the number of polarization functions with considerable angular momentum.

1.5. Hartree-Fock approximation

The Hartree Fock (HF) method is one of the simplest approximations, based on the physical conception of the average effective potential field for each electron to have a solution of the Schrödinger equation for the N-electron system. The field is combined by the electrostatic attraction of the nucleus and the average repulsive potential of all other electrons [64], [73], [78]. The most straightforward wave function to describe the ground state of the N-electron system is a Slater determinant:

$$\Psi_{el} = \left| \chi_i(x_1) \chi_j(x_2) \dots \chi_k(x_N) \right\rangle \quad (1.18)$$

According to the variational principle, the wave function with the lowest energy:

$$E_0 = \left\langle \Psi_0 \left| \hat{H} \right| \Psi_0 \right\rangle \quad (1.19)$$

Minimizing the energy for the choice of spin orbitals can draw HF equations:

$$\hat{f}(1)\chi_i(1) = \varepsilon_i \chi_i(1), i = 1, 2, \dots, N \quad (1.20)$$

in which $\hat{f}(1)$ is Fock operator:

$$\hat{f}(1) = \hat{h}(1) + \sum_j \left[\hat{J}_j(1) - \hat{K}_j(1) \right] = \hat{h}(1) + \hat{V}(1) \quad (1.21)$$

This expression allows the determination of the optimal spin-orbital. Thus, the HF method is used by replacing the N-electron system with N one-electron systems, in which e-e repulsive interactions are handled by average field. The HF equations are non-linear differential; therefore, they must be solved using an iterative method. The procedure for solving these equations is called the self-consistent field (SCF) method. The SCF method is an iterative method that involves selecting an approximate Hamiltonian, solving the Schrödinger equation to obtain a more accurate set of orbitals, and then solving the Schrödinger equation again with these until the results converge.

1.6. Density functional theory

In solving quantum problems as well as Schrödinger equations, electron densities are practical, and reasonably accurate approximations, especially for many-body systems [26], [64], [73], [78]. Density Functional Theory (DFT) comes from the view that the energy of a system can be expressed as a function of its electron density $\rho(\mathbf{r})$.

1.6.1. The Hohenberg-Kohn theorem

Theorem 1: Electron density $\rho(\mathbf{r})$ determines the external potential $V_{ext}(\rho(\mathbf{r}))$, the wave function $\phi(\rho(\mathbf{r}))$ as well as other properties of the system at the ground state. The external potential (and hence the total energy) is a unique functional of the electron density.

Theorem 2: The functional that delivers the ground-state energy of the system gives the lowest energy if and only if the input density is the actual ground-state density. In other words, the energy of the Hamiltonian reaches its absolute minimum, i.e., the ground state, when the charge density is that of the ground state.

$$\int \bar{\rho}(\mathbf{r})d\mathbf{r} = N \rightarrow E[\rho(\mathbf{r})] \geq E_0 \quad (1.22)$$

1.6.2. Kohn-Sham equations

The foundation for using DFT methods in computational chemistry is the introduction of orbitals, as suggested by Kohn and Sham (KS). The idea in the KS approach is to split the kinetic energy functional into two parts. One can be computed precisely and a small correction term. For the systems of non-interacting electrons, the energy functional is divided into specific components, in particular

$$E[\rho(\mathbf{r})] = T_{\text{ni}}[\rho(\mathbf{r})] + V_{\text{ne}}[\rho(\mathbf{r})] + V_{\text{ee}}[\rho(\mathbf{r})] + \Delta T_{\text{ni}}[\rho(\mathbf{r})] + \Delta V_{\text{ee}}[\rho(\mathbf{r})] \quad (1.23)$$

where the terms correspond to the kinetic energy of the non-interacting electrons, the nuclear-electron interaction, the classical electron-electron repulsion, the correction to the kinetic energy, and all non-classical corrections to the electron-electron repulsion energy.

Within an orbital expression for the density, the equation (1.23) can be rewritten as

$$\begin{aligned} E[\rho(\mathbf{r})] &= T_{\text{S}}[\rho] + J[\rho] + E_{\text{XC}}[\rho] + E_{\text{Ne}}[\rho] \\ &= T_{\text{S}}[\rho] + \frac{1}{2} \iint \frac{\rho(\mathbf{r}_1)\rho(\mathbf{r}_2)}{r_{12}} d\mathbf{r}_1 d\mathbf{r}_2 + E_{\text{XC}}[\rho] + \int V_{\text{Ne}}\rho(\mathbf{r})d\mathbf{r} \\ &= -\frac{1}{2} \sum_i^N \langle \varphi_i | \nabla^2 | \varphi_i \rangle + \frac{1}{2} \sum_i^N \sum_j^N \iint |\varphi_i(\mathbf{r}_i)|^2 \frac{1}{r_{12}} |\varphi_j(\mathbf{r}_j)|^2 d\mathbf{r}_1 d\mathbf{r}_2 + E_{\text{XC}}[\rho(\mathbf{r})] - \sum_i^N \int \sum_A^M \frac{Z_A}{r_{1A}} |\varphi_i(\mathbf{r}_i)|^2 d\mathbf{r}_i \end{aligned} \quad (1.24)$$

The resulting equations are given as follow:

$$\left(-\frac{1}{2} \nabla^2 + \left[\int \frac{\rho(\mathbf{r}_2)}{r_{12}} d\mathbf{r}_2 + V_{\text{XC}}(\mathbf{r}) - \sum_A^M \frac{Z_A}{r_{1A}} \right] \right) \varphi_i = \left(-\frac{1}{2} \nabla^2 + V_{\text{eff}}(\mathbf{r}_1) \right) \varphi_i = \varepsilon_i \varphi_i \quad (1.25)$$

in which ε_i is the Kohn – Sham orbital energy; $V_{\text{eff}}(\mathbf{r})$ is determined by expression:

$$V_{\text{eff}}(\mathbf{r}) = \int \frac{\rho(\mathbf{r}_2)}{r_{12}} d\mathbf{r}_2 + V_{\text{XC}}(\mathbf{r}) - \sum_A^M \frac{Z_A}{r_{1A}} \quad (1.26)$$

and $V_{XC}[\rho]$ is the exchange-correlation potential. The derivative of E_{XC} is defined by the expression:

$$V_{XC} \equiv \frac{dE_{XC}[\rho]}{d\rho} \quad (1.27)$$

Solving the Kohn-Sham equations would yield the orbital orbits of one electron Ψ_{i,r_i} , if $E_{XC}[\rho]$ is known and $V_{XC}[\rho]$ is calculated. Thus, Kohn-Sham orbitals allow the calculation of $\rho(\mathbf{r})$ by the formula:

$$\rho(\vec{\mathbf{r}}) = \sum_{i=1}^N |\phi_i(\vec{\mathbf{r}})|^2 \quad (1.28)$$

The solution to Kohn – Sham equations is carried out using the self-consistent field (SCF) method. It is customary to separate EXC into two parts in later works, a pure exchange E_X and a correlation part E_C . Each exchange and correlation energy is often written in terms of the energy per particle (energy density), ϵ_x and ϵ_c .

$$E_{XC}[\rho] = E_X[\rho] + E_C[\rho] = \int \rho(\mathbf{r})\epsilon_x[\rho(\mathbf{r})]d\mathbf{r} + \int \rho(\mathbf{r})\epsilon_c[\rho(\mathbf{r})]d\mathbf{r} \quad (1.29)$$

1.6.3. Local density approximation

In the Local Density Approximation (LDA), the local density can be treated as a uniform electron gas. The exchange energy for uniform electron gas according to the Dirac formula is calculated as follows:

$$E_X^{LDA}[\rho] = -C_x \int \rho^{4/3}(\mathbf{r})d\mathbf{r} \quad (1.30)$$

In the general case, α -electron and β -electron densities are not equal, LDA has been replaced by the Local Spin Density Approximation (LSDA) as shown in Eq. (1.30).

$$E_X^{LSDA}[\rho] = -2^{1/3}C_x \int [\rho_\alpha^{4/3} + \rho_\beta^{4/3}] d\mathbf{r} \quad (1.31)$$

LSDA can be written by total density and spin polarization function.

$$E_X^{LSDA}[\rho] = -\frac{1}{2}C_x\rho^{1/3}[(1 + \zeta)^{4/3} + (1 - \zeta)^{4/3}] \quad (1.32)$$

In addition, the correlation energy of uniform electron gas is determined by Quantum Monte Carlo methods for many different density values. The LSDA method is an exact DFT method for a particular case of uniform electron gas. For molecular systems, the LSDA approximation underestimates the exchange energy by ~10%,

creating errors that are larger than the whole correlation energy. Besides, the bond strengths are overestimated by $\sim 100 \text{ kJ.mol}^{-1}$. In general, the LSDA method provides results with an accuracy similar to HF methods.

1.6.4. General gradient approximation

To improve LSDA, considering the non-uniform electron gas is necessary. It means that the exchange-correlated energy depends not only on the electron density but also on its derivative. In Generalized Gradient Approximation (GGA) methods, the first derivative of the density is included as a variable. GGA methods are sometimes referred to as non-local methods. In the GGA, the exchange-correlation energy E_{XC} is given as follows:

$$E_{XC}^{GGA} [\rho_\alpha, \rho_\beta] = \int f(\rho_\alpha, \rho_\beta, \nabla\rho_\alpha, \nabla\rho_\beta) d\mathbf{r} \quad (1.33)$$

In practice, E_{XC}^{GGA} is often split into its exchange and correlation terms

$$E_{XC}^{GGA} = E_X^{GGA} + E_C^{GGA}. \quad (1.34)$$

The exchange part of E_{XC}^{GGA} can be written as

$$E_X^{GGA} = E_X^{LDA} - \sum_\sigma \int F(s_\sigma) \rho_\sigma^{4/3}(\mathbf{r}) d\mathbf{r} \quad (1.35)$$

$$s_\sigma(\mathbf{r}) = \frac{|\nabla\rho_\sigma(\mathbf{r})|}{\rho_\sigma^{4/3}(\mathbf{r})}$$

where s_σ is to be understood as a local inhomogeneity parameter.

The correlation part is similarly written as an enhancement factor added to the LSDA functional. The t variable is related to the x variable utilizing yet another spin-polarization function.

$$\epsilon_c^{GGA} = E_C^{LDA} + H(t)$$

$$H(t) = af_3^3 \ln \left[1 + \left(\frac{1 + At^2}{1 + At^2 + A^2 t^4} \right) dt^2 \right]; A = b \left[\exp \left(-\frac{E_C^{LDA}}{cf_3^3} \right) - 1 \right]^{-1} \quad (1.36)$$

$$f_3(\zeta) = \frac{1}{2} \left[(1 + \zeta)^{2/3} + (1 - \zeta)^{2/3} \right]; t = \left[2(3\pi^3)^{1/3} f_3 \right]^{-1} x$$

The a and b parameters are non-empirical.

1.6.5. Hybrid functionals

The basic idea of this approach is to use the exact exchange energy and rely on approximate functionals only for the part missing in the HF method, i.e., the electron correlation,

$$E_{\text{XC}} = E_{\text{X}}^{\text{exact}} + E_{\text{C}}^{\text{KS}} \text{ where } E_{\text{X}}^{\text{exact}} = \frac{1}{2} \iint \frac{\rho_0(\mathbf{r}_1) h_{\text{X}}^{\text{KS}}(\mathbf{r}_1, \mathbf{r}_2)}{r_{12}} d\mathbf{r}_1 d\mathbf{r}_2 \quad (1.37)$$

with the exact density ρ_0 .

For atoms, this concept indeed delivers good results. However, it does not live up to the expectation at all for molecules and chemical bonding.

In a different avenue to exploit the exact exchange outlined by Becke, the exchange-correlation energy (E_{XC}), is defined by integration over the λ -dependent exchange-correlation potential energy. The non-classical e-e interaction (E_{ncl}) corresponds to the pure potential energy contribution and depends on λ .

$$E_{\text{XC}} = \int_0^1 E_{\text{ncl}}^{\lambda} d\lambda \quad (1.38)$$

The simplest approximation for this approach is to assume E_{ncl}^{λ} is a linear function in λ , as follows:

$$E_{\text{XC}}^{\text{HH}} = \frac{1}{2} E_{\text{XC}}^{\lambda=0} + \frac{1}{2} E_{\text{XC}}^{\lambda=1} \quad (1.39)$$

This equation represents the so-called half-and-half (HH) combination of exact exchange and density functional exchange-correlation.

It is noted that the most popular hybrid functional is known as B3LYP in which the exchange functional is utilized by Beck, and correlation functional is proposed by Lee, Yang, and Parr (LYP). The B3LYP exchange-correlation energy expression is

$$E_{\text{XC}}^{\text{B3LYP}} = (1-a)E_{\text{X}}^{\text{LSD}} + aE_{\text{X}}^{\lambda=0} + bE_{\text{X}}^{\text{B88}} + cE_{\text{C}}^{\text{LYP}} + (1-c)E_{\text{C}}^{\text{LSD}} \quad (1.40)$$

in which a, b, c are the coefficients determined by Becke as follows: a \sim 0.20; b \sim 0.72; c \sim 0.81.

1.6.6. Van der Waals functionals

Recently, DFT has been widely applied with approximate local and semilocal density functionals for the interactions for molecules and materials. For biomolecules, soft matter, and van der Waals (vdW) complexes, the functionals, including vdW forces, need to be added and considered to describe cohesion, bonds, structures, and other properties [34], [64], [78]. The exchange-correlation energy now can be written as:

$$E_{XC} = E_X^{GGA} + E_C^{LDA} + E_C^{nl} \quad (1.41)$$

where E_C^{nl} is the nonlocal correlation-energy part. The simple form of E_C^{nl} is

$$E_C^{nl} = \frac{1}{2} \int d^3r d^3r' n(\vec{r}) \phi(\vec{r}, \vec{r}') n(\vec{r}') \quad (1.42)$$

where $\phi(\vec{r}, \vec{r}')$ is a function depending on $\vec{r} - \vec{r}'$ and the density n in the vicinity of \vec{r} and \vec{r}' . For full potential approximation, exacted at the long distances between separated components, the E_C^{nl} can be expressed as:

$$E_C^{nl} = \int_0^\infty \frac{du}{2\pi} \text{tr} \left[\ln(1 - V_\chi) - \ln \varepsilon \right] \quad (1.43)$$

in which χ is the density response to a fully self-consistent potential with long-range, V is the interelectronic Coulomb interaction, ε an approximated dielectric function, and u the imaginary frequency.

For the layered structures, the scheme obtained by expanding E_C^{nl} equation above to second order in $S \equiv 1 - \varepsilon^{-1}$ is given

$$E_C^{nl} \approx \int_0^\infty \frac{du}{4\pi} \text{tr} \left[S^2 - \left(\frac{\nabla S \cdot \nabla V}{4\pi e^2} \right)^2 \right]. \quad (1.44)$$

In a plane-wave presentation, $S_{q,q'}$ is followed to conditions and approximated by the plasmon-pole model: $S_{q,q'} = \frac{1}{2} (\tilde{S}_{q,q'} + \tilde{S}_{-q',-q})$. (1.45)

For considering nonlocal exchange-correlation energy, in general, the E_{XC}^{nl} is given in the form:

$$E_{\text{XC}}^{\text{nl}} = \int_0^\infty \frac{du}{4\pi} \sum_{\vec{q}, \vec{q}'} \left[1 - (\hat{q}, \hat{q}')^2 \right] S_{\vec{q}, \vec{q}} S_{\vec{q}', \vec{q}'}. \quad (1.46)$$

1.7. Pseudopotential and plane-wave methods

In the solid states, pseudopotentials and plane-wave basis sets are essential features, providing consistent and highly accurate results for investigated systems [37]. For natural materials, one needs to solve the Schrödinger equation using the proper potential $v(r)$, as shown in eq. (1.47),

$$\left[-\frac{1}{2} \nabla^2 + v(r) \right] \psi(\mathbf{k}, \mathbf{r}) = E(\mathbf{k}) \psi(\mathbf{k}, \mathbf{r}) \quad (1.47)$$

and it will soon become clear how the potential determines both the band-structure method and its associated essential functions. This kind of basis functions strongly differs between molecules and extended solids due to the underlying translational symmetry. Bloch suggested a theorem that contains the basis functions for translational invariant solid, namely a plane wave ($e^{i\mathbf{k}\mathbf{r}}$) which is the symmetry-adapted wave function to a crystal's boundary conditions. It means that any type of crystal wave function $\psi_n(\mathbf{k}, \mathbf{r})$ can be expressed as a plane-wave expansion and written as

$$\psi_n(\mathbf{k}, \mathbf{r}) = \sum_{\mathbf{K}} c_n(\mathbf{k}, \mathbf{K}) e^{i(\mathbf{k}+\mathbf{K})\mathbf{r}} = e^{i\mathbf{k}\mathbf{r}} \sum_{\mathbf{K}} c_n(\mathbf{k}, \mathbf{K}) e^{i\mathbf{K}\mathbf{r}} \quad (1.48).$$

Here, \mathbf{K} is a reciprocal lattice vector, and the contribution coefficients c_n must be sought, either analytically or numerically.

Due to the simplicity of plane waves, they are convenient to perform computations, especially if they are applied to simple (non-chemical) potential. For the realistic potential, plane waves can become complicated. For instance, as illustrated in Figure 1, the 3s radial function of Na atom from a self-consistent calculation has two radial nodes close to the characteristic of the electron kinetic energy, reflecting the significant nuclear potential.

Outside the atom, there is a smooth exponential decay of the valence function. For crystalline Na, the new situation will also reflect different regions with step

potential valleys or a relatively smooth potential in the bonding region, as shown in Figure 2.

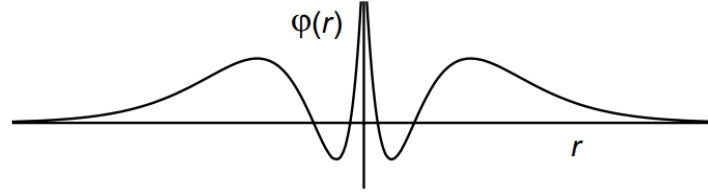


Figure 1. Radial part of the 3s atomic orbital of the Na atom [ref. 37].

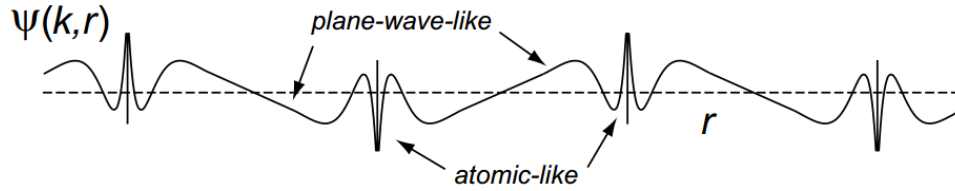


Figure 2. Schematic drawing of a 3s-derived Bloch function of one-dimensional crystals of Na atoms [ref. 37].

The process of the symmetric adaptive wave function (Bloch function) of one-dimensional Na crystals may not reflect both potential types. The local 3s atomic function has been transformed previously into a fully delocalized function. Therefore, there must be enough variational freedom to simultaneously exhibit core-like behavior close to the atom and enough typical plane-wave properties between atoms. The size of the plane-wave basis set, which is proportional to Z^3 , will be tourable for a band-structure calculation on the diamond. For larger systems, it will computationally explode and make realistic calculations almost impossible. Three different approaches have been proposed to address this issue by i) ignoring the core functions, ii) modifying the potential, also ignoring the core functionals, and iii) modifying the basis sets and splitting the functional into core and beyond-core functions.

In addition, for where the low-lying core orbitals ϕ_{core} of an atom are known, it is impossible to construct plane waves representing the valence levels by forcing these plane waves to be orthogonal to the core levels for a specified k , as follow:

$$\phi^{\text{OPW}}(\mathbf{k}, r) = e^{i\mathbf{k}r} + \sum_{\text{core}} c_{\text{core}}(\mathbf{k}) \phi_{\text{core}}(\mathbf{k}, r) \quad (1.49).$$

This is the original approach of the orthogonal plane wave (OPW) method by using a k -weighted combination of OPWs to extend the Bloch function. Consequently, an OPW oscillates at the core and acts as a plane wave in the outer regions of the atom.

A more systematic way to address the oscillations of the core functions is given by the pseudopotential method. This approach aims to remove these oscillations by replacing a strong ion-electron potential with a weaker pseudopotential (as shown in Fig. 3). The atom can thus be considered as a small perturbation of the electron gas. Pseudopotential theory - called the combined approximation method - was given firstly by Hellmann. Pseudopotentials nowadays can be known as effective core potentials.

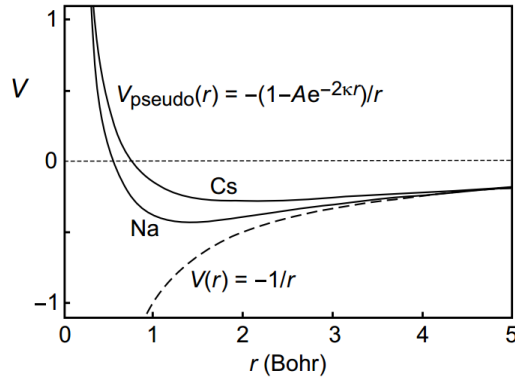


Figure 3. The graph shows the first random substitution for two alkali metals Na, Cs according to Hellmann [ref. 37].

Furthermore, substitution methods have been considered for solid-state by replacing the OPW orthogonality recipe with an efficient potential. Indeed, the pseudopotential theory is applied not only to solid-state but also to molecular quantum chemistry. In contrast to Hellmann's simple, the local pseudopotential (Figure 3) for the alkali metals,

$v_{\text{pseudo}}(\mathbf{r}) = -\frac{1}{r}(1 - Ae^{-2\kappa r})$ (1.50), modern pseudopotentials are either semilocal or

nonlocal. Mathematically, a projection operator P_l for each l channel ensures, in the semilocal case, that each orbital feels its correct pseudopotential,

$$v_{\text{pseudo}}(\mathbf{r}) = \sum_{l=0}^{\infty} v_l(\mathbf{r})P_l. \quad (1.51)$$

Over the past decades, new methods have been proposed, promising both accuracy and faster performance. They enable one to describe complex systems of chemistry and physics. In the first approach, the inner, atom-like wave functions are discarded altogether and replaced by a much weaker potential. In the second approach, the outer wave functional augments exactly these atom-like partial waves. One solution is then given by combining two ideas into a unified electronic structure method. The projector augmented wave (PAW) can be considered a pseudopotential method in which the pseudopotential is immediately adapted to the electronic environment. This is a possible way for ab-initio molecular dynamics to be performed using an all-electron method and to treat massive chemical systems composed of several thousands of atoms.

1.8. Atoms In Molecules and Natural Bond Orbitals approaches

1.8.1. Atoms In Molecules analysis

In Atoms In Molecules (AIM) theory, the topology of the charge distribution is dominated by the electron-nuclear force, causing the electron density ($\rho(\mathbf{r})$) to exhibit maxima at the nuclear positions, thereby imposing the atomic form on the structure of matter [87]. The electron density ($\rho(\mathbf{r})$) is the square of the wave function and is integrated over ($N_{\text{elec}}-1$) coordinates.

$$\rho(\mathbf{r}_1) = \int \left| \Psi(\mathbf{r}_1, \mathbf{r}_2, \mathbf{r}_3, \dots, \mathbf{r}_{N_{\text{elec}}}) \right|^2 d\mathbf{r}_2 d\mathbf{r}_3 \dots d\mathbf{r}_{N_{\text{elec}}} \quad (1.52)$$

If a molecule can be broken down into several volumetric parts, each with a specific nucleus (A in this case), then the electron density can be integrated to obtain the number of electrons present in each atomic basin and atomic charge,

$$Q_A = Z_A - \int_{\Omega_A} \rho(\mathbf{r}) d\mathbf{r} \quad (1.53)$$

Q_A is the atomic charge, Z_A is the nuclear charge, Ω_A is the atomic pot.

The division of atomic confinement space in a molecule requires a "choice" for a volume factor in space to possess a nucleus. The most logical way is the AIM method of Richard Bader. This method uses electron density as the starting point because the electron density is a genuine problem, measured experimentally or

theoretically, deciding shape and material formation. Thus, some properties of interactions in investigated systems are clarified based on electron density ($\rho(r)$) which is determined by the gradient vector ($\nabla\rho(r)$).

$$\nabla\rho = u_x \frac{\partial\rho}{\partial x} + u_y \frac{\partial\rho}{\partial y} + u_z \frac{\partial\rho}{\partial z} \quad (1.54)$$

Here, u_x , u_y , and u_z are three unit vectors perpendicular to the surface of electron density and point to the lowest slope. A sequence of infinitesimal gradient vectors corresponds to a gradient path. Because gradient vectors have one direction, this line also has a direction: going up or down. All of them are attracted to one point in space, and this point is called the "attractor". All nuclei are "points of attraction", and the set of gradients that each nucleus is called "atomic pot". This is the most important thing about AIM theory because the "atomic pot" constitutes the space that locates an atom. The second important point of AIM theory is the definition of association. The critical point (CP) is when the electron density is very large or the gradient vector $\nabla\rho(r) = 0$. The CPs are classified based on the individual values λ_1 , λ_2 , and λ_3 of the electron density Hessian matrix:

$$\left\{ \begin{array}{ccc} \frac{\partial^2\rho}{\partial x^2} & \frac{\partial^2\rho}{\partial x\partial y} & \frac{\partial^2\rho}{\partial x\partial z} \\ \frac{\partial^2\rho}{\partial y\partial x} & \frac{\partial^2\rho}{\partial y^2} & \frac{\partial^2\rho}{\partial y\partial z} \\ \frac{\partial^2\rho}{\partial z\partial x} & \frac{\partial^2\rho}{\partial z\partial y} & \frac{\partial^2\rho}{\partial z^2} \end{array} \right\} \quad (1.55)$$

All individual values λ_1 , λ_2 , and λ_3 , are different from zero, and their signs are used to define the CP type. The Laplacian of the electron density ($\nabla^2\rho(r)$) is the sum of the eigenvalues of the Hessian density matrix, with the expression:

$$\nabla^2\rho(r) = \lambda_1 + \lambda_2 + \lambda_3 \quad (1.56)$$

It is noted that the electron density ($\rho(r)$) at the bond-critical point (BCP) is the most important parameter. The magnitude of $\rho(r)$ is used to determine the strength of bonds. In general, the larger value of $\rho(r)$, the stronger bonding, and conversely, the smaller value of $\rho(r)$, the weaker bonding. Besides, the $\nabla^2(\rho(r))$ values describe

the type of bonding. For instance, it is a covalent bond if the $\nabla^2(\rho(r)) < 0$ and it can be an ionic bond, a hydrogen bond, or a van der Waals interaction if the $\nabla^2(\rho(r)) > 0$.

AIM analysis also gives the local kinetic energy density ($G(r)$) and the local potential energy density ($V(r)$) at BCPs, which are related to Laplacian according to the expression:

$$\frac{1}{4}\nabla^2(\rho(r)) = 2G(r) + V(r) \quad (1.57)$$

The total energy density of electrons ($H(r)$) localized in BCP includes $G(r)$ and $V(r)$.

$$H(r) = G(r) + V(r) \quad (1.58)$$

Moreover, at BCPs, Espinosa and et al. [40] examined the correlation of hydrogen bonding energy and its potential energy density, as expressed in the empirical formula:

$$E_{\text{HB}} = 0.5V(r) \quad (1.59).$$

1.8.2. Natural Bond Orbitals analysis

Some characteristics in Natural Bond Orbital (NBO) approach include natural (semi-)localized molecular orbitals (NLMOs), natural atomic orbitals (NAOs), natural bond orbitals (NBOs), natural population analysis (NPA), and also donor-acceptor scheme upon interactions and complex formations [77], [134]. The NBO method uses only the first-order reduced density matrix of the wave function and hence applies to wavefunctions of general mathematical form. In the open-shell case, the analysis is performed in terms of different NBOs for different spins, based on different density matrices for α and β spin.

According to the simple bond orbital, each bonding NBO σ_{AB} can be written by two directed valence hybrids (NHOs) h_{A} , h_{B} on atoms A and B, and corresponding polarization coefficients c_{A} , c_{B} ,

$$\sigma_{\text{AB}} = c_{\text{A}} h_{\text{A}} + c_{\text{B}} h_{\text{B}} \quad (1.60).$$

The bonding characteristic is determined as covalent ($c_{\text{A}} = c_{\text{B}}$) or ionic ($c_{\text{A}} \gg c_{\text{B}}$) in nature. Each valence bonding NBO (1.60) has a corresponding valence antibonding NBO σ_{AB}^* given by expression

$$\sigma_{AB}^* = c_B h_A - c_A h_B \quad (1.61).$$

The ‘‘Lewis’’-type (donor) NBOs (1.60) are thereby complemented by the ‘‘non-Lewis’’-type (acceptor) NBOs (1.61) that are formally empty. Weak occupancies of the valence antibonding (1.61) signal irreducible departures from actual delocalization effects. The energetic stabilization due to such $\sigma \rightarrow \sigma^*$ donor-acceptor interactions can be considered by second-order perturbation theory, particularly for the $\sigma_i \rightarrow \sigma_j^*$ interaction,

$$\Delta E_{i \rightarrow j}^{(2)} = -2 \frac{\langle \sigma_i | \hat{F} | \sigma_j^* \rangle^2}{\epsilon_j^* - \epsilon_i} \quad (1.62)$$

where \hat{F} is the effective orbital Hamiltonian and $\epsilon_i = \langle \sigma_i | \hat{F} | \sigma_i \rangle$, $\epsilon_j^* = \langle \sigma_j^* | \hat{F} | \sigma_j^* \rangle$ are the respective orbital energies of donor and acceptor NBOs. As a result, valence antibondings (1.61) lead to a far-reaching extension of elementary Lewis structure concepts to provide delocalization corrections in simple NBO perturbative estimated as in the Eq. (1.62). As a result of each $\sigma_i \rightarrow \sigma_j^*$ perturbation, the starting NBO acquires a weak antibonding ‘‘tail’’ in the final (doubly occupied) NLMO Ω_i . In general, each semi-localized NLMO Ω_i can be expressed as a linear combination of the parent Lewis-type NBO σ_i (with coefficient $c_{ii} \approx 1$) and weak residuals ($c_{ji} \approx 0$) from non-Lewis (NL) NBOs σ_j^*

$$\Omega_i = c_{ii} \sigma_i + \sum_j^{NL} c_{ji} \sigma_j^* \quad (1.63)$$

that reflect the irreducible physical effect of $\sigma_i \rightarrow \sigma_j^*$ delocalizations. Despite the compact, recognizable forms of NLMOs and their close connection to chemical structure concepts, it is essential to recognize that a Slater determinant of doubly occupied NLMOs is equivalent to the usual MO wavefunction. Hence, the simplicity of NBO-based expansions such as (1.63) is achieved with no loss of accuracy in the description of ψ .

2. Computational methods

2.1. TiO_2 systems

Geometrical structures of organic molecules, antibiotics, and surfaces are taken into account experimental data [18], [97], [126] and then optimized using the VASP program [57], [68]. The unit cells are chosen with four layers (two layers are frozen and two layers are relaxed) or two layers (relaxed) for rutile- TiO_2 (110) surface (r- TiO_2) and two layers (relaxed) for anatase- TiO_2 (101) surface (a- TiO_2) to investigate the adsorption of molecules on surfaces with an acceptable computational cost. The surface structures contain the double-bonded and neighbor bridging oxygen atoms (O_b) and five-fold and six-fold coordinated titanium (Ti_{5f} , Ti_{6f}) atoms with in-plane threefold coordinated oxygen atoms as shown in Figure 4 [6], [123].

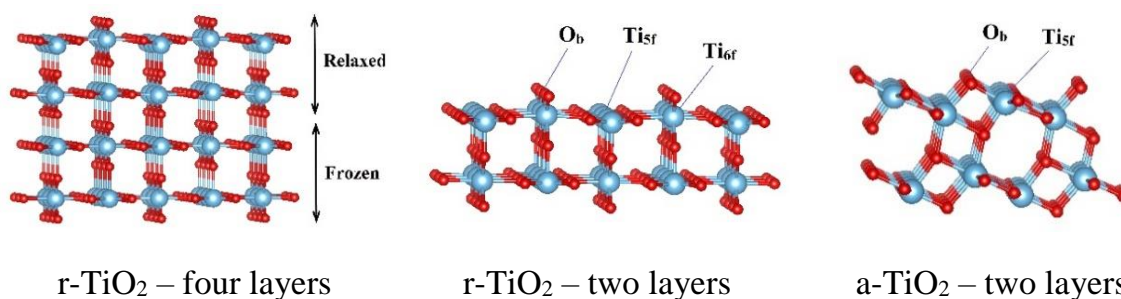


Figure 4. The slab models of rutile- TiO_2 (110) and anatase- TiO_2 (101) surfaces

The simulated surfaces of r- TiO_2 are set up with acceptable dimensions: $a = 13.24 \text{ \AA}$; $b = 9.10 \text{ \AA}$; $c = 25.00 \text{ \AA}$, $a = 17.82 \text{ \AA}$; $b = 13.15 \text{ \AA}$; $c = 35.00 \text{ \AA}$, and $a = 14.85 \text{ \AA}$ $b = 13.15 \text{ \AA}$; $c = 35.00 \text{ \AA}$ for adsorptions of organic molecules (formic acid, acetic acid, benzene derivatives), enrofloxacin (ER), ampicillin (AP); amoxicillin (AX); tetracycline (TC) antibiotics, respectively. Similarly, the a- TiO_2 is selected with special parameters: $a = 11.42 \text{ \AA}$, $b = 10.43 \text{ \AA}$, $c = 20.00 \text{ \AA}$, $a = 15.22 \text{ \AA}$, $b = 20.87 \text{ \AA}$, $c = 30.01$ in considering the adsorption of benzene derivatives and AP, AX antibiotics, respectively. The automatically generated Γ -center k-points grids are used for all the surface-related calculations. The k-points in the reciprocal space are considered and selected at the Gamma center with a ratio of $2 \times 2 \times 1$ or $2 \times 3 \times 1$ for r- TiO_2 and $2 \times 2 \times 1$ or $4 \times 3 \times 1$ for a- TiO_2 based on cell size of investigated systems. The converged plane-wave cut-off energy controlling the number of plane-wave basis

functions for our calculations is chosen at 500 eV. The interaction between the valence electrons and the core is described by the projected augmented wave (PAW) method implemented by Kresse and Joubert [75]. Relaxations of the allowed ionic positions are performed using the conjugate gradient algorithm until the forces on all atoms were smaller than 0.01 eV/Å.

In the present study, the Perdew-Burke-Ernzerhof (PBE) version of generalized-gradient approximation (GGA) accounting for the exchange-correlation effects selected for all the calculations if noted otherwise [104]. Adsorption energy (E_{ads}) and interaction energy (E_{int}) are calculated as in the following expressions:

$$E_{\text{ads}} = E_{\text{comp}} - (E_{\text{surf}} + E_{\text{mol}}) \quad (1.64);$$

$$E_{\text{int}} = E_{\text{comp}} - (E_{\text{surf}}^* + E_{\text{mol}}^*) \quad (1.65)$$

where E_{comp} , E_{surf} and E_{mol} are the energies of the optimized surface-adsorbate system, surface, and molecule, respectively; and E_{surf}^* and E_{mol}^* are single-point energies of the surface and molecule geometries which are kept fixed as in the surface-adsorbate optimized structure. The deformation energies of the adsorbate molecule ($E_{\text{def-mol}}$) and rutile surface ($E_{\text{def-surf}}$) upon the adsorption process are computed as the differences between E_{mol}^* and E_{mol} and E_{surf}^* and E_{surf} , respectively. The optPBE-vdW functional is then considered in some calculations for a full evaluation on adsorption energies [72], [104].

2.2. Clay mineral systems

2.2.1. Adsorption of organic molecules on kaolinite surfaces

Kaolinite, whose chemical formula is $\text{Al}_2\text{Si}_2\text{O}_5(\text{OH})_4$, includes a series of uncharged layers connected by a network of hydrogen bonds between hydrogen-rich facet (kaolinite (001) surface, denoted by H-slab) and oxygen-rich facet (kaolinite (00 $\bar{1}$) surface, denoted by O-slab). The surfaces of kaolinite are shown in Figure 5. The geometric structures of benzene derivatives and kaolinite surfaces are considered and optimized by VASP program. The K^+ -supported kaolinite (001) surface (denoted by K^+ -slab), as shown in Figure 5, is later observed to consider the effect of cation on adsorption ability of molecules on kaolinite.

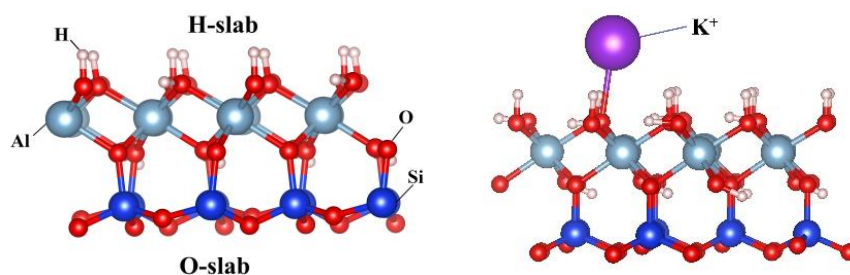


Figure 5. The structure of kaolinite surfaces

In the investigated systems, for H-slab of kaolinite with/without K^+ cation, cell size is designed with dimensional parameters: $a = 10.43 \text{ \AA}$; $b = 9.06 \text{ \AA}$; $c = 25.00 \text{ \AA}$, including a vacuum space *ca.* 15 \AA . The cutoff energy is surveyed and selected at 500 eV. The PBE functional is used in all calculations. The optPBE-vdW functional is also considered in the later systems of K^+ -slab to have a full evaluation of adsorption energies [72], [104]. Some particular parameters, including adsorption energy (E_{ads}), interaction energy (E_{int}), and deformation energies, are computed using the expressions (1.64) and (1.65) above.

2.2.2. Adsorption of antibiotics on vermiculite surface

Geometrical structures of the systems considered were optimized using the GPAW package [39]. This software uses the projector-augmented wave (PAW) method and describes wave functions in real-space orthorhombic grids, following a finite-difference approach. Besides, to model the vermiculite surface, a periodic slab was constructed from crystallographic data available in American Mineralogist Crystal Structure Database [36]. This model is illustrated in Figure 6. In this study, the vermiculite surface contains exclusively Mg^{2+} as the octahedral ions. The Si^{4+} cations in tetrahedral sheets are substituted by Al^{3+} cations in a ratio of 1:3. To perform calculations for the large size of the adsorbed molecule, a single unit cell of the structure was expanded by replication into a 2×1 super-cell defined by $a = 10.70 \text{ \AA}$, $b = 18.51 \text{ \AA}$, $c = 46.64 \text{ \AA}$ and $\alpha = 90.00^\circ$, $\beta = 97.12^\circ$, $\gamma = 90.00^\circ$ lattice parameters (monoclinic structure).

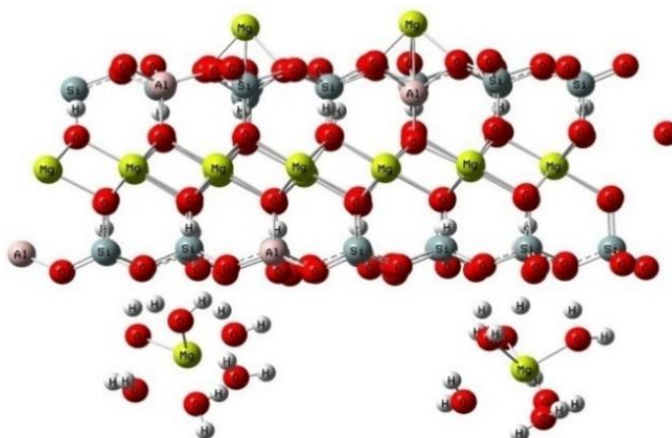


Figure 6. The model slab of vermiculite surface (red, yellow, grey, pink, and white colors displayed for O, Mg, Si, Al, and H atoms, respectively)

For a simplified model, the water molecules hydrating the Mg^{2+} cations external to the surface were removed, and the obtained surface was used as such for all DFT calculations. In the present work, the PBE and the vdW-DF-C09 functionals [25] were selected for geometry optimization and energy calculation. Adsorption energy (E_{ads}) and interaction energy (E_{int}) are thus calculated using both PBE and vdW-DF-C09 functionals by the expressions (1.64) and (1.65). In addition, the deformation energies of the adsorbate molecule ($E_{def-mol}$) and of vermiculite surface ($E_{def-surf}$) are computed similarly to TiO_2 systems.

2.3. Quantum chemical analyses

To have a deeper understanding of the nature of interactions between small organic molecules, antibiotics, and TiO_2 (rutile, anatase) and clay minerals (kaolinite, vermiculite) surfaces, we perform calculations on proton affinity (PA) and deprotonation enthalpy (DPE) for the molecules using the Gaussian 09 program [42] at B3LYP/6-31++G(d,p) level. Topological analysis, electron density ($\rho(r)$) and Laplacian of the electron density ($\nabla^2(\rho(r))$) at bond-critical points (BCPs) are identified using the atoms-in-molecules theory using the AIM 2000 program at the B3LYP/6-31+G(d,p) level [9], [12]. The density potential energy ($V(r)$) and density kinetic energy ($G(r)$) at the BCPs are calculated by the expressions [40], [88]:

$$G(r) = \frac{3}{10} (3\pi^2)^{2/3} \rho^{5/3}(r) + \frac{1}{6} \nabla^2 \rho(r) \quad (1.66); \quad V(r) = \frac{1}{4} \nabla^2 \rho(r) - 2G(r) \quad (1.67).$$

Moreover, the molecular electrostatic potential (MEP) maps for antibiotic molecules were estimated at B3LYP/6-31++G(d,p) level with charge regions ranging from -5.10^{-5} e to 0.15 e to probe the stability of interactions between charged regions in the molecules and the vermiculite surface. Natural bond orbital (NBO) analysis was performed using NBO 5.G software to evaluate electron density transfer between interaction counterparts [134].

PART 3. RESULTS AND DISCUSSION
CHAPTER 1. ADSORPTION OF ORGANIC MOLECULES ON
MATERIALS SURFACES

1.1. Adsorption of organic molecules on rutile-TiO₂ (110) surface

1.1.1. Optimized structures

Performing calculations on adsorption of formic, acetic, and benzoic acids and phenol, nitrobenzene molecules on rutile-TiO₂ (110) surface (r-TiO₂), we obtained the most stable complexes of each adsorbate corresponding to **P1**, **P2**, **P3**, **P4**, and **P5** as shown in Figure 1.1.

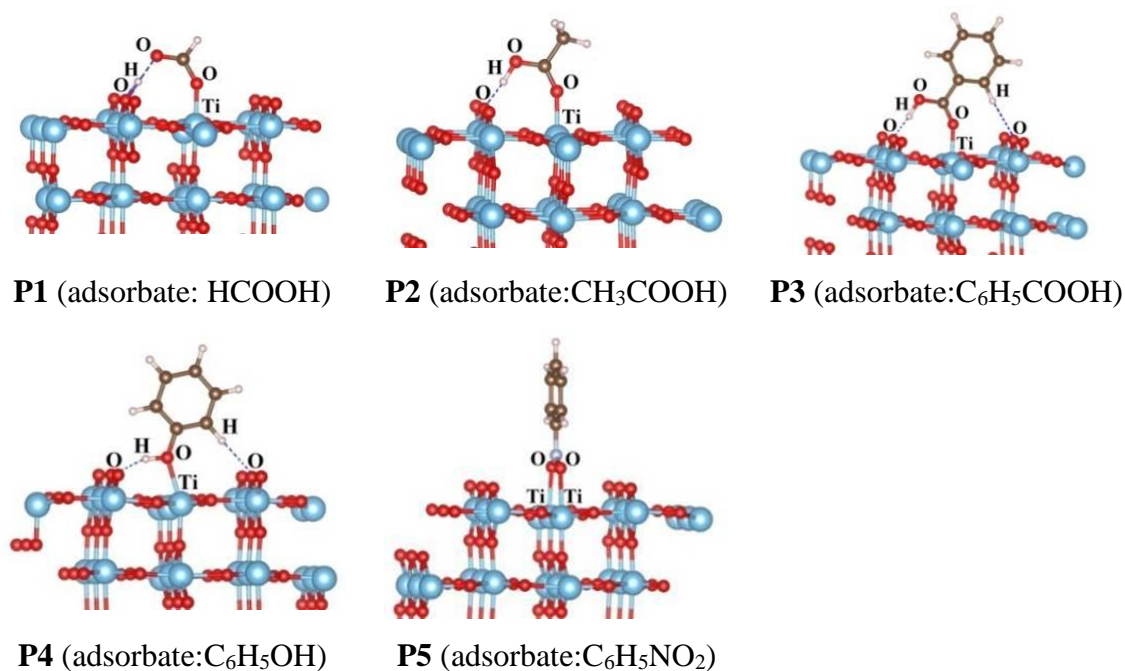


Figure 1.1. Stable complexes for the adsorption of organic molecules on rutile-TiO₂ (110) surface

Table 1.1. Charge distribution in molecules at the B3LYP/6-31+G(d,p) level

	HCOOH	CH ₃ COOH	C ₆ H ₅ COOH	C ₆ H ₅ OH	C ₆ H ₅ NO ₂
q(O) ^(a)	-0.585	-0.451	-0.474	-	-0.393
q(O) ^(b)	-0.706	-0.556	-0.583	-0.664	-
q(H) ^(c)	0.494	0.408	0.412	0.409	-

^(a),b)for O atoms in C(N)=O and O-H groups, ^(c)for H atoms in OH groups.

The NBO charge distribution at atoms in molecules is calculated at B3LYP/6-31+G(d,p) level and tabulated in Table 1.1. Some parameters of optimized structures upon complexation such as interaction distances, bond angles are given in Table 1.2.

Table 1.2. Some selected parameters of stable complexes at PBE functional
(distance (r) in Å; angle (α) in degree)

	Ti \cdots O	O \cdots H	α (TiOC(N))	α (OHO)	Δr (C(N)-O)	Δr (O-H)	Δr (Ti-O)
P1	1.95	1.05 ⁽¹⁾ /1.49 ⁽²⁾	149.4	178.0	0.09	0.51	0.28
P2	2.07	1.50	154.5	176.9	0.04	0.07	0.14
P3	2.06	1.50/2.39*	153.1	176.8	0.04	0.07	0.16
P4	2.22	1.74; 2.17*	145.7	159.0	-0.004	0.03	0.10
P5	2.35/2.38		127.5/126.8	-	0.01	-	0.05

*for C-H \cdots O; ⁽¹⁾for O atom in surface, ⁽²⁾for O atom in formic acid

As displayed in Figure 1.1 and Table 1.2, the distances of Ti \cdots O of 1.95 to 2.35 Å between the O atoms of organic molecules and Ti atoms of the surface are close to the Ti-O bond lengths of the r-TiO₂ (1.80-2.20 Å) [18]. Hence, it is roughly predicted that these are strong interactions upon adsorption. Also, the distances of O \cdots H hydrogen bonds range from 1.49 Å to 2.39 Å upon complexation. Therefore, these contacts can be regarded as stable hydrogen bonds. It is noted that the H atom in -COOH group in **P1** tends to shift to r-TiO₂ to form O_b-H covalent bond with a bond length of 1.05 Å. In short, the stability of these complexes is contributed by both Ti \cdots O interaction and O(C)-H \cdots O hydrogen bond for **P1** to **P4** and only Ti \cdots O interaction for **P5**. The role of -COOH or -OH groups in the stability of complexes is also examined in the previous studies [84], [89], [90], [123], [139].

Considering the complex formation, the Ti \cdots O strong interactions are favorably formed by the Ti atoms of the surface and the highest negative charged O atoms of C=O or O-H group of the molecule, whereas the O(C)-H \cdots O hydrogen bonds are formed between the O atoms of the surface and the largest positive charged H atoms of O-H, C-H bonds of the molecules (*cf.* Table 1.1). Besides, the Ti \cdots O distances increase in the order of the **P1** < **P2** \approx **P3** < **P4** < **P5** complexes. The

$\alpha(\text{TiOC}(\text{N}))$ angles for these interactions range from 126.8 to 154.5° in which the $\alpha(\text{TiOC})$ angles in **P1**, **P2**, **P3** and **P4** are larger than the $\alpha(\text{TiON})$ in **P5**. The O⋯H hydrogen bonds distance increases going from **P1** to **P2** via **P3** and then finally to **P4** complexes. It is noted that the interaction angles of H-O⋯H hydrogen bonds are in the range of 159.0-178.0° in which the largest value appears in **P1** and the smallest one is in **P4**. These values in **P1**, **P2**, and **P3** are close to that of the classical hydrogen bond type (so-called “red-shifting” hydrogen bond) [49]. Consequently, they are evaluated as strong interactions upon complexation.

Further, changes of selected bonding lengths upon adsorption phenomena are also given in Table 1.2. The changes of O-H, C-O, N-O, and Ti-O bond lengths in isolated monomers/surface are quite small, within the range of 0.01 to 0.16 Å for **P2**, **P3**, **P4**, and **P5**. For **P1**, however, the changes of O-H and Ti-O distances are significantly large with the elongation value of 0.51 and 0.28 Å, respectively. This large change leads to the breaking of the O-H bond of the adsorbate to form the new O-H bond on the surface, and accordingly, the Ti atom of the surface tends to move to the molecular adsorbate to form the new Ti-O bond.

1.1.2. Energetic aspects

To evaluate the adsorption process of the molecules on the TiO₂ surface, the adsorption, interaction, and deformation energies (E_{ads} , E_{int} and $E_{\text{def-mol}}$, $E_{\text{def-surf}}$, respectively) are calculated with the PBE functional and given in Table 1.3.

Table 1.3. Adsorption, interaction, and deformation energies (all in kcal.mol⁻¹) for the adsorption processes on rutile-TiO₂ (110) surface

	P1	P2	P3	P4	P5
E_{ads}	-24.2	-26.5	-28.8	-18.5	-18.5
E_{int}	-114.3	-40.8	-43.9	-24.4	-22.6
$E_{\text{def-surf}}$	27.7	8.1	8.9	5.1	2.5
$E_{\text{def-mol}}$	62.4	6.2	6.2	0.8	1.6

Accordingly, the adsorption energies of the investigated organic compounds on r-TiO₂ are highly negative and in the range of -18.5 to -28.8 kcal.mol⁻¹. The adsorption energies of configurations increase in the order of benzoic acid < acetic acid < formic acid < phenol ≈ nitrobenzene. Accordingly, these molecules are strongly adsorbed on r-TiO₂ in which the ability of adsorption decreases from acids to phenol and nitrobenzene. Hence, these processes are characterized as chemical adsorption because of their large negative adsorption energies. Furthermore, the transfer of H atom from O-H bond in the acid molecules to the r-TiO₂ surface and then to form the complex with O··Ti electrostatic attractive interactions is a possible way for anion carboxylate which is dissociated forms on the surface. This result is consistent with the previous studies for adsorption of formic, acetic and benzoic acid on rutile-TiO₂ surface [15], [74], [84], [89], [90], [120], [121], [123].

The interaction energies of these stable complexes, which have not been investigated before, are quite negative, in the range of -22.6 to -114.3 kcal.mol⁻¹. Consequently, the Ti··O and O-H··O interactions on the surface are strong and lead to form stable configurations. As presented in Table 1.3, these energy values decrease in going from nitrobenzene to phenol and finally to acids, in which the largest negative value is obtained for formic acid. This is understood due to the large negative charge densities at O atoms in C=O and C-O bonds and the large positive charge densities at H atoms in O-H bonds for molecules, which decrease in going from acids to phenol and nitrobenzene molecules. The highest values of interaction energy for **P1** result from the formation of the O_b-H covalent bond on r-TiO₂. As a result, the stability of Ti··O and O-H··O hydrogen bond interactions in the complexes decreases in the order of **P1** > **P3** > **P2** > **P4** > **P5**. Hence, we can see that the interactions between the r-TiO₂ and the -COOH groups in **P1**, **P2**, **P3** are stronger than those of -OH, -NO₂ groups in **P4**, **P5**.

Deformation energy is an important parameter for evaluating the ability to separate the substrate and the surface from their stable configurations. As shown in Table 1.3, the deformation energy values for the surface are slightly larger than that

for the molecules, except for **P1** case where the energy for the dissociation of formic acid is larger than that of the surface. Therefore, the ability of separating and then forming stable structures for the surface is less favorable than that for the adsorbed molecules (except for separated monomers in **P1**).

1.1.3. The quantum chemical analysis for the interactions on the surface

To get deeper insights into the interactions between the aforementioned molecules with the r-TiO₂, the charge density, and topological analysis are examined and plotted in Figures 1.2, 1.3, and given in Table 1.4.

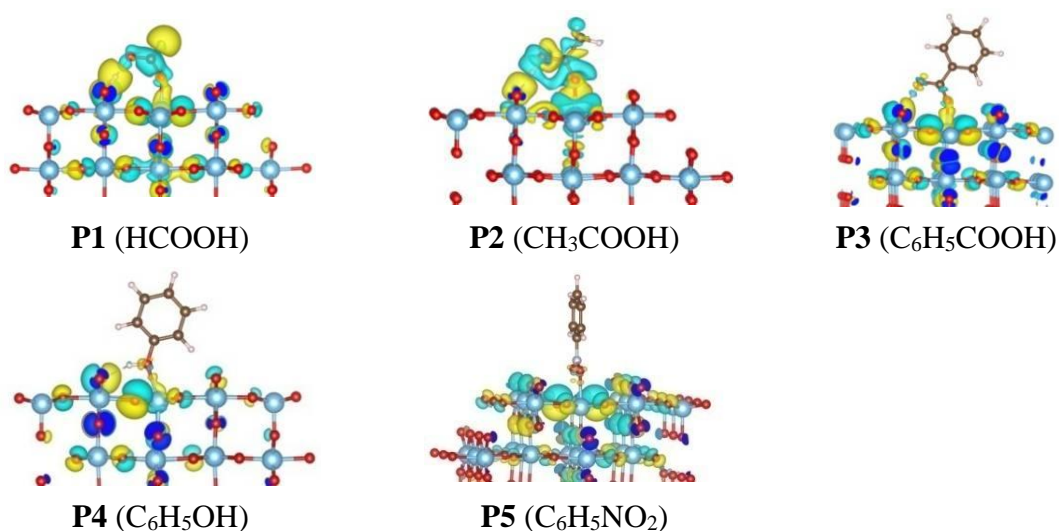


Figure 1.2. The charge density between adsorbent and adsorbates in stable complexes

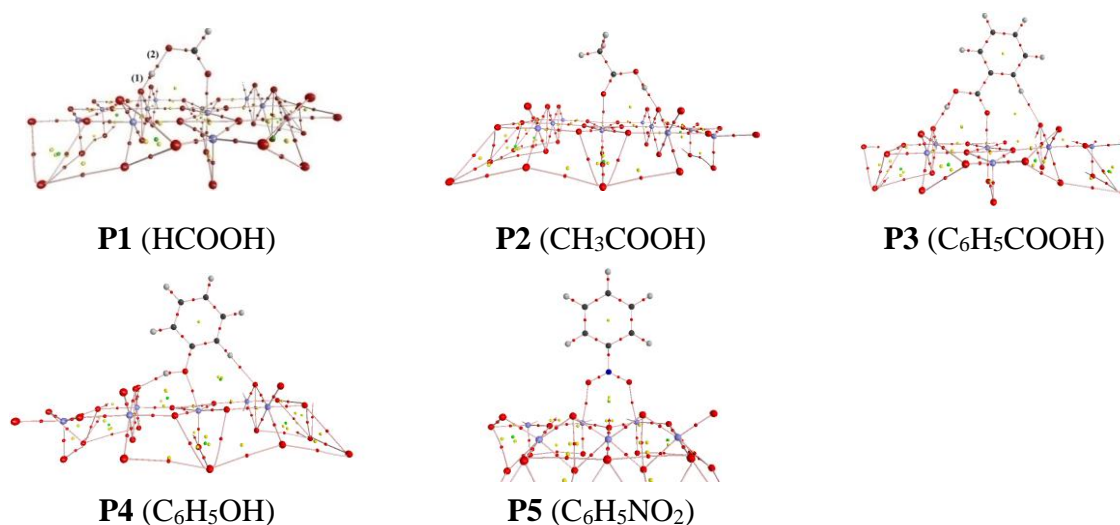


Figure 1.3. The topological analysis for the first-layered structures

The charge distribution upon formation of interactions occurs significantly on the first two-layered structures (see Figure 1.2). In addition, the orbital overlaps

between the atoms directly involved in the interactions further corroborate their formation. The electron density overlaps in **P1**, **P2**, **P3** are more significant than those of **P4**, **P5**, indicating larger stability of interactions in **P1**, **P2**, **P3** relative to in **P4**, **P5**. Hence, the interaction between –COOH group and rutile surface is more favorable than that of –OH and NO₂ groups following the adsorption process.

Table 1.4. The characteristic parameters for topological analysis (all in au)

BCP	P1	P2	P3	P4	P5	
$\rho(r)$	O...Ti	0.097	0.067	0.069	0.045	0.034
	O-H...O	0.257 (1)	0.073	0.073	0.042	0.032
		0.075 (2)		0.011 (C)*	0.017 (C)*	
$\nabla^2(\rho(r))$	O...Ti	0.516	0.389	0.400	0.253	0.167
	O-H...O	-1.084 (1)	0.190	0.187	0.120	0.152
		0.187 (2)		0.036(C)*	0.053 (C)*	

**for C-H...O hydrogen bonds; (1), (2) shown in Fig. 1.3 (P1).*

The presence of BCPs in Figure 1.3 and the values of electron density, its Laplacian in Table 1.4 indicate the existence of intermolecular interactions of O...Ti and H...O as displayed in Figure 1.1. The considerable $\rho(r)$ values of 0.042-0.075 au at BCPs of O-H...O contacts indicate significantly strong interactions of O-H group of the molecules with the O site on the surface. In addition, the $\rho(r)$ values at BCPs of Ti...O intermolecular contacts decrease in the order of **P1** > **P3** > **P2** > **P4** > **P5**, thus the interaction of Ti sites with >C=O groups is stronger than with –OH and –NO₂ groups upon complexation. Consequently, **P1**, **P2**, and **P3** are more stable than **P4**, **P5**. Furthermore, the small electron density values of 0.011 and 0.017 au at BCPs of C-H...O intermolecular contacts in **P3** and **P4** show a slight contribution of the C-H...O hydrogen bonds to the stability of two complexes. Besides, the high values of $\rho(r)$ and $\nabla^2(\rho(r))$ at BCP H...O_b corresponding to 0.257 au and -1.084 au clarify the shifting H atom in HCOOH to r-TiO₂ to form O_b-H covalent bond.

1.1.4. Summary

The stable complexes of adsorption of acids (formic, acetic, benzoic), phenol, and nitrobenzene on rutile-TiO₂ (110) surface (r-TiO₂) are observed using DFT calculations. The adsorption energy of the model organic molecules on the r-TiO₂ is estimated to be in the range of -18.5 to -28.8 kcal.mol⁻¹. Both O··Ti strong interaction and O-H··O hydrogen bond significantly contributed to the stability of complexes. Remarkably, the additional role of C-H··O weak hydrogen bonds to the stability of complexes has been observed for the first time. The adsorption on r-TiO₂ is more favorable for >COOH group than -OH and -NO₂ ones. These processes are characterized as chemical adsorption. The electron density overlap and AIM results provide a clearer understanding of the formation and role of O··Ti and O(C)-H··O intermolecular interactions following complexation.

1.2. Adsorption of benzene derivatives on rutile-TiO₂ (110) and anatase-TiO₂ (101) surfaces

1.2.1. Geometrical structures

Some parameters of geometrical structures of benzene derivatives, rutile-TiO₂ (110) and anatase-TiO₂ (101) surfaces (denoted by r-TiO₂ and a-TiO₂) calculated at PBE functional by VASP are compared to the experiment as shown in Table 1.5. The calculated results indicate that the slight difference of the bond length and angle in the range of 0.00-0.08 Å; 0.5-2.4°, respectively, is achieved in this work as compared to experimental results [18], [97], [126]. Accordingly, the PBE functional selected in the present work is quite reliable for considering this system.

In addition, by using DFT calculations, we obtained 12 stable complexes for each system of interactions between the benzene derivatives, including C₆H₅CHO, C₆H₅COOH, C₆H₅NH₂, C₆H₅OH, and C₆H₅SO₃H and r-TiO₂, a-TiO₂ which denoted by **r-PiX**, **a-PiX** (i = 1- 4, X = -CHO, -COOH, -NH₂, -OH, -SO₃H), respectively. These optimized structures are shown in Figures 1.4 and 1.5. Besides, the selected parameters for complexes are gathered in Tables 1.6 and 1.7.

Table 1.5. Some selected parameters of molecules and TiO₂ surfaces

	Parameters	Calc./Expt.		Parameters	Calc./Expt.
C ₆ H ₅ CHO	r(C=O)	1.23 Å/1.21 Å	C ₆ H ₅ NH ₂	r(N-H)	1.01 Å/-
	r(C-H)	1.12 Å/1.12 Å		r(C-N)	1.40 Å/1.43 Å
	r(C-C)	1.48 Å/1.48 Å		α(HNH)	112.2°/113.8°
	α(OCC)	124.9°/123.6°		α(HNC)	115.4°/114.9°
C ₆ H ₅ COOH	r(H-O)	0.98 Å/0.95 Å	C ₆ H ₅ OH	r(O-H)	0.97 Å/0.96 Å
	r(C-O)	1.37 Å/1.36 Å		r(C-O)	1.38 Å/1.36 Å
	r(C=O)	1.22 Å/1.22 Å		α(HOC)	108.8°/106.4°
	r(C-C)	1.49 Å/1.48 Å	r(S=O)	1.44 Å/-	
a-TiO ₂	Ti-O	1.81-2.10 Å/ 1.89-2.07 Å	C ₆ H ₅ SO ₃ H	r(O-H)	0.98 Å/-
r-TiO ₂	Ti-O	1.83-2.07 Å/ 1.80-2.20 Å		r(C-S)	1.78 Å/-

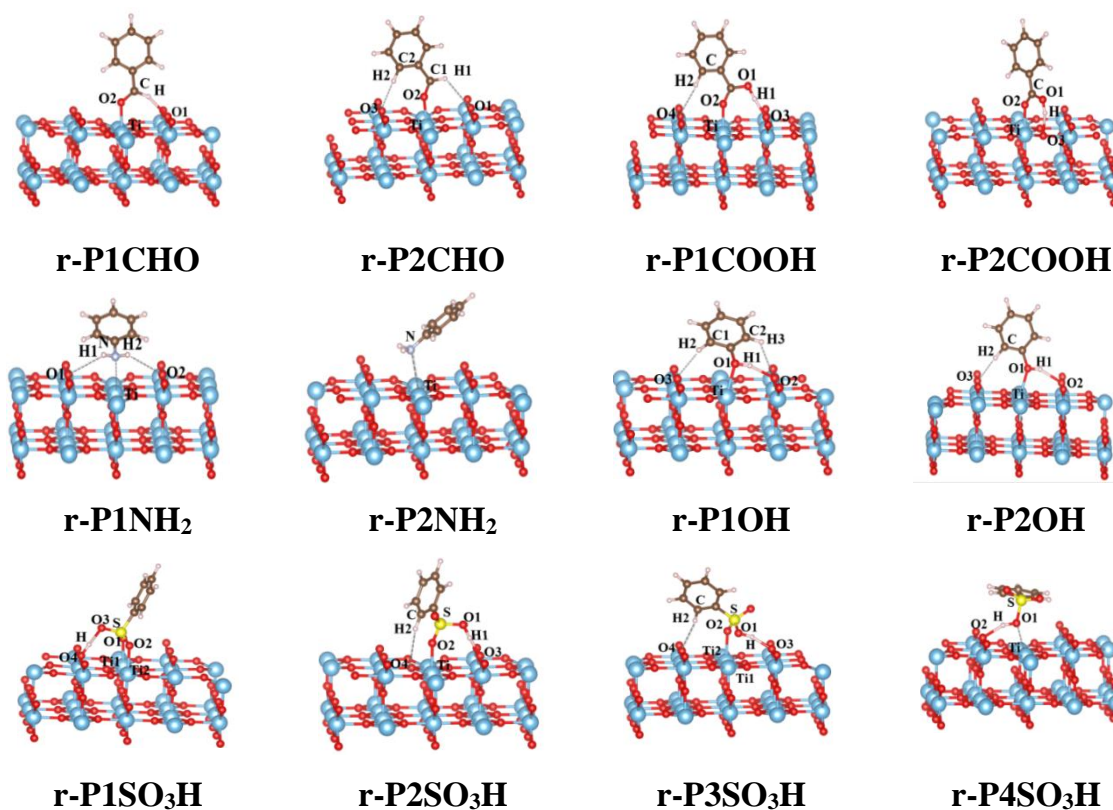
**Figure 1.4.** Stable complexes of adsorption of benzene derivatives on rutile-TiO₂ (110) surface

Table 1.6. Interaction distance (d , Å), bond angle (α , °), and changes in the length of bonds (Δr , Å) following the adsorption process for rutile systems

Complex	$d(\text{Ti}_{5f}\cdots\text{O/N})$	$d(\text{O/C/N-H}\cdots\text{O}_b)$	$\alpha(\text{Ti}_{5f}\text{-O/N-C/S})$	$\alpha(\text{O/C/N-H-O}_b)$	$\Delta r(\text{Ti-O})$	$\Delta r(\text{O/C/N-H})$
r-P1CHO	2.22	2.03	128.1	156.1	0.02	-0.01
r-P2CHO	2.17	2.33*	153.4	153.4	0.02	-0.01
r-P1COOH	2.11	1.56/2.50*	152.3	174.4	0.05	0.05
r-P2COOH	2.19	1.73	136.4	136.4	0.02	0.03
r-P1NH₂	2.37		121.6	121.0	0.02	0.01
r-P2NH₂	2.38	-	122.3	-	0.02	0.01
r-P1OH	2.32	1.88/2.16*	125.6	158.1	0.04	0.03
r-P2OH	2.30	1.90/2.47*	145.7	153.3	0.04	0.03
r-P1SO₃H	2.18 ^a /2.14 ^b)	1.00/1.73 ⁽ⁱ⁾	125.2 ^a)/127.8 ^b)	158.1	0.14	0.75
r-P2SO₃H	2.17	1.46/2.72*	158.3	174.3	0.05	0.08
r-P3SO₃H	2.28	1.66/2.24*	137.7	137.7	0.05	0.05
r-P4SO₃H	2.41	1.74	146.6	157.6	0.04	0.03

*a), b) for $\text{Ti}\cdots\text{O}$ (O_1, O_2 of $-\text{SO}_3\text{H}$ group with 2 atoms of Ti_1, Ti_2); * for $\text{C-H}\cdots\text{O}$; ⁽ⁱ⁾ for $\text{O}_b\text{-H}\cdots\text{O}$ (Ti_{5f} and O_b on TiO_2 surfaces as displayed in Fig. 4 in Part 2)*

Table 1.7. Distance of intermolecular interactions (d , Å), bonding angle (α , °), and changes of bond length (Δr , Å) upon adsorption process for anatase systems

Complex	$d(\text{Ti}_{5f}\cdots\text{O})$	$d(\text{H}\cdots\text{O}_b)$	$\alpha(\text{C/S-O-Ti}_{5f})$	$\alpha(\text{X-H-O}_b)$	$\Delta r(\text{Ti-O})$	$\Delta r(\text{X-H})$
a-P1CHO	2.24		117.8	168.2	0.02	-0.01
a-P2CHO	2.22	2.48	128.8	128.8	0.00	-0.01
a-P1COOH	2.13	1.42	132.5	164.2	0.07	0.08
a-P2COOH	2.18	1.66	132.4	164.6	0.00	0.03
a-P1NH₂	2.34		118.1	118.1	0.01	0.02
a-P2NH₂	-	2.02/2.35*	-	162.2	0.01	0.01
a-P1OH	2.35	2.07/2.16*	152.7	109.0	0.03	0.01
a-P2OH	2.33	2.66*	119.5	-	0.01	0.01
a-P1SO₃H	2.13 ¹)/2.20 ²)	1.00/1.75 ⁽ⁱ⁾	124.5 ¹)/126.4 ²)	154.7	0.17	0.77
a-P2SO₃H	2.03	1.03/1.50 ⁽ⁱ⁾	136.4	160.7	0.13	0.52
a-P3SO₃H	2.26	1.61	138.6	174.7	0.00	0.05
a-P4SO₃H	2.10 ¹)/2.22 ²)	0.99/1.78 ⁽ⁱ⁾	126.2 ¹)/126.8 ²)	154.1	0.17	0.80

*X = C,N,O; * for $\text{C-H}\cdots\text{O}$; ^{1), 2)} for $\text{Ti}\cdots\text{O}$ (Fig. 1.5); ⁽ⁱ⁾ for $\text{O}_b\text{-H}\cdots\text{O}$ (Ti_{5f} and O_b on TiO_2 surfaces as displayed in Fig. 4 in Part 2)*

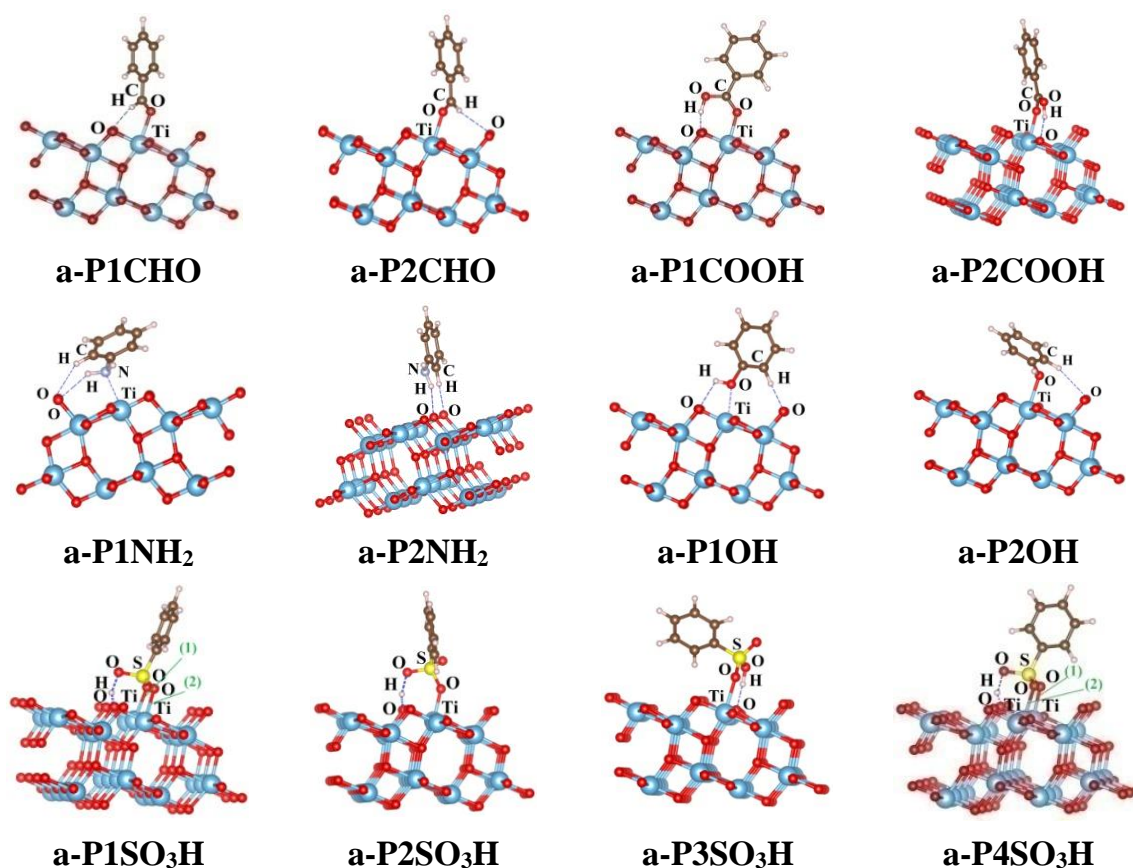


Figure 1.5. Stable structures of adsorption of benzene derivatives on anatase-TiO₂ (101) surface

Tables 1.6 and 1.7 imply that the distances of $\text{Ti}_{5f} \cdots \text{O/N}$ and $\text{O/C/N-H} \cdots \text{O}$ in the complexes are in the range of 2.03-2.41 Å and 0.99-2.72 Å, respectively. These values are all smaller than the total van der Waals radius of the atoms involved in the interactions (the total radius of the atoms Ti and O; Ti and N; O and H are 3.67 Å, 3.85 Å, and 2.72 Å, respectively). Therefore, it is initially suggested that $\text{Ti} \cdots \text{O/N}$ and $\text{O/C/N-H} \cdots \text{O}$ intermolecular contacts exist following the complexation. Notably, the H atom in $-\text{SO}_3\text{H}$ group tends to attach at O_b in $r\text{-TiO}_2$ and $a\text{-TiO}_2$ to form $\text{O}_b\text{-H}$ covalent bonds upon complexation. The stable complexes are formed by interactions between functional groups with the five-coordination Ti atoms (Ti_{5f}) and O atoms at the bridge sites (O_b) on the $r\text{-TiO}_2$ and $a\text{-TiO}_2$ (as shown in Fig. 4 in Part 2).

In addition, the interactive angles such as $\alpha(\text{Ti-O/N-C/S})$ range from 117.8° to 158.3°, in which $\alpha(\text{Ti-O-C/S})$ angles are bigger than $\alpha(\text{Ti-O-N})$. The bonding angles

of $\alpha(\text{O/C/N-H-O})$ are in the range of 109.0° - 174.7° , where the largest and smallest angles are found in the **r-P2SO₃H**; **a-P4SO₃H** and **r-P1NH₂**; **a-P1OH**, respectively. The magnitude of these angles is close to the bonding angles in the formation of O/C-H \cdots O hydrogen bonds in previous studies [49], [127]. Also, the lengths of Ti-O and O/C/N-H bonds are increased in the range of 0.02-0.17 Å and 0.01-0.80 Å, respectively. Remarkably, the changes of O-H and Ti-O bonds in **r-P1SO₃H**, **a-P1SO₃H**, **a-P4SO₃H** are more significant than those in other complexes. This is due to the high flexibility of the H atom in the -SO₃H group for shifting to the r-TiO₂ as well as a-TiO₂ as compared to other groups. The tendency of flexible H atom transferred in acid functional groups is consistent with the previous reports [85], [121]. Hence, the obtained complexes are stabilized by Ti_{5f} \cdots O interactions and O/N/C-H \cdots O hydrogen bonds.

1.2.2. Energetic aspects of the adsorption process

The energy aspects for stable configurations are listed in Tables 1.8 and 1.9.

Table 1.8. Adsorption, interaction, and deformation energies of adsorption of benzene derivatives on rutile-TiO₂ (110) surface (all in kcal.mol⁻¹)

Complex	E _{ads}	E _{int}	E _{def-surf}	E _{def-mol}
r-P1CHO	-18.0	-22.8	3.8	1.0
r-P2CHO	-17.2	-21.8	3.7	0.9
r-P1COOH	-24.2	-35.0	6.4	4.4
r-P2COOH	-18.0	-25.5	5.2	2.3
r-P1NH₂	-19.0	-23.0	2.9	1.0
r-P2NH₂	-15.2	-19.7	3.3	1.2
r-P1OH	-15.3	-20.0	3.9	0.8
r-P2OH	-14.0	-18.9	4.0	0.9
r-P1SO₃H	-31.1	-146.7	25.2	90.3
r-P2SO₃H	-20.5	-33.2	5.8	6.9
r-P3SO₃H	-18.6	-28.8	6.7	3.5
r-P4SO₃H	-12.9	-16.4	3.4	0.0

Table 1.9. Energetic aspects of adsorption of benzene derivatives on anatase-TiO₂ (101) surface (all in kcal.mol⁻¹)

Complex	E_{ads}	E_{int}	E_{def-surf}	E_{def-mole}
a-P1CHO	-14.7	-18.7	3.3	0.7
a-P2CHO	-15.1	-19.6	3.7	0.7
a-P1COOH	-22.8	-34.4	6.3	5.3
a-P2COOH	-15.8	-23.7	5.6	2.3
a-P1NH₂	-18.6	-22.7	3.1	1.0
a-P2NH₂	-3.4	-3.9	0.1	0.3
a-P1OH	-9.7	-12.6	2.1	0.7
a-P2OH	-9.8	-12.7	1.7	1.2
a-P1SO₃H	-27.8	-146.2	28.6	89.8
a-P2SO₃H	-21.7	-104.5	16.1	66.7
a-P3SO₃H	-12.2	-20.4	5.1	3.0
a-P4SO₃H	-29.1	-151.5	29.4	92.9

The adsorption energy values of the complexes are largely negative, ranging from -12.9 to -31.1 kcal.mol⁻¹ and from -3.4 to -29.1 kcal.mol⁻¹ for rutile and anatase systems, respectively. It is noted that adsorption energy values increase in the following order: -SO₃H < -COOH < -NH₂ < -CHO < -OH when they are adsorbed on r-TiO₂ or a-TiO₂. Thus, the adsorption ability of these molecules on r-TiO₂ and a-TiO₂ decreases in the ordering of -SO₃H > -COOH > -NH₂ > -CHO > -OH. This result shows that organic molecules containing acid functional groups (-SO₃H, -COOH) have stronger adsorption on TiO₂ surfaces than other ones (containing -OH, -CHO, -NH₂ groups). This is also similar to the previous investigation on adsorption of organic molecules on rutile-TiO₂ surface [85].

In addition, the interaction energy is also an important characteristic for evaluating the adhesion of molecules on material surfaces. As shown in Tables 1.8 and 1.9, the E_{int} values are in the range of -16.4 to -146.7 kcal.mol⁻¹ and -3.9 to -151.5 kcal.mol⁻¹ for rutile and systems, respectively. It is remarkable that, the interaction

energy values increase in the sequence: $-\text{SO}_3\text{H} \ll -\text{COOH} < -\text{NH}_2 < -\text{CHO} < -\text{OH}$ derivatives. The significantly negative values obtained for $-\text{SO}_3\text{H}$ derivatives are understood by the convenient transfer of the H atom in the $-\text{SO}_3\text{H}$ group to the TiO_2 surfaces upon formation of the $\text{O}_b\text{-H}$ covalent bonds.

Furthermore, deformation energy is also a special parameter to consider the changes in structures of molecule and surface upon the adsorption process. Tables 1.8 and 1.9 show that the deformation energy values are relatively small (excepted for complexes of $-\text{SO}_3\text{H}$), in which the values are smaller for the molecule than for the surface. Therefore, the structures of molecules are less distorted than the surfaces. For $-\text{SO}_3\text{H}$ derivative, the significant changes are found in both molecule and surface. The molecule is a good proton-donor (at $-\text{SO}_3\text{H}$ group) whereas the surface is regarded as a potential proton-acceptor (at O sites). This is expressed from shifting of H in $-\text{SO}_3\text{H}$ to r- TiO_2 and a- TiO_2 in the geometrical analysis above. As a consequence, the distortion of molecules in their complexes decreases in going from $-\text{SO}_3\text{H}$ to $-\text{COOH}$, $-\text{NH}_2$, $-\text{CHO}$, and finally to $-\text{OH}$.

1.2.3. Formation and role of intermolecular interactions

1.2.3.1. MEP maps and NBO charge of molecules

To evaluate the interactive ability at the sites of molecules, we perform calculations on molecular electrostatic potential (MEP) and NBO charge for benzene's derivatives. The results are illustrated in Figure 1.6 and tabulated in Table 1.10.

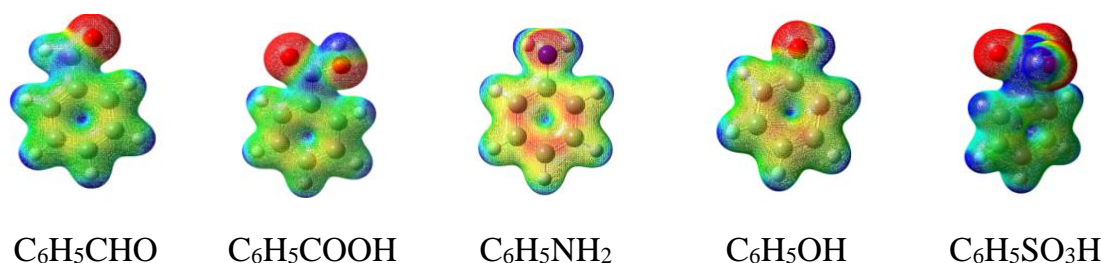


Figure 1.6. MEP maps of benzene derivatives (isovalue = 0.02 au, charge region taken in the range of $2 \cdot 10^{-3}$ to 0.15 e)

Colors displayed on the MEP maps correspond to the charge density regions that change from negative to positive regions in the ordering of red (most negative)

< orange < yellow < green < blue (most positive). As shown in the MEP maps, the positive charge density is mainly located at H atoms in O-H, N-H, C-H groups, in which the density is reduced from O-H to N-H and finally to C-H. The negative charge density is found at O, N atoms in functional groups. As a matter of fact that, the electrostatic interaction would be preferred formed between Ti^{4+} (Ti_{5f}) and O^{2-} (O_b) sites on the surface and high charge density regions at O/N and H atoms of molecules, respectively.

Table 1.10. NBO charges at atoms in functional groups involved in interactions in complexes

	R-CHO	R-COOH	R-NH₂	R-OH	R-SO₃H
q(O)^a	-0.542	-0.507	-	-	-0.936/-0.907
q(O)^b	-	-0.732	-0.873	-0.714	-0.929
q(H)	0.152	0.525	0.414	0.509	0.538
q(C,S)	0.393	0.802	-	-	2.367

R = C₆H₅-; ^a) for O atoms in C/S=O groups; ^b) for O/N atoms in O/N-H groups

In addition, Table 1.10 presents the negative charge density at O/N atoms in functional groups decreases in the ordering of $-SO_3H > -NH_2 > -COOH > -OH > -CHO$. Similarly, the positive charge density at H decreases in the sequence of $-SO_3H > -COOH > -OH > -NH_2 > -CHO$. Hence, the ability to form electrostatic interactions of $Ti \cdots O/N$ and $H \cdots O$ in complexes is more favorable for $-SO_3H$ derivatives than for $-COOH$ and much stronger than $-NH_2$, $-OH$, $-CHO$. Hence, the strength of complexes decreases in the order of $-SO_3H > -COOH > -OH > -NH_2 > -CHO$ derivatives.

1.2.3.2. Deprotonation enthalpy and proton affinity at sites of molecules

To clarify the formation of stable interactions, some characteristic thermodynamic quantities including proton affinity (PA) and deprotonation energy (DPE) are calculated at B3LYP/6-31++G(d,p) and given in Table 1.11.

Table 1.11 indicates the PA values obtained at the B3LYP/6-31++G(d,p) level are close to the experimental values (errors of 0.2-8.5%) [97]. The PA values at O/N atoms in the functional groups decrease in the following order: $-NH_2 > -CHO > -$

COOH > -SO₃H implying that the ability of formation Ti_{5f}···N electrostatic interactions is stronger than that for Ti_{5f}···O. The trend of Ti_{5f}···O formation in derivatives has followed the ordering of -CHO > -COOH > -SO₃H > -OH.

Table 1.11. Proton affinity (PA) at O and N atoms and deprotonation enthalpy (DPE) of O-H and N-H bonds in functional groups and C-H bonds in the benzene ring of derivatives (in kcal.mol⁻¹)

Molecules	PA			DPE		
C₆H₅CHO	203.2*	199.3**	404.3 ^{a)}	397.4 ^{b)}	401.8 ^{c)}	400.2 ^{d)}
C₆H₅COOH	195.7*	196.2**	356.4 ^{a)}	407.2 ^{b)}	405.2 ^{c)}	402.9 ^{d)}
C₆H₅NH₂	210.4*	210.9**	383.7 ^{a)}	409.5 ^{b)}	415.3 ^{c)}	416.7 ^{d)}
C₆H₅OH	178.8*	195.5**	362.5 ^{a)}	409.5 ^{b)}	412.1 ^{c)}	413.0 ^{d)}
C₆H₅SO₃H	192.2*		341.1 ^{a)}	391.1 ^{b)}	394.9 ^{c)}	391.0 ^{d)}

* for O/N atoms in functional groups; ** experimental value; a) for C/O/N-H in functional groups; b),c),d) for the C-H bonds in the benzene ring at the ortho-, meta-, and para- sites, respectively

Besides, the deprotonation energy (DPE) values at the O/N/C-H bonds in molecules decrease in the sequence of -SO₃H > -COOH > -OH > -NH₂ > -CHO. This leads to the ability to form stable hydrogen bonds reduces in going from O-H···O to N-H···O and finally to C-H···O. Further, DPE values at O/ N/C-H bonds in functional groups are smaller than at C-H bonds in benzene rings. Therefore, the C-H···O hydrogen bonds formed at sites of benzene ring are pretty weak in comparison to other O/N/C-H···O contacts.

1.2.3.3. AIM and NBO analyses

To gain insight into the origin and role of intermolecular interactions in the adsorption of derivatives on r-TiO₂ and a-TiO₂, we perform quantum chemical analyses based on AIM, and NBO approaches. The first-layered structures of the most stable structures are considered suitably in these computations. The topological geometries and EDT maps are displayed in Figures 1.7, 1.8, 1.9, and 1.10. Some selected parameters are presented in Tables 1.12 and 1.13.

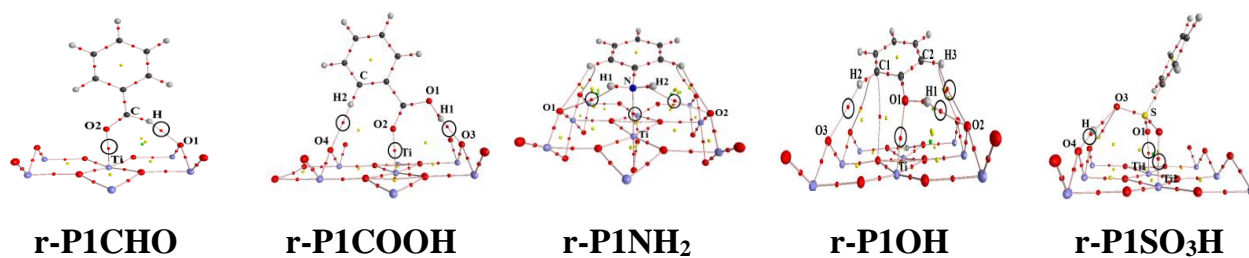


Figure 1.7. Topological geometry of the first-layered structures of the most stable complexes for rutile systems

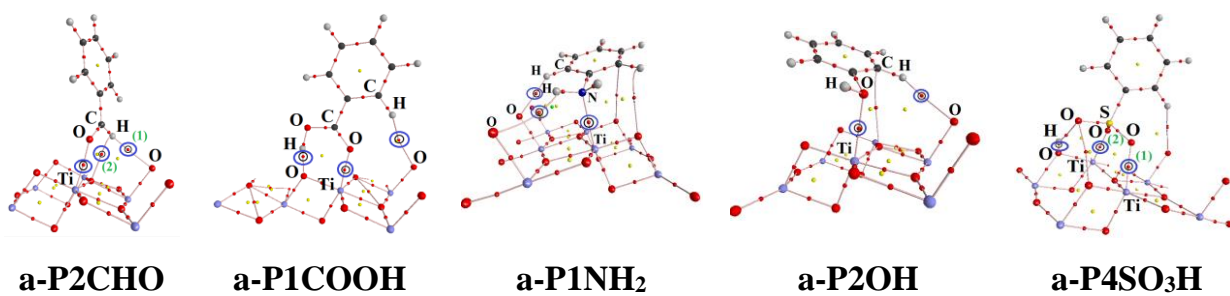


Figure 1.8. Topological geometry of the first-layered structures of the most stable complexes for anatase systems

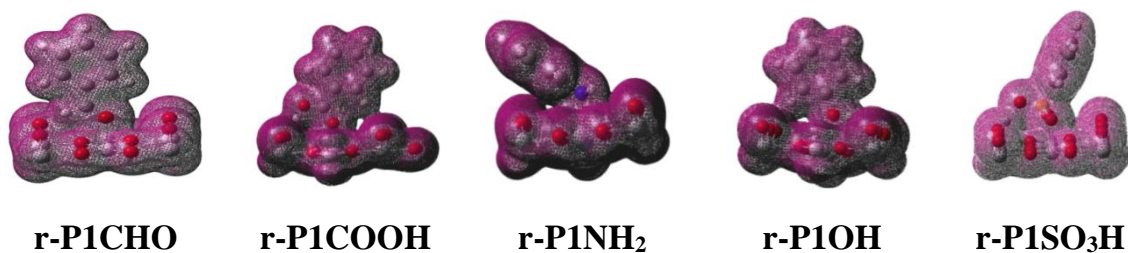


Figure 1.9. EDT maps of investigated structures for rutile systems

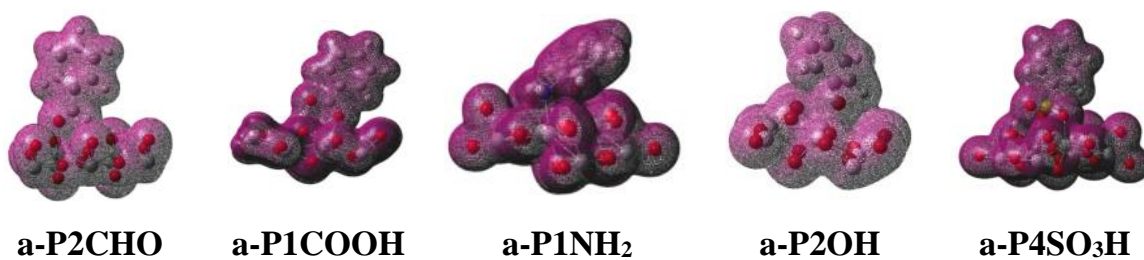


Figure 1.10. EDT maps of investigated structures for anatase systems

Table 1.12. Characteristic parameters for topological geometry ($\rho(r)$, $\nabla^2(\rho(r))$, $H(r)$, in au), EDT (in e) for rutile systems

Complex	BCPs	$\rho(r)$	$\nabla^2\rho(r)$	$H(r)$	EDT
r-P1CHO	Ti \cdots O ₂	0.048	0.232	0.006	0.09
	C-H \cdots O ₁	0.023	0.068	-0.001	
r-P1COOH	Ti \cdots O ₂	0.062	0.319	0.007	0.13
	O ₁ -H ₁ \cdots O ₃	0.061	0.160	-0.006	
	C ₂ -H ₂ \cdots O ₄ *	0.008	0.027	0.001	
r-P1NH₂	Ti \cdots N	0.044	0.019	0.001	0.24
	N-H ₂ \cdots O ₂	0.005	0.167	0.005	
	N-H ₁ \cdots O ₁	0.004	0.020	0.001	
r-P1OH	Ti \cdots O ₁	0.038	0.167	0.005	0.07
	O ₁ -H ₁ \cdots O ₂	0.028	0.080	-0.001	
	C ₁ -H ₂ \cdots O ₃ *	0.009	0.031	0.001	
	C ₂ -H ₃ \cdots O ₂ *	0.006	0.022	0.001	
r-P1SO₃H	Ti ₁ \cdots O ₁	0.053	0.261	0.006	-0.73
	Ti ₂ \cdots O ₂	0.059	0.287	0.006	
	O-H \cdots O _b	0.309	-1.739	-0.500	
	O _b -H \cdots O	0.039	0.122	-0.003	

* BCP of C-H group in benzene ring with O atom of the surface

As shown in Figures 1.7, 1.8, the BCPs of Ti \cdots O and O/C/NH \cdots O contacts exist in the complexes. This further implies the formation of intermolecular contacts between functional groups in organic molecules and r-TiO₂, a-TiO₂ as suggested above. Additionally, the electron density values at BCPs are quite large, in the range of 0.004-0.091 au, and Laplacian ($\nabla^2(\rho(r))$) values are in the range of 0.016-0.333 au (except for H \cdots O_{surf} in complexes of -SO₃H) (cf. Tables 1.12, 1.13). It is noted that all of these values are within the range of values for the formation of non-covalent interaction [9], [49], [50], [76], these Ti \cdots O and O/C/N-H \cdots O contacts are thus evaluated to be stable noncovalent interactions.

Table 1.13. Characteristic parameters for topological geometry ($\rho(r)$, $\nabla^2(\rho(r))$, $H(r)$, in au), EDT (in e) for anatase systems

Complex	BCPs	$\rho(r)$	$\nabla^2\rho(r)$	$H(r)$	EDT
a-P2CHO	Ti \cdots O	0.048	0.238	0.007	
	C-H \cdots O ⁽¹⁾	0.012	0.048	0.002	0.14
	C-H \cdots O ⁽²⁾	0.010	0.032	0.001	
a-P1COOH	Ti \cdots O	0.060	0.307	0.006	0.09
	O-H \cdots O	0.091	0.146	-0.032	
a-P1NH₂	Ti \cdots N	0.045	0.172	0.003	
	N-H \cdots O	0.004	0.016	0.001	0.53
	C-H \cdots O	0.011	0.038	0.001	
a-P2OH	Ti \cdots O	0.038	0.172	0.005	0.12
	C-H \cdots O	0.006	0.021	0.001	
a-P4SO₃H	Ti \cdots O ⁽¹⁾	0.065	0.333	0.006	
	Ti \cdots O ⁽²⁾	0.048	0.237	0.006	
	O-H \cdots O _b	0.325	-1.821	-0.524	-0.52
	O _b -H \cdots O	0.037	0.108	-0.003	

^{(1), (2)} as shown in Fig. 1.5

For complexes of -SO₃H, the electron density values at O_b \cdots H BCPs (*ca.* 0.309 - 0.325 au) are considerably predominant in comparison to other ones. Further, the $\nabla^2(\rho(r))$ and $H(r)$ at these BCPs have large negative values, indicating the O_b \cdots H bonds are covalent. This result suggests that the H atom in the -SO₃H group shifts to the surfaces of r-TiO₂ and a-TiO₂ to form O_b-H bonds and then O_b-H \cdots O hydrogen bonds following the complex formation. Moreover, the high values of $\rho(r)$ at O_b-H \cdots O BCPs in **r-P1SO₃H** and **a-P4SO₃H** *ca.* 0.04 au imply that O_b-H \cdots O contacts are quite strong and remarkably contribute to the stability of complexes.

Besides, the tendency of changes in the strength of interactions in complexes is observed in detail. The electron densities at BCPs of Ti \cdots O/N contacts decrease in the order of -COOH \approx -SO₃H > -CHO \approx -NH₂ \approx -OH derivatives. Similarly, the $\rho(r)$

values at BCPs of C/N/O-H \cdots O are reduced in the sequence: -SO₃H \gg -COOH $>$ -OH \approx -CHO \approx -NH₂. Hence, Ti \cdots O and O-H \cdots O interactions are significantly vital in complexes of -SO₃H derivatives and reduced following the order: -SO₃H \gg -COOH $>$ -CHO \approx -NH₂ \approx -OH. This result is consistent with the change of interaction energy of these complexes.

In addition, EDT is also an important characteristic to clarify the formation of intermolecular interactions. As shown in Figures 1.9 and 1.10, the overlaps of electron density at atoms involved in interactions are found following formations of Ti \cdots O and H \cdots O contacts. The EDT values in most of the complexes are positive (in the range of 0.07-0.53 e) (except for -SO₃H derivative), indicating that the electron transfers are from molecules to r-TiO₂ or a-TiO₂ surface stronger than the reverse transfers are. For complexes of -SO₃H derivative, the large negative EDT values (ranging from -0.52 to -0.73 e) imply that the transfers of electron density from the surface to molecules are substantial and more than the converse transfer. This result gives the superior strength of interactions such as O-H \cdots O in the complexes of -SO₃H derivative as compared to other ones.

1.2.4. Summary

Twenty-four stable structures are obtained of the adsorption of organic molecules containing benzene rings on the surfaces of TiO₂ (r-TiO₂ and a-TiO₂). The adsorption energy values are in the range of -12.9 to -31.1 kcal.mol⁻¹ and -3.4 to -29.1 kcal.mol⁻¹ for rutile and anatase systems, respectively. These processes are determined as chemical adsorptions. Besides, the interaction between functional groups of molecules and surface is considerably strong with associated energy in the range of -16.4 to -146.7 kcal.mol⁻¹ for rutile's complexes and of -3.9 to -151.5 kcal.mol⁻¹ for anatase ones. The quantum chemical analyses indicate the stability of the complexes is significantly contributed by both Ti \cdots O/N and O/C/N-H \cdots O intermolecular interactions for remaining derivatives. Overall, the adsorption ability of molecules on r-TiO₂ and a-TiO₂ decreases in the ordering of -SO₃H $>$ -COOH $>$ -NH₂ $>$ -CHO $>$ -OH derivatives.

1.3. Adsorption of benzene derivatives on kaolinite (001) surface

1.3.1. Optimized geometries

The optimized structures of benzene derivatives adsorbed onto kaolinite (001) surface (denoted by H-slab) are based on configurations: i) vertical structure in which the interactions are formed between functional groups and surface (**P1** type), and ii) parallel structure in which the interactions are focused at the benzene ring (**P2** type). These complexes are shown in Figure 1.11. Accordingly, the stability of **P1** complexes is contributed by O/N/C-H \cdots O contacts. For **P2** complexes, the H \cdots π and O/N/C-H \cdots O are significant terms in stabilization. Some selected parameters of complexes' structures are tabulated in Table 1.14.

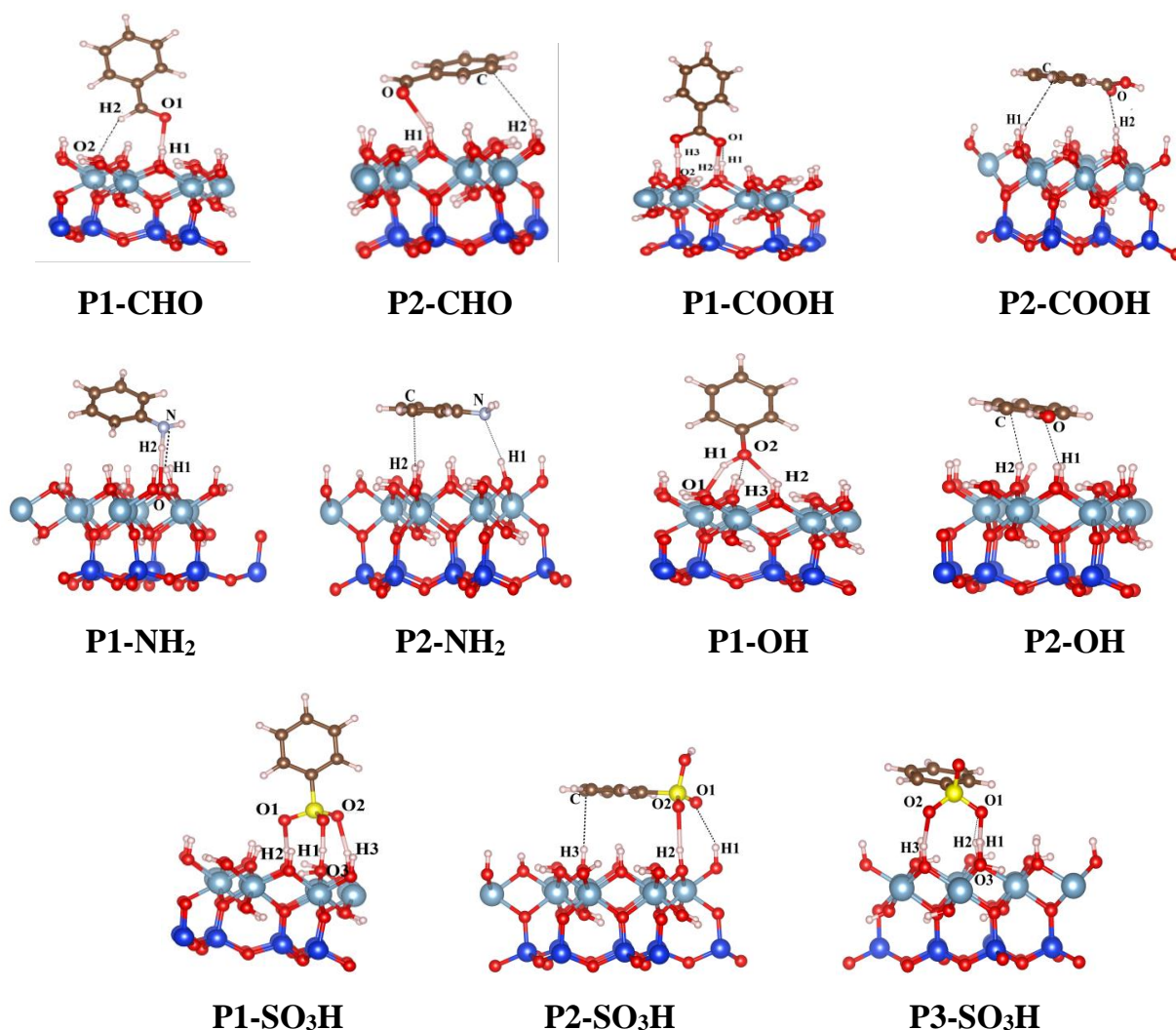


Figure 1.11. Stable structures of adsorption of derivatives on H-slab

Table 1.14. Distances of intermolecular contacts (d), changes in the bond lengths (Δr) involved in interactions in complexes (all in Å)

Complex	d(H \cdots O)	d(H \cdots C/N)	Δr (C/S-O)	Δr (C/O/N-H)	Δr (C/S=O)	Δr (H-O) ^{e)}
P1-CHO	1.77/2.58 ^{a)}	-	-	0.00	0.01	0.02
P2-CHO	2.07	3.12	-	-0.01	0.01	0.01
P1-COOH	1.72/1.61 ^{a)} /2.52	-	-0.03	0.06	0.02	0.02
P2-COOH	2.12	3.25	-0.01	0.00	0.01	0.01
P1-NH₂	1.92 ^{a)}	2.81 ^{b)}	-	0.02	-	0.01
P2-NH₂	-	3.18/2.25 ^{b)}	-	0.00	-	0.00
P1-OH	1.87/ 2.51/1.75 ^{a)}	-	0.00	0.03	0.03	0.01
P2-OH	2.38	2.61	0.01	0.00	-	0.00
P1-SO₃H	1.05 ^{a)} /1.48 ⁽ⁱ⁾ /1.92/1.81	-	-0.13	-	-	0.02
P2-SO₃H	2.05/2.33	2.84	-0.01	0.00	0.01	0.01
P3-SO₃H	1.06 ^{a)} /1.46 ⁽ⁱ⁾ /1.80/2.13	-	-0.12	-	0.04	0.02

^{a)} for O-H \cdots O_{surf} (surface), ^{b)} for H \cdots N, ^{c)} for O-H of surface, ⁽ⁱ⁾ for O_{surf}-H \cdots O

Table 1.14 shows the distances of H \cdots O, H \cdots N and H \cdots C/ π (benzene ring) in the complexes are in the range of 1.46-2.58 Å, 2.25-2.81 Å, and 2.61-3.25 Å, respectively. These values are mostly smaller than the total van der Waals radius of the two atoms involved directly in interactions (the Van der Waals radius of H, C, N, O are 1.20 Å, 1.70 Å, 1.55 Å, and 1.50 Å, respectively). Therefore, it can be suggested that the hydrogen bonds of O/N/C-H \cdots O/ π are formed in investigated complexes. For **P1-NH₂** and complexes of **P2** type, the H \cdots N and H \cdots C(π) contacts exist although their distances are *ca.* 2.81 Å and 2.61-3.25 Å, respectively, slightly larger than the total van der Waals radius of H and N/C atoms. Furthermore, the changes of C-H, C=O, S=O, S-O, N-H, O-H bonds length in molecules are pretty small, *ca.* 0.06 Å. Some C-O (in C-O-H) and S-O (in S-O-H) bonds are shortened in the range of 0.01-0.13 Å upon complexation. In general, the formation of stable complexes leads to small changes in the geometrical structures of molecule and surface.

Remarkably, the H \cdots O_{surf} distance in **P1-SO₃H** and **P3-SO₃H** is *ca.* 1.0 Å, close to the O-H bond length in the organic molecules (*ca.* 0.98 Å, [97]). This implies that the H atom in the -SO₃H group strongly shifts to the H-slab of kaolinite to form

$O_{\text{surf}}\text{-H}$ covalent bond following the adsorption process. The hydrogen bonds of $O_{\text{surf}}\text{-H}\cdots\text{O}$ ($-\text{SO}_3^-$) are then formed upon adsorption with associated distances of 1.5 Å. The tendency of shifting of H atom in the strongly polarized bonds of acid groups such as $-\text{COOH}$, $-\text{SO}_3\text{H}$ to material surfaces in this work is reasonable with the previous studies [85], [121].

1.3.2. Energetic aspects of the adsorption process

To gain an evaluation about the ability of adsorption of molecules on the H-slab surface, the characterized parameters, including adsorption energy (E_{ads}), interaction energy (E_{int}) of complexes, and deformation energies of molecules ($E_{\text{def-mol}}$) and surface ($E_{\text{def-surf}}$) are calculated and given in Table 1.15.

Table 1.15. Energetic parameters of complexes, molecules and surface upon adsorption processes (in kcal.mol⁻¹)

Complex	E_{ads}	E_{int}	$E_{\text{def-surf}}$	$E_{\text{def-mol}}$
P1-CHO	-7.7	-9.3	0.9	0.8
P2-CHO	-5.5	-6.9	0.8	0.6
P1-COOH	-16.2	-23.4	2.9	4.3
P2-COOH	-3.5	-4.6	0.6	0.5
P1-NH₂	-5.4	-6.8	0.8	0.6
P2-NH₂	-4.8	-5.9	0.8	0.3
P1-OH	-11.0	-15.1	1.7	2.4
P2-OH	-3.0	-3.6	0.5	0.1
P1-SO₃H	-24.8	-99.2	14.6	59.8
P2-SO₃H	-6.0	-7.6	1.4	0.2
P3-SO₃H	-19.6	-94.2	16.7	58.0

As shown in Table 1.15, the adsorption energy of the complexes is in the range of -3.0 to -24.8 kcal.mol⁻¹, in which complexes of **P1** type have more negative energy than those of **P2** type. Therefore, **P1** complexes are more stable than **P2**. In addition, interactive energy values of **P1**, **P2** complexes range from -6.8 to -99.2 kcal.mol⁻¹

and -3.6 to -7.6 kcal.mol⁻¹, respectively. This confirms the higher strength of **P1** complexes in comparison to **P2**.

When considering the most stable complexes for derivatives containing different functional groups, it can be found that the changes of E_{ads} and E_{int} values are in the increasing order: $-\text{SO}_3\text{H} < -\text{COOH} < -\text{OH} < -\text{CHO} < -\text{NH}_2$. Hence, the stability of complexes decreases in the sequence: $-\text{SO}_3\text{H} > -\text{COOH} > -\text{OH} > -\text{CHO} > -\text{NH}_2$. The results also indicate that these processes are mostly regarded as physical adsorptions (excepted for $-\text{SO}_3\text{H}$ derivative) and reduced to $-\text{COOH}$, $-\text{OH}$, $-\text{CHO}$, and finally to $-\text{NH}_2$. The chemisorption is found out for $-\text{SO}_3\text{H}$ derivative due to its highly negative adsorption energy.

Moreover, the E_{ads} and E_{int} values of **P1-SO₃H** and **P3-SO₃H** are more highly negative than **P2-SO₃H** (in complexes of $-\text{SO}_3\text{H}$ derivative) and other complexes due to H atom in the $-\text{SO}_3\text{H}$ group is conveniently shifted to the kaolinite surface upon the formation of $\text{O}_{\text{surf}}\text{-H}$ covalent bond. The transfer of H atom in functional groups would lead to considerable changes in molecular and surface structures. This is clarified by the deformation energy ($E_{\text{def-mol}}$, $E_{\text{def-surf}}$) of molecules and surface which are separated from stable configurations. The deformation energy values in **P1-SO₃H** and **P3-SO₃H** are about 60 kcal.mol⁻¹ for molecules and about 17 kcal.mol⁻¹ for surface, respectively. For the rest of the complexes, the deformed energies are *ca.* 0.1-4.3 kcal.mol⁻¹ (cf. Table 1.15). Thus, the geometrical structures of molecule and surface in complexes of $-\text{SO}_3\text{H}$ derivative are considerably distorted, whereas the changes in geometry for other derivatives' complexes are weak.

1.3.3. Formation and role of intermolecular interactions

1.3.3.1. Deprotonation enthalpy of bonds and proton affinity at atoms in molecules

To gain a deeper insight into the existence and strength of intermolecular interactions, we carried out calculations on DPE of O-H, C-H, N-H bonds, and PA at O, N atoms involved in the interactions, as well as the NBO charge for atoms in functional groups at the B3LYP/6-31+G(d,p) level of theory. The calculated results were presented in Tables 1.10 and 1.11.

The negative charge densities are located mainly at the O/N atoms in the functional groups, *ca.* -0.507 to -0.936 e. They thus easily interact with the positively charged regions of the H-slab, particularly at H atoms, to form O/N \cdots H_{surf} electrostatic interactions. Similarly, the positive charges are in the range of 0.152-0.538 e focused mainly at H atoms in the functional groups, thus, they also conveniently form H \cdots O_{surf} electrostatic interactions upon complexation. For the C₆H₅SO₃H molecule, the O atoms in the -SO₃H group have highly negative charge densities leading to form stronger O \cdots H interactions with the H-slab in comparison to other derivatives. Results imply that the ability to form O \cdots H interactions in complexes decreases in the ordering of -SO₃H > -COOH > -OH > -CHO derivatives.

In addition, the proton affinity at the O atom and the ability of deprotonation of O-H/C-H bonds in functional groups are observed to clarify the formation ability of intermolecular contacts. As presented in Table 1.11, the PA values at O atoms range from 178.8 to 203.2 kcal.mol⁻¹ and increase in the sequence of -OH < -SO₃H < -COOH < -CHO, leading to the formation ability of O \cdots H_{surf} intermolecular contacts increases with the same order. On the other hand, DPE values in O-H/C-H bonds vary from 341.1 to 404.3 kcal.mol⁻¹ and follow to the ordering: -SO₃H < -COOH < -OH < -CHO < -CHO, indicating the strength of O/C-H \cdots O_{surf} interactions reduces as follows: -SO₃H > -COOH > -OH > -CHO. Besides, the negative charge density and PA at N atom in C₆H₅NH₂ are higher than those at O atoms in other derivatives, however, the ability of deprotonation for N-H bond is less preferred than O-H bonds due to the higher DPE(N-H) in comparison to DPE(O-H). Therefore, the formation of H \cdots O_{surf} contacts for the -NH₂ group is slightly weaker than that for -SO₃H, -COOH, and -OH ones. Further, DPE values of C-H bonds at the benzene ring are *ca.* 391.0 - 416.7 kcal.mol⁻¹ higher than that for O-H, N-H bonds in functional groups. Hence, the H \cdots C/ π intermolecular contacts at the benzene ring can be less stable interactions as compared to O/N \cdots H_{surf} ones.

1.3.3.2. AIM analysis

The topological geometries of the complexes are displayed in Figure 1.12. The

particular parameters for AIM analysis such as electron density ($\rho(r)$), Laplacian of electron density ($\nabla^2\rho(r)$), total electron density energy ($H(r)$) at the bond critical points (BCPs) are given in Table 1.16.

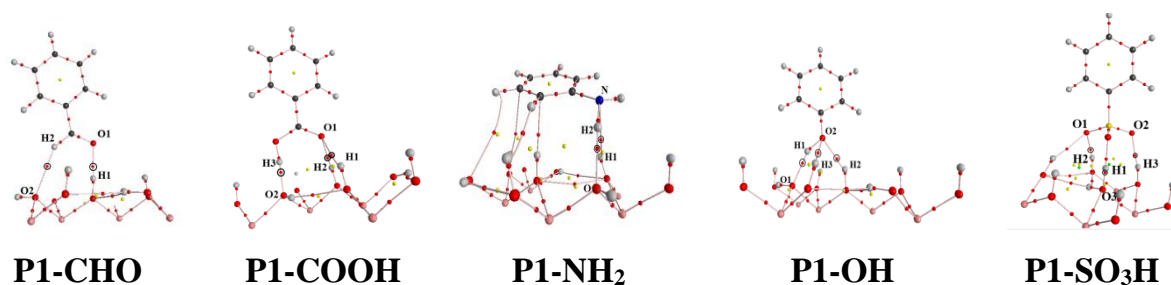


Figure 1.12. Topological geometry of the most stable complexes for adsorption of organic molecules on H-slab

Table 1.16. Characteristics of topological geometries ($\rho(r)$, $\nabla^2\rho(r)$, $H(r)$, in au) and EDT (in e) at the B3LYP/6-31+G(d,p) level

Complex	BCPs	$\rho(r)$	$\nabla^2\rho(r)$	$H(r)$	EDT
P1-CHO	O1...H1	0.038	0.107	0.000	0.02
	H2...O2	0.008	0.026	0.001	
P1-COOH	H3...O2	0.056	0.144	-0.005	-0.28
	O1...H1	0.041	0.124	0.000	
	O1...H2	0.007	0.028	0.001	
P1-NH₂	N...H1	0.006	0.018	0.001	0.00
	H2...O	0.028	0.080	-0.001	
P1-OH	O2...H2	0.030	0.087	-0.001	0.00
	O2...H3	0.008	0.029	0.001	
	H1...O1	0.040	0.115	-0.001	
P1-SO₃H	H1...O3	0.264	-1.252	-0.388	-0.76
	O...H1	0.080	0.128	-0.032	
	O1...H2	0.034	0.097	0.000	
	O2...H3	0.025	0.070	0.000	

The presence of BCPs in Figure 1.12 and the values of electron density $\rho(r)$, Laplacian ($\nabla^2\rho(r)$) in Table 1.16, that are primarily within the range of values for

noncovalent interactions [9], [49], [50], indicate that the O/N/C-H \cdots O hydrogen bonds exist in investigated complexes. Especially for **P1-SO₃H**, the values of $\rho(r)$ and $\nabla^2\rho(r)$ at O_{surf} \cdots H BCP are much higher than that at other BCPs and out of the range for noncovalent interactions. Additionally, the $\nabla^2\rho(r)$ and H(r) at this O_{surf} \cdots H BCP are largely negative, *ca.* -1.252 au and -0.388 au, respectively. Therefore, this contact is regarded as a covalent bond. This result suggests the trend of shifting the H atom in the -SO₃H to the H-slab to form the O_{surf}-H covalent bond in **P1-SO₃H**. Moreover, the large values of $\rho(r)$ and $\nabla^2\rho(r)$ at O_{surf}-H \cdots O BCP *ca.* 0.080 au and 0.128 au, respectively, reveal the high stability of O_{surf}-H \cdots O hydrogen bond. The H(r) at O_{surf}-H \cdots O BCP is negative (*ca.* -0.032 au) and constitutes a leading contribution of the covalent part to its strength.

In addition, as presented in Table 1.16, the $\rho(r)$ values at O/N/C-H \cdots O BCPs in complexes range from 0.006 to 0.264 au and decrease in the sequence of derivatives: -SO₃H > -COOH > -OH > -CHO > -NH₂. It can be suggested that the strength of the interactions and thus lead to stability of configurations tend to reduce in the same order. Furthermore, the H(r) values at BCPs in complexes (excepted for **P1-SO₃H**) are small negative, *ca.* -0.005 au, indicating these hydrogen bonds have a small part of covalent nature. With other BCPs of H \cdots O/N intermolecular contacts, the H(r) values are slightly positive (0.001 au), so these contacts have only non-covalent.

1.3.3.3. NBO analysis

The existence of hydrogen bonds in complexes and their strengths can be further observed by analyzing the total electron density (EDT) transfers following complexation, as shown in Figure 1.13 and Table 1.16. The overlap of electron density between the atoms involved in interactions implies the existence of O/N/C-H \cdots O hydrogen bonds in the investigated complexes (see Fig. 1.13). The EDT values are obtained with different signs based on the electron density transfers upon complex formation. For **P1-COOH** and **P1-SO₃H**, EDT values are negative due to the electron transfer from the surface to the molecules is stronger than the opposite transfer, from

molecule to surface. In contrast, for **P1-CHO**, **P1-OH**, **P1-NH₂**, EDT values are small positive. This results from the stronger electron density transfer from the molecule to the surface in comparison to the reversed transfer from the surface to the molecule. It is noted that the electron density transfers from the surface to the molecule in **P1-COOH** and **P1-SO₃H** are quite strong. Further, it implies the remarkable shifting of H atom in the -COOH, -SO₃H groups to the H-slab surface to form O_{surf}-H bond and O_{surf}-H...O hydrogen bonds upon complex formation.

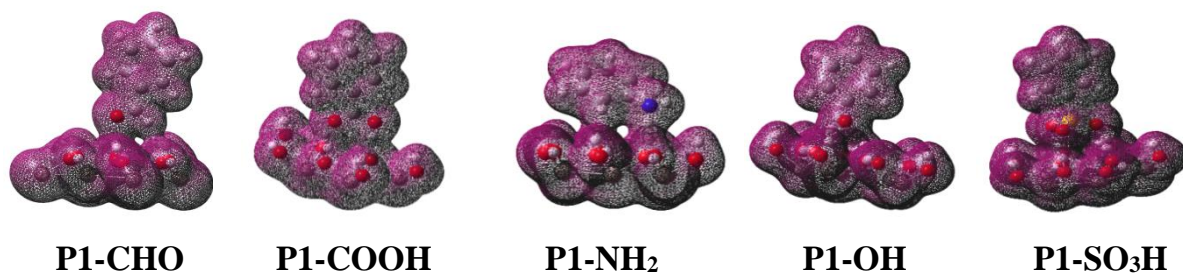


Figure 1.13. Schematic of total electron density of complexes at the B3LYP/6-31+G(d,p) level

1.3.4. Summary

By performing a theoretical investigation on adsorption of benzene's derivatives on the H-slab surface of kaolinite, we obtained eleven stable complexes corresponding to two special structures: i) vertical arrangement with forming interactions between functional groups and surface (**P1** type) and ii) parallel arrangement with the existence of interactions at benzene ring (**P2** type). The adsorption energy of complexes ranges from -3.0 to -24.8 kcal.mol⁻¹ in which the values are more negative for **P1** than for **P2**. Remarkable, highly stable intermolecular contacts are found in complexes of -SO₃H derivative. The stability of the complexes is mainly contributed by O/N-H...O and H...C/π hydrogen bonds. All results indicate that the adsorption ability of molecules on the H-slab of kaolinite decreases in the order of -SO₃H > -COOH > -OH > -CHO > -NH₂. Further, the interaction between these molecules and the H-slab surface forms favorably the complexes of **P1** type as compared to **P2**.

1.4. Adsorption of benzene derivatives on K⁺-supported kaolinite (001) surface

1.4.1. Stable complexes

To examine further the role of cation supported on a kaolinite surface, we continue to perform calculations for the interaction between some derivatives of benzene and K⁺-supported kaolinite (001) surface (denoted by K⁺-slab). The optimized adsorption configurations of C₆H₅-X (X = -CHO, -COOH, -NH₂, -OH) on K⁺-slab are displayed in Figure 1.14. Similar to the H-slab of kaolinite, the stable structures of benzene's derivatives adsorbed onto K⁺-slab are formed with two trends: i) interactions are mainly formed between functional groups and surface (**P1** type) and ii) interactions are focused at the benzene ring (**P2** type).

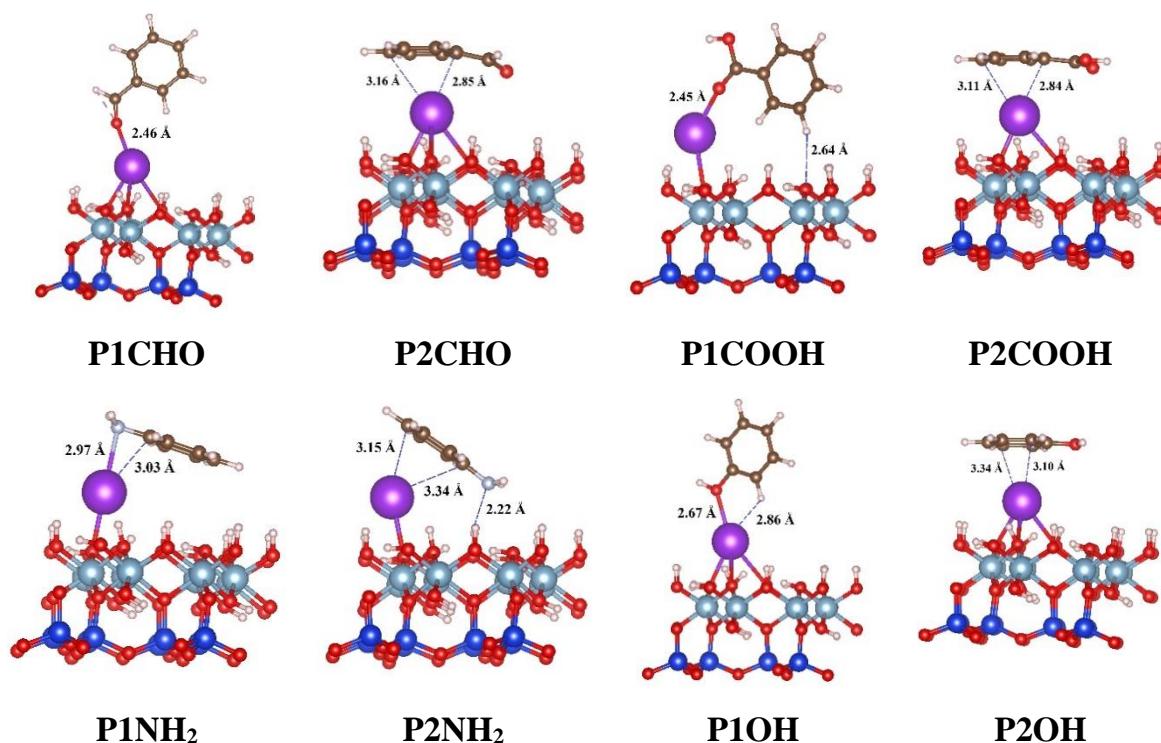


Figure 1.14. The stable complexes of molecules adsorption on K⁺-slab

The distances are in the range of 2.45-2.97 Å and 2.84-3.34 Å corresponding to K⁺⋯O/N and K⁺⋯π. In **P1COOH** and **P2NH₂**, the H⁺⋯O/N distances range from 2.22 Å to 2.64 Å. All these values are smaller than the total of van der Waals radii of atoms involving in interactions. In particular, the van der Waals radii of O, N, C, H, K atoms are 1.52 Å, 1.55 Å, 1.70 Å, 1.20 Å, and 2.75 Å, respectively [11]. Therefore,

it can be suggested that these contacts are formed in configurations upon adsorption and thus contribute to the stability of configurations.

In addition, MEP maps and NBO charges evaluate the formation ability of electrostatic interactions between sites at the surface and molecules in complexes (cf. Fig. 1.6 and Table 1.10). Accordingly, the $K\cdots O/N$ and $K\cdots\pi$ electrostatic interactions are formed favorably and thereby play an important role in the strength of **P1** and **P2** configurations, respectively. The $H\cdots O$ hydrogen bonds in **P1COOH** and **P2NH₂** are also regarded as an additional term in stabilization. Moreover, the small movement of the K^+ site on the surface is found following the adsorption of derivatives, especially for C_6H_5COOH and $C_6H_5NH_2$.

1.4.2. Adsorption energy

The adsorption energy values of configurations calculated by using the PBE and optPBE-vdW functionals are presented in Table 1.17.

Table 1.17. The adsorption energy of the stable complexes (in kcal.mol⁻¹)

	PBE	optPBE-vdW
P1CHO	-20.6	-21.7
P2CHO	-18.6	-22.7
P1COOH	-17.4	-22.8
P2COOH	-12.2	-17.4
P1NH₂	-7.6	-16.1
P2NH₂	-10.2	-19.1
P1OH	-4.8	-8.7
P2OH	-5.8	-11.2

The formation energy (E_f) of K^+ -slab is -6.2 kcal.mol⁻¹ (at PBE functional) which is computed by the expression: $E_f = E_{K^+-slab} - E_{H-slab} - E_{K^+}$. Here, the E_{K^+-slab} , E_{H-slab} , and E_{K^+} are energies of optimal structures of K^+ -slab, H-slab, and K^+ ion, respectively. Consequently, the K^+ -slab is slightly stable, and K^+ ion can be favorably

shifted to other sites upon adsorption of molecules. This is expressed in forming of stable configurations as displayed in geometrical structures.

The adsorption energy of configurations is in the range of -4.8 to -20.6 kcal.mol⁻¹ and -8.7 to -22.8 kcal.mol⁻¹ for PBE and optPBE-vdW functional, respectively. It can be indicated that the inclusion of vdW forces in calculations leads to improvement of adsorption energy values, *ca.* 1.1-8.9 kcal.mol⁻¹. The difference of E_{ads} values from PBE and optPBE-vdW calculations is consistent with previous report [20]. Noticeably, that the E_{ads} increases in the ordering of $-\text{CHO} \leq -\text{COOH} < -\text{NH}_2 < -\text{OH}$ derivatives for both functionals PBE and optPBE-vdW. As a consequence, the stability of configurations as well as adsorption ability of -CHO, -COOH derivatives on K⁺-slab is higher than that for -NH₂, -OH ones.

Furthermore, the energy values for **P1** type are more negative than that for **P2** in -COOH systems, indicating the important role of K \cdots O electrostatic interactions to the stability of complexes, consistent with results of H-slab systems (without cation K⁺). For -NH₂ and -OH derivatives, the **P2** configurations have more negative energy than the **P1** ones leading to the considerable contribution of K \cdots π intermolecular interactions (in **P2**) in stabilization, as compared to K \cdots O/N contacts (in **P1**). For -CHO derivative, the **P1** configuration is more stable than **P2** by using PBE calculation, whereas using vdW calculation, the **P2** is more slightly stable than **P1**. Therefore, the K \cdots O/N/ π contacts and vdW forces play an important role in the stability of the configurations in these investigated systems.

1.4.3. AIM and NBO analyses

To have a closer look at the formation and strength of intermolecular contacts in complexes, we carry out AIM and NBO calculations at the B3LYP/6-31+G(d,p) level. The results are illustrated in Figures 1.15, 1.16 and given in Table 1.18.

The appearance of bond critical points (blue rings, BCPs) in topological geometries (Fig. 1.15) indicates the existence of intermolecular contacts of K \cdots O/N/C and H \cdots O/N. The electron density ($\rho(r)$) and Laplacian ($\nabla^2\rho(r)$) values are in the range of 0.001-0.028 au and 0.002-0.150 au, respectively. These values are within

the range of values for noncovalent interactions [9], [49], [50]. With the small electron density, these contacts are evaluated as weak interactions.

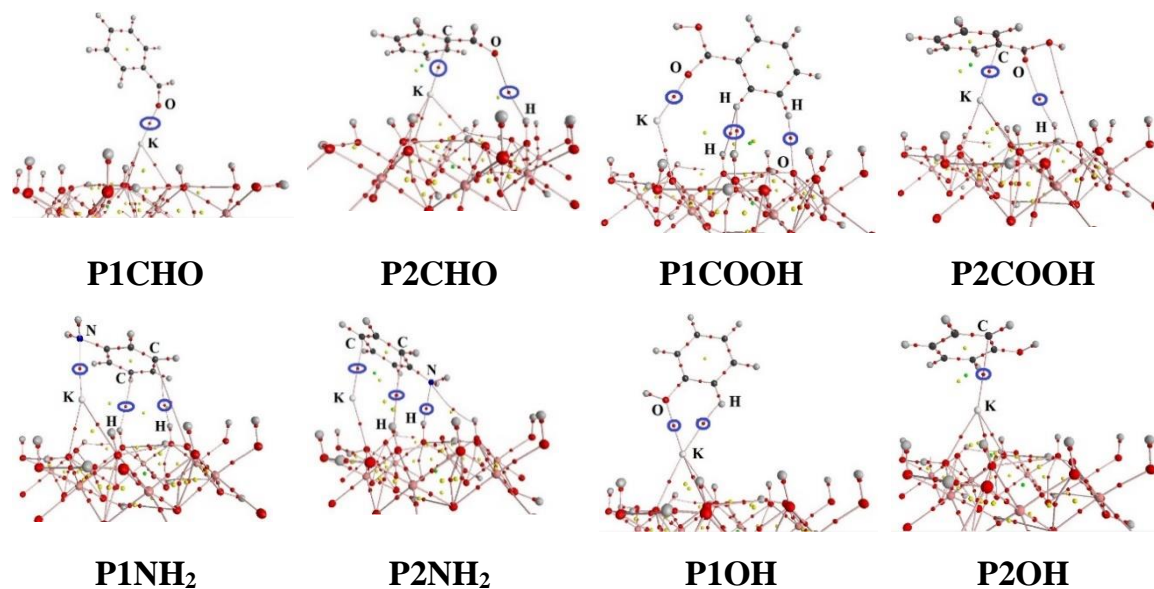


Figure 1.15. The topological geometries of the stable complexes for K^+ -slab systems

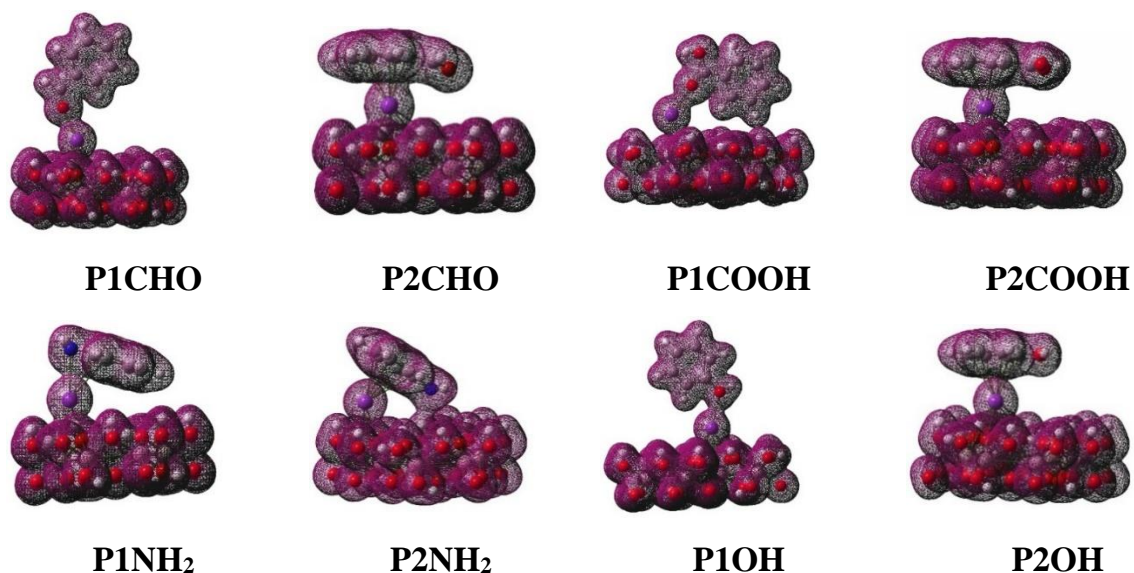


Figure 1.16. The EDT maps of the stable complexes for K^+ -slab systems

Further, the $\rho(r)$ values at $K \cdots O$ BCPs decrease in the sequence of $-\text{CHO} > -\text{COOH} > -\text{OH}$ derivatives. Similarly, the $\rho(r)$ values at $K \cdots C/\pi$ BCPs reduce in the ordering of $-\text{CHO} > -\text{COOH} > -\text{OH} > -\text{NH}_2$. Hence, the stability of complexes is mainly contributed by $K \cdots O/N/C$ interactions and tends to decrease in the order of -

CHO > -COOH > -OH > -NH₂ derivatives. Besides, H...C/N/O contacts are regarded as additional terms in stabilization.

Table 1.18. The characteristics for topology analysis and total of electron density transfer (EDT) for K⁺-slab systems at the B3LYP/6-31+G(d,p) level

Configurations	BCPs	$\rho(r)$	$\nabla^2(\rho(r))$	EDT
P1CHO	K...O	0.028	0.150	0.01
P2CHO	K...C	0.018	0.072	0.02
	O...H	0.001	0.002	
P1COOH	K...O	0.027	0.150	0.00
	O...H	0.007	0.023	
	H...H	0.002	0.006	
P2COOH	K...C	0.017	0.069	0.02
	K...N	0.013	0.048	
P1NH₂	H...C	0.002	0.005	0.02
	H...C	0.003	0.010	
	O...C	0.001	0.002	
P2NH₂	K...C	0.010	0.035	0.03
	H...C	0.001	0.002	
	N...H	0.017	0.042	
	N...H	0.003	0.010	
P1OH	K...O	0.019	0.082	0.01
	K...H	0.005	0.021	
P2OH	K...C	0.011	0.039	0.02

Furthermore, the electron density transfers (EDT) in configurations are also examined to clarify the formation of intermolecular interactions. The electron density overlaps between atoms involved in interactions imply the formation of these intermolecular contacts, as shown in Fig. 1.16. Besides, the EDT values in configurations are small positive. This is understood by the stronger electron density

transfers from molecules to surface as compared to the reverse transfers from surface to molecules.

1.4.4. Summary

By using DFT calculations, we evaluated the adsorption of benzene derivatives on a K^+ -slab. Two trends are found following the adsorption processes: i) interactions locate at functional groups (**P1** type) and ii) interactions focus at benzene ring (**P2** type). Results indicate that the processes of adsorbing these organic molecules on kaolinite are weak chemical adsorption and reduce in the order of $-COOH \approx -CHO > -NH_2 > OH$. Stability of complexes is contributed by $K \cdots O/N/\pi$ electrostatic interactions between K^+ site on surface and high negative charge regions of molecules. The inclusion of vdW forces leads to an improvement in adsorption energy and structural arrangement of molecules and K^+ -slab. Besides, the existence of K^+ cation on the kaolinite surface increases the adsorption ability of molecules.

Table 2.1. Some selected parameters for two stable complexes using PBE

Complex	functional	
	ER1	ER2
$d(\text{O}\cdots\text{Ti}_{5f})$	2.00	2.20/2.05
$d(\text{O}-\text{H}\cdots\text{O}_b)$	1.41 (O)	
$\angle \text{OHO}_b$	175.2 (O)	
$\angle \text{O}_b\text{TiO}_{1(2)}$	179.4 ¹	179.0 ¹ /178.8 ²
$\angle \text{CO}_{1(2)}\text{Ti}_{5f}$	151.1 ¹	173.3 ¹ /172.9 ²
$\Delta r(\text{C}=\text{O}_1)$		0.030
$\Delta r(\text{C}=\text{O}_2)$	-0.117	-0.161
$\Delta r(\text{O}-\text{H})$	0.435	
$\Delta r(\text{Ti}-\text{O}_a)$	0.300	0.177
$\Delta r(\text{Ti}-\text{O}_b)$	0.052	0.067

(^{1, 2, a, b} for O atoms in $>\text{C}=\text{O}$, $-\text{COOH}$ groups of the molecule, O sites in the plane, and at the bridge of surface, respectively; d and Δr are in Å, \angle in °)

As shown in the MEP of ER, the high negative charge regions are found at O atoms, whereas the high positive charge regions are located at H atoms. Accordingly, O and H atoms are favorable interacting sites when ER molecules are adsorbed on r-TiO₂. Figure 2.1 shows that the **ER1** is formed by adhesion of $-\text{COOH}$ group of ER on the surface, while the **ER2** is obtained by arranging ER molecules along rows containing Ti five-fold coordination (Ti_{5f}) sites due to the interaction between two $>\text{C}=\text{O}$ groups of ER and those of Ti_{5f} sites. The Ti \cdots O interactions are formed by Ti_{5f} sites of surface and O atoms in $>\text{C}=\text{O}$, $-\text{OH}$ groups of the adsorbed molecule. Besides, an O-H \cdots O hydrogen bond emerges between the bridging O (O_b) site of r-TiO₂ and H atom in the O-H bond of ER. The distances of intermolecular interactions presented in Table 2.1 are in the range of 2.00-2.20 Å and 1.41 Å for Ti_{5f} \cdots O and O-H \cdots O_b, respectively. All these values are significantly smaller than the total van der Waals radii of Ti and O (3.82 Å), O and H (2.72 Å) atoms involving in the interactions. It is noteworthy that the Ti_{5f} \cdots O distances in the investigated complexes are close to those

of the Ti-O bonds in the TiO₂ bulk (ranging from 1.86 Å to 2.20 Å). Therefore, the Ti_{5f}···O and O-H···O_b contacts are predicted to be strong interactions during the adsorption process.

In addition, the values of 178.8° to 179.4°, 151.1° to 173.3°, and 175.2° are observed for the O-Ti-O₁₍₂₎, C-O₁₍₂₎-Ti, and the O-H-O_b angles, respectively. Besides, the changes of bond length for C=O, O-H, and Ti-O in ER and r-TiO₂ are determined. The lengths of C=O bonds of the carbonyl group are elongated by *ca.* 0.03 Å whereas that of carboxyl groups are shortened with an amount within the range of 0.12-0.16 Å. The largest value of 0.43 Å is found for the O-H bond in ER upon interaction. Also, the Ti-O bonds of the surface are elongated in the range of 0.05 to 0.30 Å. This indicates that the bond lengths and angles at atoms involving in interactions change considerably due to complexation.

2.1.2. Energetic aspects of the adsorption process

To evaluate the adsorption ability of r-TiO₂ for ER and the stability of configurations, adsorption (E_{ads}), interaction (E_{int}), and deformation ($E_{\text{def-surf}}$, $E_{\text{def-mol}}$) energies are given in Table 2.2, which are calculated employing the PBE functional.

Table 2.2. Energies for adsorption of Enrofloxacin on rutile-TiO₂ (110) surface (in kcal.mol⁻¹)

Complex	E_{ads}	E_{int}	$E_{\text{def-surf}}$	$E_{\text{def-mol}}$
ER1	-26.4 (-40.0)	-55.6	19.3	9.9
ER2	-35.1 (-61.0)	-54.9	16.7	3.1

(italic values in parentheses are obtained at optPBE-vdW functional)

As presented in Table 2.2, the adsorption energies of ER on r-TiO₂ are highly negative and of -26.4 and -35.1 kcal.mol⁻¹ corresponding to **ER1** and **ER2**; therefore, **ER2** is more stable than **ER1**. Due to large negative adsorption energies and the form of strong interactions on the surface, the process of adhesion ER on r-TiO₂ is characterized as strong chemisorption. The stability of **ER2** illustrated in Figure 2.1 is mainly contributed by two Ti_{5f}···O interactions, whereas the **ER1** is stabilized by both Ti···O and O-H···O_b intermolecular interactions. The contribution of Ti_{5f}···O and

$\text{H}\cdots\text{O}_b$ interactions following adsorption of some organic molecules on r-TiO₂ has been found in the previous studies [84], [123], [147]. It is remarkable that the including of van der Waals forces in single-point energy calculations at optPBE-vdW functional leads to obtain the more negative values of adsorption energy, *ca.* 14 kcal.mol⁻¹ and 26 kcal.mol⁻¹ for **ER1** and **ER2** as compared to PBE calculations.

Further, a good understanding of interactions between adsorbed molecules and the material surfaces can provide better insights into the various aspects of the adhesion process of molecules on surfaces. The interaction energies of **ER1** and **ER2** are -55.6 and -54.9 kcal.mol⁻¹, respectively (*cf.* Table 2.2). Hence, the Ti_{5f}···O and O-H···O_b contacts formed in these complexes can be regarded as strong interactions. The highly negative values of E_{int} for **ER1** as compared to those of **ER2** counterpart implies a significant contribution of O-H···O_b hydrogen bond to the overall stability of the complexes.

The deformation energy is a characteristic parameter for evaluating the ability of separating the substrate and the surface from its stable adsorption configuration [20]. As tabulated in Table 2.2, these energy values for TiO₂ surface are larger than those for ER molecule. For this reason, the ability of separation and then to form stable structures are less convenient for r-TiO₂ than for ER. These obtained results are consistent with the remarkable changes of the structure of r-TiO₂ as compared to ER in the aforementioned stable configurations.

2.1.3. Characteristics of interactions on the surface

To get more insight into the origin and role of intermolecular interactions, the AIM and NBO analyses are carried out at the B3LYP/6-31+G(d,p) level of theory. Some characteristic parameters are given in Table 2.3 and presented in Figure 2.2.

The presence of Bond Critical Points (BCPs) topology in Figure 2.2 and their large electron density ($\rho(r)$). Laplacian of electron density values ($\nabla^2(\rho(r))$) in Table 2.3 proves the existence of stable intermolecular interactions between O···Ti, H···O as shown in Figure 2.1. The $\rho(r)$ value of O-H···O_b BCP is 0.093 au and slightly larger than that of Ti_{5f}···O BCP in **ER1**. As a result, the O-H···O_b hydrogen bond is highly

stable and plays an important role in the stability of **ER1** as compared to $\text{Ti}_{5f}\cdots\text{O}$ interaction. Remarkably, the $\rho(r)$ values of $\text{O}-\text{H}\cdots\text{O}_b$ and $\text{Ti}_{5f}\cdots\text{O}$ interactions in **ER1** are larger than those of $\text{Ti}_{5f}\cdots\text{O}$ interactions in **ER2**. This result leads to the strength of interactions formed in **ER1** being more significant than that in **ER2**. As a consequence, the interaction energy for **ER1** is larger than that for **ER2** and in good agreement with the values shown in Table 2.2. The existence of $\text{O}\cdots\text{O}$ chalcogen-chalcogen interaction in **ER1** with an electron density of 0.011 au indicates a slight contribution to the stability of **ER1**.

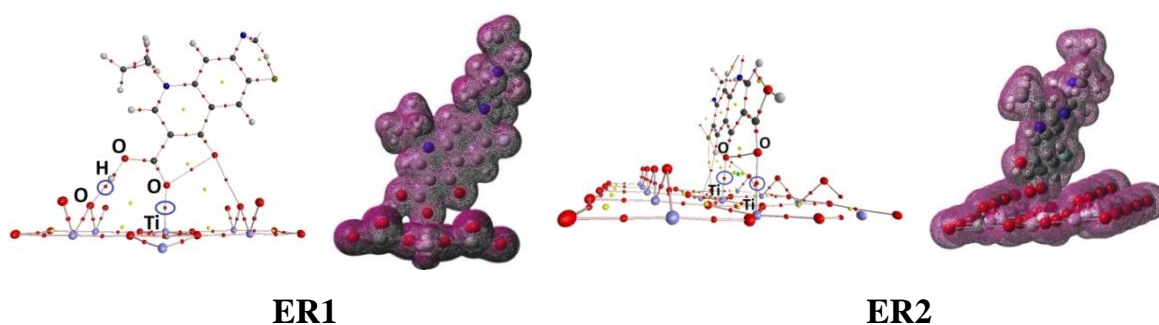


Figure 2.2. The topology and electron density transfer maps for the first-layered structures of **ER1** and **ER2** at the B3LYP/6-31+G(d, p) level

Table 2.3. The topological analysis and EDT of investigated structures at the B3LYP/6-31+G(d, p) level

	BCPs	$\rho(r)$	$\nabla^2(\rho(r))$	H(r)	EDT
ER1	$\text{O}_1\cdots\text{Ti}$	0.080	0.452	-0.005	
	$\text{O}-\text{H}\cdots\text{O}$	0.093	0.112	-0.046	0.22
	$\text{O}\cdots\text{O}$	0.011	0.038	0.002	
ER2	$\text{O}_1\cdots\text{Ti}$	0.042	0.254	0.007	
	$\text{O}_2\cdots\text{Ti}$	0.068	0.404	0.001	0.36

^{1,2}- for O atoms in $>\text{C}=\text{O}$ and $-\text{COOH}$ groups

In addition, the $\nabla^2(\rho(r))$ values for $\text{Ti}_{5f}\cdots\text{O}$ BCPs are large and in the range of 0.254 to 0.452 au, therefore, they are regarded as highly stable interactions. The $\nabla^2(\rho(r))$ values for $\text{O}-\text{H}\cdots\text{O}_b$ and $\text{O}\cdots\text{O}$ interactions are 0.038 and 0.112 au, respectively, falling within the range for weak interactions [9], [49]. It should be

noted that the negative values of $H(r)$ for $O-H\cdots O_b$ and $Ti_{5f}\cdots O$ BCPs in **P1** (*cf.* Table 2.3) imply that these interactions are stabilized by the covalent component. In contrast, the $H(r)$ values for $O\cdots O$ (**ER1**) and $Ti_{5f}\cdots O$ (**ER2**) BCPs are all positive, suggesting that they are non-covalent interactions.

Moreover, the total electron density map shown in Figure 2.2 and the values given in Table 2.3 corroborate the formation of the aforementioned interactions. This can be understood due to the high electron density overlaps between H and O_b , O and Ti_{5f} atoms directly involved in the $O_b\cdots H$ hydrogen bond and $Ti_{5f}\cdots O$ interaction, respectively. The larger overlap in **ER2** leads to its stronger stability as compared to **ER1** and in good agreement with adsorption energies in Table 2.2. Hence, the $Ti\cdots O$ and $O-H\cdots O$ intermolecular contacts are regarded as strong interactions.

2.1.4. Summary

Two stable configurations formed by the interaction between ER and r-TiO₂ were optimized by using the VASP program and employing the DFT method. The adsorption of ER molecule onto the r-TiO₂ is a strong chemical adsorption with energies of -26 and -35 kcal.mol⁻¹ (PBE) and of -40 and -61 kcal.mol⁻¹ (optPBE-vdW) for **ER1** and **ER2** complexes, respectively. The stability of the complexes formed significantly depends on the strong $O\cdots Ti_{5f}$ electrostatic interactions. The $O-H\cdots O_b$ hydrogen bond found in **ER1** plays an important role in stabilizing this adsorbate-adsorbent system. The adsorption of ER on r-TiO₂ preferably forms $>C=O\cdots Ti_{5f}$ interactions. Also, the $O\cdots O$ chalcogen interaction examined in **ER1** slightly contributes to the complex's strength.

2.2. Adsorption of ampicillin, amoxicillin, and tetracycline molecules on rutile-TiO₂ (110) surface

2.2.1. Stable complexes

Structures of ampicillin (AP), amoxicillin (AX), tetracycline (TC) molecules, and r-TiO₂ are considered based on experimental reports and then optimized using the PBE functional as shown in Figure S1 in Appendix. Some parameters for the optimized geometries in comparison with references are given in Table S1

(Appendix). Differences in bond lengths and angles are small, in the range of 0.01-0.06 Å and 1°-3° as compared to experimental data, respectively. The adsorption configurations of AP, AX, and TC molecules on r-TiO₂ are further optimized using DFT computations. The stable complexes corresponding to ampicillin, amoxicillin, tetracycline systems assigned symbols **AP1**; **AP2**, **AX1**; **AX2**; **AX3**, and **TC1**; **TC2**; **TC3** are shown in Figure 2.3 by leaving out two layers at the bottom. Some selected parameters following the complexation are given in Table 2.4.

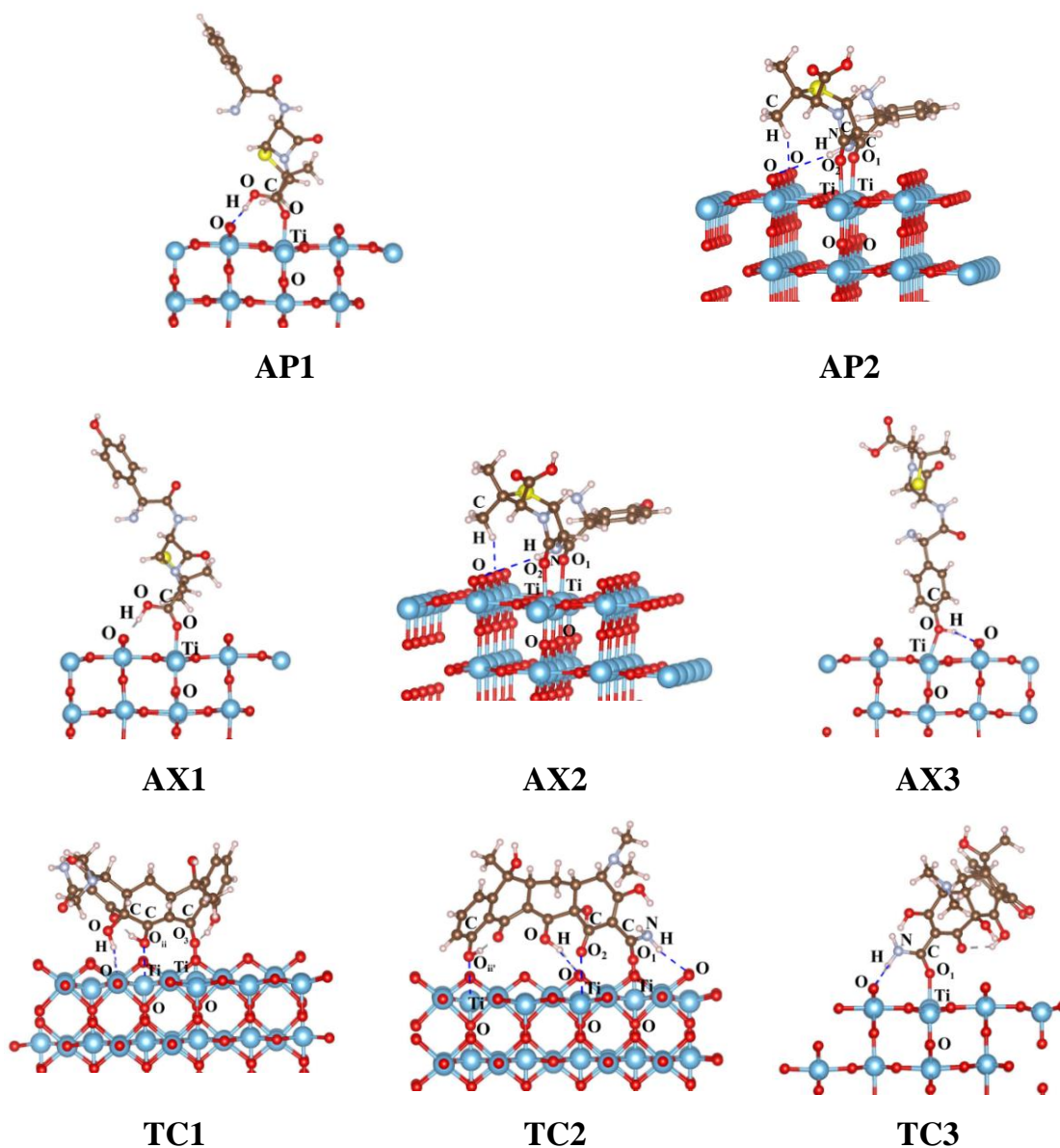


Figure 2.3. Stable complexes for adsorption of antibiotic molecules on rutile-TiO₂ (110) surface

Table 2.4. Some selected parameters for stable adsorption configurations

Parameter	AP1	AP2	AX1	AX2	AX3	TC1	TC2	TC3
d(O···Ti)	2.11	2.23 ¹⁾ /2.21 ²⁾	2.08	2.23 ¹⁾ /2.20 ²⁾	2.26	2.40 ¹⁾ /2.17 ²⁾	2.15 ¹⁾ /2.70 ²⁾ / 2.42 ³⁾	2.06
d(X-H···O)	1.48 ^{a)} 2.48/2.65 ^{c)}	2.51/2.62 ^{b)} 2.53/2.69 ^{c)}	1.52	2.52/2.60 ^{b)} 2.53/2.71 ^{c)}	1.71	1.96/2.11 ^{a)}	2.05/2.69 ^{a)} 2.40/2.53 ^{b)} 2.51 ^{c)}	1.63 ^{b)}
α (X-H···O)	171.9 ^{a)} 155.8/142.6 ^{c)}	120.2/173.5 ^{b)} 126.2/137.6 ^{c)}	176.3	119.8/173.6 ^{b)} 127.8/138.2 ^{c)}	161.7	166.8/123.2 ^{a)} 148.7/137.8 ^{c)}	144.8/162.6 ^{a)} 103.1/159.8 ^{b)} 164.0 ^{c)}	171.8 ^{b)}
α (C-O···Ti)	146.8	146.8/134.4	150.4	146.5/134.4	150.5	133.8/151.8	146.1/162.7/ 138.1	153.6
Δr (C=O)	0.037	0.019/0.019	0.033	0.018/0.019	0.025	0.016/0.015	0.027/-0.009/ -0.004	0.013
Δr (X-H)	0.079	0.007 ^{b)} / -0.002 ^{c)}	0.072	0.007 ^{b)} / -0.002 ^{c)}	0.035	0.006 ^{b)} / -0.036 ^{c)}	-0.027 ^{a)} /0.004 ^{b)} / -0.004 ^{c)}	0.031 ^{b)}
Δr (Ti-O _b)	0.126	0.092/0.117	0.110	0.092/0.120	0.091	0.176/0.054	0.093/0.029/ 0.103	0.206

^{a), b), c)}- for X = O, N, C atoms involving in hydrogen bonds; ^{1,2,3)}- for O atoms in antibiotic molecules, d: distance in Å, α : angle in degree, Δr : change of bond length, in Å.

As displayed in Figure 2.3, the optimized structures of antibiotics adsorbed on r-TiO₂ are stabilized by the contributions of both Ti···O and O(C,N)-H···O contacts. The Ti···O interactions are formed at Ti sites of r-TiO₂ with O atoms in >C=O or O-H groups of the antibiotic molecules while the O(C,N)-H···O hydrogen bonds are formed between O atoms at bridging sites (O_b) of the surface and H atoms in O-H, C-H, N-H bonds of molecules. As a result, the stable configurations are obtained by either interaction between -COOH, -OH groups of molecules with the surface of TiO₂ (**AP1**, **AX1**, **AX3**) or between >C=O groups in an arrangement of molecules along with Ti five-fold coordination (Ti_{5f}) sites (**AP2**, **AX2**). For the tetracycline system, the stability of configurations receives contributions of several intermolecular interactions between >C=O, -OH, -NH₂ groups with Ti_{5f}, O_b sites of the surface (**TC1**, **TC2**, **TC3**).

In addition, the distances of intermolecular interactions presented in Table 3.4 are in the range of 2.06 to 2.70 Å, 1.48 to 2.69 Å, 2.48 to 2.71 Å, and 1.63 to 2.62 Å for Ti···O, O-H···O, C-H···O, and N-H···O contacts, respectively. All these values are smaller than the total van der Waals radii of Ti and O (3.82 Å), O and H (2.72 Å), C and H (2.90 Å), N and H (2.75 Å) atoms involved in the interactions [11], [97]. The O(C,N)-H···O_b contacts are thus estimated as hydrogen bonds and contribute to the complexes' stability. Besides, the Ti_{5f}···O distances in the investigated complexes are close to those of the Ti-O bonds in the TiO₂ bulk and surfaces (*ca.* 1.84-2.17 Å, ref. [17], [18], [125]). Therefore, the Ti_{5f}···O intermolecular contacts are predicted to be quite strong interactions upon the adsorption process.

Furthermore, the changes of C=O, O-H, C-H, N-H, Ti-O bond lengths, and the C-O-Ti, O(C,N)-H-O bonding angles upon interactions with the surface are also calculated and shown in Table 2.4. The value ranges from 134° to 163°, 126° to 164°, 103° to 174°, and 123° to 176° are noted for C-O-Ti, C-H-O_{surf}, N-H-O_{surf}, and O-H-O_{surf} angles, respectively. Also, the changes of bond length for C=O, O-H, and Ti-O in antibiotics and surface are given in Table 2.4. The lengths of C=O bonds of carbonyl or carboxyl groups are elongated by *ca.* 0.013 to 0.047 Å (except in **TC2** where the bond length is shortened by *ca.* 0.009 Å). The bond lengths of O(C,N)-H bonds involved in hydrogen bonds are elongated in the range of 0.004-0.079 Å. Following the formation of O-H···O (in **TC2**), N-H···O (in **TC1**), C-H···O (in **AP2**, **AX2**, **TC2**) hydrogen bonds, the O(N,C)-H bonds are shortened by 0.002-0.036 Å. Also, the Ti-O bonds of the surface are elongated in the range of 0.029 to 0.206 Å upon adsorption. In general, the bond lengths and angles at atoms involved in interactions are not uniformly changed upon complexation.

2.2.2. Energetic aspects of the adsorption process

To evaluate the adsorption ability of antibiotic molecules on r-TiO₂, and also the strength of intermolecular interactions, we calculate some characteristic parameters including the adsorption energy (E_{ads}), interaction energy (E_{int}), and deformation energies ($E_{\text{def-surf}}$; $E_{\text{def-mol}}$) for the systems considered (Table 2.5). The

opt-PBE-vdW functional is subsequently computed for improving the E_{ads} values for further consideration of the adsorption ability of antibiotic molecules.

Table 2.5. Energies for adsorption processes using both PBE and optPBE-vdW functionals (kcal.mol⁻¹) ^{a)}

	AP1	AP2	AX1	AX2	AX3	TC1	TC2	TC3
E_{ads}	-23.0	-25.3	-26.1	-26.6	-15.4	-19.1	-24.1	-21.7
	<i>-42.7</i>	<i>-64.9</i>	<i>-42.9</i>	<i>-66.5</i>	<i>-28.4</i>	<i>-58.9</i>	<i>-66.6</i>	<i>-45.1</i>
E_{int}	-37.5	-43.6	-37.6	-44.7	-22.1	-42.5	-50.0	-40.6
$E_{\text{def-surf}}$	7.4	11.5	5.9	11.7	4.4	13.5	13.0	12.1
$E_{\text{def-mol}}$	7.1	6.9	5.5	6.5	2.2	9.9	12.9	6.8

^{a)} *Italic values of E_{ads} are obtained using the optPBE-vdW functional.*

As presented in Table 2.5, the adsorption energies of these molecules on r-TiO₂ are highly negative and in the range of -15 to -27 kcal.mol⁻¹ and -28 to -67 kcal.mol⁻¹ for the PBE and optPBE-vdW functionals, respectively. The adsorption energies E_{ads} are slightly different ca. 1-2 kcal/mol⁻¹ for the AP, AX, and TC systems. The adsorption ability of these molecules on the r-TiO₂ is thus quite strong and similar to each other. Furthermore, the adsorption of AP, AX, and TC molecules on r-TiO₂ can be characterized as chemisorptions, and they are evaluated as weaker processes, in comparison to those for vermiculite, by *ca.* 12 kcal.mol⁻¹. This can be explained by the strong electrostatic interactions of Mg²⁺ sites of a vermiculite surface and O atoms in >C=O groups of molecules as compared to Ti...O contacts in the aforementioned configurations. It is noteworthy that the E_{ads} values for optPBE-vdW are more negative than that for PBE functional, similarly with results for ER system above. Here, the inclusion of vdW interactions in the geometry optimization tends to affect the total electronic energy of complexes, resulting in more negative adsorption energy values for the optPBE-vdW functional in comparison to the values obtained by the PBE functional [123]. Besides, the differences of E_{ads} values when using the PBE functional are small, ~1 kcal/mol⁻¹ for AP, AX systems, and of 2 kcal/mol⁻¹ for TC one. These differences are larger for optPBE-vdW computations: a range of 22-

24 kcal/mol⁻¹ is obtained for AP, AX, while a difference of 8-21 kcal.mol⁻¹ is derived for TC. The **AP2**, **AX2**, **TC2** are the most stable complexes for the investigated systems. As a consequence, the contribution of two Ti···O contacts to the stabilization is more significant than that of one Ti···O with H···O contact as displayed in Figure 2.3. The important addition of O/N-H···O hydrogen bonds along with Ti···O interactions in these adsorbate-adsorbent systems is consistent with previous reports on interactions between organic molecules and rutile surfaces [80], [81], [84], [119], [122], [123], [124]. Hence, in the formation of stable configurations, the role of >C=O···Ti contacts can be regarded as more substantial than that of O/N/C-H···O hydrogen bonds.

On the other hand, the interaction energies E_{int} of investigated configurations are largely negative and amount in a range of -22 to -50 kcal.mol⁻¹ and increase in going from TC to AX and finally to AP, as given in Table 2.5. Consequently, the strength of interactions slightly decreases in the order of TC > AX \approx AP. The larger negative values of E_{int} for **AP2**, **AX2**, and **TC2**, as compared to the **AP1**, **AX1**, **AX3**, **TC1**, and **TC3** counterparts, imply the significant contributions of the Ti_{5f}···O electrostatic attractions and O/N/C-H···O hydrogen bonds to the stability of these complexes. This result is similar to the ordering of adsorption energy changes obtained by the optPBE-vdW functional mentioned above.

The deformation energy is one of the important parameters for evaluating the ability to separate the adsorbed molecules and the adsorbent from its stable configuration as shown in sections above. Calculated results indicate that $E_{\text{def-surf}}$ values for r-TiO₂ are inherently larger than those for AP, AX, and TC molecules. It can be suggested that the ability of separation and then the formation of stable structures are less convenient for the surface than for the molecules considered. This is consistent with the considerable changes in structure observed for the surface as compared to the molecules in the aforementioned stable configurations. These results are similar to previous investigations on the adsorption of molecules onto solid surfaces [143]. Furthermore, the separation of antibiotic molecules from stable

configurations is reduced in the following order: $AX \approx AP > TC$. The formation of stable interactions between functional groups and the surface for the TC system leads to significant changes in the structure of TC as compared to its optimized geometry. Furthermore, the interaction in configurations of TC is stronger than that for AP, AX systems as expressed by the higher interaction energy (cf. Table 2.5). As a consequence, the separation of TC in the stable configuration is more inconvenient than for AP and AX. On the other hand, the similar separation of stable configurations found in AP and AX systems is consistent with the small differences in structures for AP, AX molecules, and their configurations (cf. Fig. 2.3).

2.2.3. Characteristic properties of intermolecular interactions

2.2.3.1. Ability to form stable interactions on TiO_2 surface at different sites of molecules

To have a better understanding of the nature of the interactions in the configurations as well as to estimate the formation ability and stability of the interactions, NBO charge distributions and MEP maps of the antibiotic molecules, the vertical proton affinity (PA), and de-protonation enthalpy (DPE, without geometry re-optimization) were considered and illustrated in Figures S2 and S3 and gathered in Table S2 (Appendix).

The MEP maps of the molecules (shown in Figure S3) are displayed by different colors representing the electrostatic potential values, increasing from red to orange, yellow, green, and finally to blue colors. The most negative charge density (red color) is located considerably at the O sites of C=O, C-O groups, and N sites (in C-N, N-H bonds). Conversely, the most positive charge density (blue color), centered on H atoms, is higher on the O-H than on the N-H and C-H bonds. These evaluations are further characterized by NBO charge distributions collected in Figure S2 (SI). In particular, the charge density values at O/N and H atoms are in the range of -0.5 to -0.9 electron and 0.2 to 0.5 electron, respectively. As a matter of fact, the electrostatic interactions are formed favorably between O/N atoms and Ti_{5f} sites (Ti^{4+}); H atoms, and O_b sites (O^{2-}).

In addition, the PA(O) values given in Table S2 (Appendix) indicate that the gas-phase basicity of the O atoms of the $>C=O$, $-COOH$ groups is quite strong due to their large proton affinities ranging from 183 to 235 kcal.mol⁻¹. This implies that an attractive interaction of the O atoms of these groups with Ti_{5f} sites on the surface is significant, leading to the formation of O··Ti stable contacts in the resulting configurations. For the hydrogen bond formation on the rutile surface, stronger intermolecular contacts are obtained with the participation of O-H covalent bonds as compared to N-H, and also C-H bonds. This can be understood from the fact that the O-H bonds are more polarized than the N-H bonds, and much more than C-H bonds which is due to the smaller DPE value for the former in comparison with the latter, corresponding to the values in the range of 333-359 kcal.mol⁻¹ (for O-H bonds) and in the range of 344-356 kcal.mol⁻¹ (for N-H) and 362-392 kcal.mol⁻¹ (for C-H). Hence, the stability of hydrogen bonds formed on r-TiO₂ tends to decrease from O-H··O to N-H··O and finally to C-H··O in the investigated systems.

On the other hand, the ability of forming orbital interactions is considered by looking at the valence band (VB) and conduction band (CB) as related to the Fermi level (E_F) of r-TiO₂ and the frontier molecular orbitals of the adsorbed molecules as presented in Figure 2.4. The highest occupied molecular orbital (HOMO) and lowest unoccupied molecular orbital (LUMO) levels of the molecule interacting with the TiO₂ surface are known to play an important role in molecular adsorption [69]. As displayed in Figure 2.4, the HOMO and LUMO energies of the molecules (determined relatively to the VB of TiO₂) are close to the VB and CB regions of rutile-TiO₂ calculated at the same level of theory using PBE functional. The stable orbital interactions are more favorably formed between the HOMOs of an antibiotic molecule and the CB of TiO₂ as compared to other ones, similar to previous studies [69], [128]. Here, stable interactions between antibiotic molecules and r-TiO₂ are formed by electron transfers from HOMOs of molecules to the Lewis acid Ti sites of surface (Ti_{5f}) (cf. Figures 2.5 and S5 (Appendix)). Besides, the formation of these

interactions is expected to lead to a slight change in the band energy of TiO₂ solid by *ca.* 0.2 eV (cf. Fig. S5, Appendix).

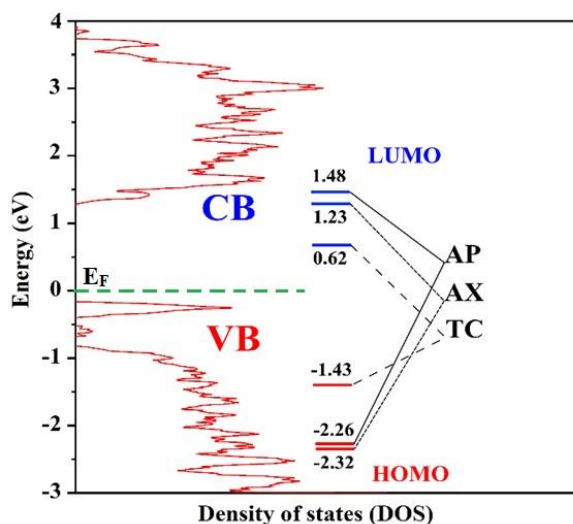


Figure 2.4. DOS plot of rutile-TiO₂ (110) surface and HOMO, LUMO levels of adsorbed antibiotic molecules

2.2.3.2. *The existence and role of interactions upon complexation*

To have a clearer view of the existence and role of adsorption interactions, the topological geometries of complexes are determined and illustrated in Figures 2.5 and S4 (Appendix). Some characteristic parameters are tabulated in Table S3 (Appendix). Additionally, the density of states (DOS), electron transfers, and electronic charge distribution for the most stable configurations are considered and displayed in Figures 2.5 and S5 (Appendix).

The formation of intermolecular contacts O/N...Ti, H...O in complexes is revealed by the presence of bond critical points (BCPs, marked by blue circles) in the topologies depicted in Figure 2.5(a). Additionally, as listed in Table S3 (Appendix), the electron density $\rho(r)$ values of Ti_{5f}...O, O/N-H...O_b, and C-H/C...O_b BCPs are in the range of 0.017 - 0.070 au, 0.018-0.078 au, and 0.005-0.013 au, respectively. The Ti...O interactions and O/N-H...O hydrogen bonds are thus highly stable and play an important role in the stability of complexes. The C-H...O hydrogen bonds and C...O weak interactions are regarded as cooperative terms to the stability of configurations because of their small $\rho(r)$ values. Besides, the Laplacian $\nabla^2(\rho(r))$ values for Ti_{5f}...O

BCPs range from 0.05 to 0.38 au indicating that these contacts are noncovalent interactions. Similarly, for O/N-H \cdots O hydrogen bonds, the $\nabla^2(\rho(r))$ values are in the range of 0.02-0.15 au, falling within the range for noncovalent interactions [9], [49]. Negative values of $H(r)$ are found out at BCPs of O/N-H \cdots O_b and Ti_{5f} \cdots O contacts in **AP1**, **AX1**, **AX3**, and **TC3** (cf. Table S3) indicating that these interactions have a certain part of covalent nature. In contrast, the $H(r)$ values for other contacts are all positive suggesting that they have a non-covalent nature.

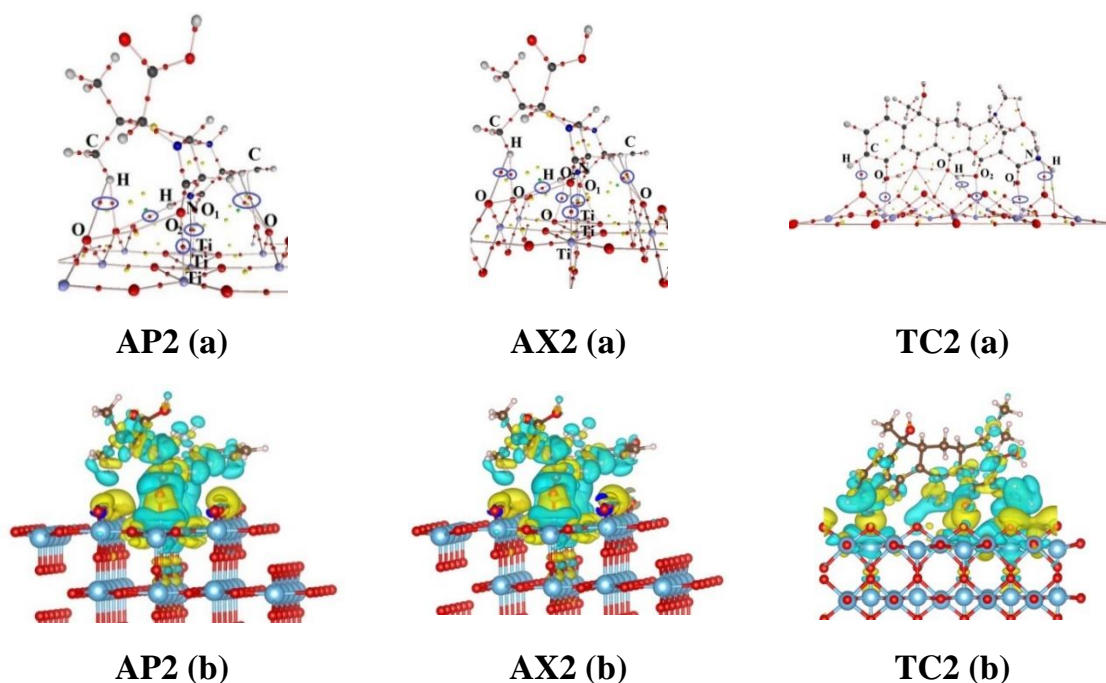


Figure 2.5. a) Topological critical points and b) electronic charge density transfer of the most stable complexes

The formation of intermolecular contacts is further considered as two-electron transfers upon complexation. The first transfer is from HOMOs of the molecule, particularly at the lone pair LP(O) and $\pi(\text{C}=\text{O})$ orbitals to Ti-3d orbitals in the CB region of r-TiO₂ (110) to form Ti \cdots O interactions. The second one is from the electron density at O-2p orbitals in the VB of the surface to LUMOs of the molecules including $\sigma^*(\text{O}/\text{N}/\text{C}-\text{H})$ orbitals to form O/N/C-H \cdots O hydrogen bonds. These overlaps of electron density would lead to the shifting of DOS to the CB regions in configurations as compared to TiO₂ (cf. Figure S5). Besides, the transfers are further demonstrated by the electron density transfer (EDT) and electronic charge

distributions shown in Figures 2.5(b) and S5 (Appendix). Furthermore, the charge density distributions in most stable configurations are displayed by yellow and cyan colors in Figure 2.5(b). Accordingly, the cyan color is assigned for regions of reduced charge density while the yellow color is assigned for regions of enhanced charge density in comparison to initial monomers. As a consequence, the charge density is mainly located at the $\text{Ti}\cdots\text{O}$ site whose electrostatic attractions lead to the formation of complexes.

2.2.4. Summary

Adsorption of the ampicillin (AP), amoxicillin (AX), and tetracycline (TC) antibiotics on the rutile- TiO_2 (110) surface (r- TiO_2) were investigated in detail using density functional theory calculations. The adsorption energies of the antibiotic-surface systems are calculated to be in the range of -15 to -27 kcal.mol^{-1} and -65 to -67 kcal.mol^{-1} as obtained from the PBE and optPBE-vdW functionals, respectively. Such a large difference indicates the importance of the inclusion of van der Waals interactions in the functional. These processes are regarded as strong chemical adsorptions. The ability of interactions between functional groups of antibiotics and r- TiO_2 is regarded approximately for AP, AX, and TC. The formation and nature of surface interactions were fully considered based on quantum chemical approaches. The adsorption configurations are stabilized by the significant contribution of $\text{O}\cdots\text{Ti}_{5f}$ electrostatic attractions and an additional role of the $\text{O/N-H}\cdots\text{O}_b$ hydrogen bonds. The $\text{C-H}\cdots\text{O}$ or $\text{C}\cdots\text{O}$ weak interactions are also examined following complexation as cooperative terms. Consequently, adsorption of AP, AX and TC molecules on r- TiO_2 occurs favorably in a horizontal arrangement with predominant interactions of $>\text{C}=\text{O}$ or $-\text{COOH}$ groups of the molecules and Ti_{5f} sites of the surface.

2.3. Adsorption of ampicillin and amoxicillin molecules on anatase- TiO_2 (101) surface

2.3.1. Stable structures

The optimized geometries of anatase- TiO_2 (101) surface (a- TiO_2) and ampicillin (AP), amoxicillin (AX) molecules are displayed in Figure 2.6. Some

characterized parameters including bond length, angle are compared to experimental data and calculated results in previous studies [102], [118], [121], [136]. Accordingly, the calculated parameters in this work are in good agreement with previous reports in which the changes of bond lengths and angles are *ca.* 0.01-0.05 Å and 1-3°, respectively.

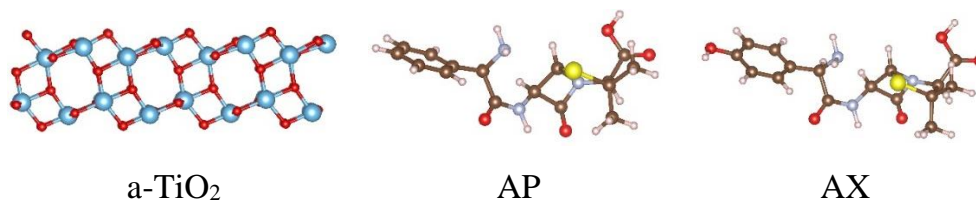


Figure 2.6. Optimized structures of anatase-TiO₂ (101) surface and ampicillin, amoxicillin molecules

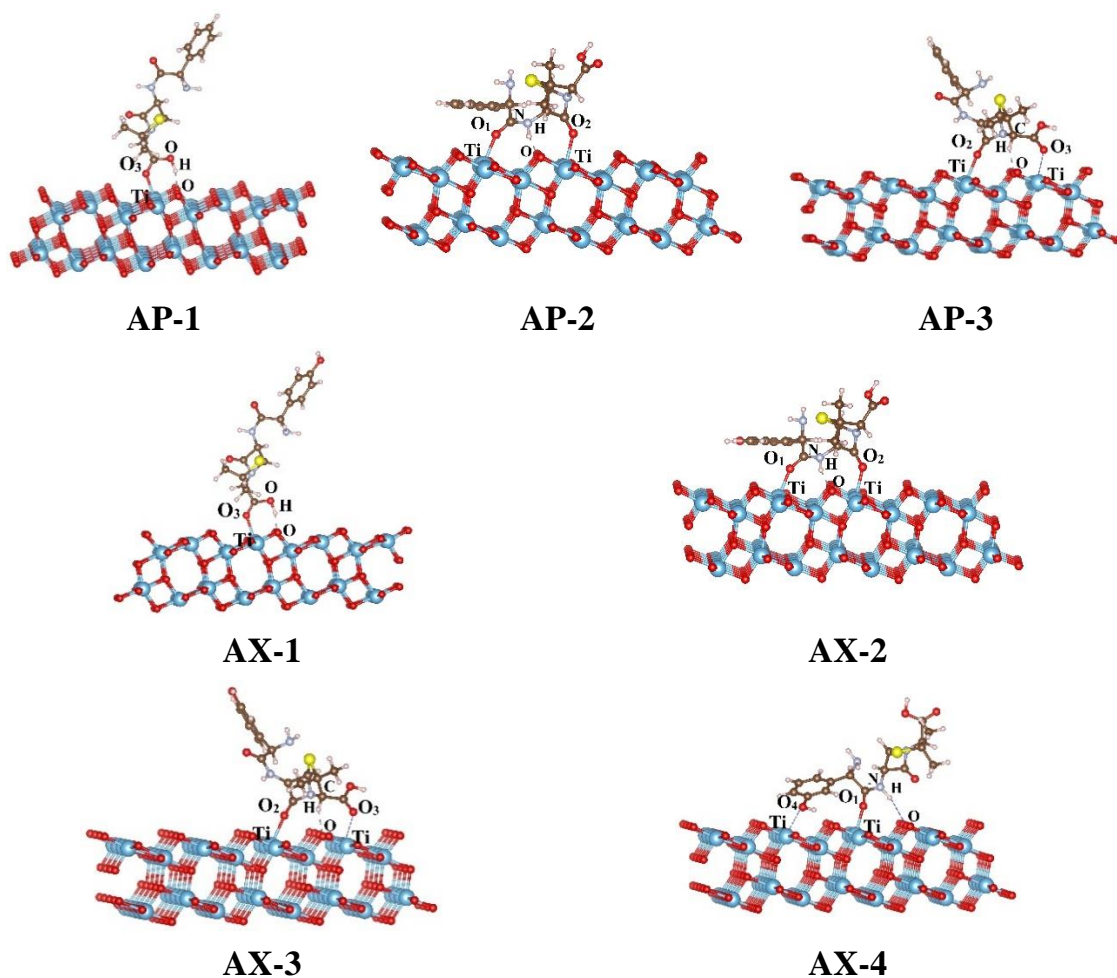


Figure 2.7. The optimized structures of ampicillin, amoxicillin adsorbed on anatase-TiO₂ (101) surface

The ground states of adsorption configurations of AP and AX molecules onto α -TiO₂ are illustrated in Figure 2.7. These structures are denoted by **AP-i** and **AX-i** (i = 1-4), following different arrangements of AP, AX molecules on the surface to have a conventional look. The **AX-4** is found out only for AX system due to the interaction of -OH group attached to the benzene ring as compared to AP system. Besides, the distances of intermolecular contacts and changes of bond lengths, angles are tabulated in Table 2.6.

Table 2.6. Some characteristic parameters of the stable complexes

	d(Ti...O)	d(H...O)	a(COTi)	a(O/N/CHO)	$\Delta r(\text{C}=\text{O})$	$\Delta r(\text{X}-\text{H})$	$\Delta r(\text{Ti}-\text{O})^{**}$
AP-1	2.16 ³	1.49	131.7	164.1	0.036	0.070	0.015 – 0.062
AP-2	2.13 ¹ /2.28 ²	1.64	153.3 ¹ /135.0	161.9	0.044/0.018	0.029	0.007 – 0.033
AP-3	2.22 ² /2.39 ³	1.86	163.2/130.8 ³	143.8	0.014/0.014	0.001	-0.018 – 0.011
AX-1	2.19 ³	1.52	131.9	164.2	0.035	0.062	0.004 – 0.067
AX-2	2.11 ¹ /2.30 ²	1.66	153.6 ¹ /135.5	161.7	0.027/0.018	0.028	-0.003 – 0.040
AX-3	2.26 ² /2.42 ³	1.89	163.8/130.3 ³	142.1	0.013/0.013	0.001	-0.026 – 0.019
AX-4	2.16 ¹ /2.43 ⁴	2.28/2.26 [*]	151.1/125.9 ⁴	160.0/160.2 [*]	0.023/0.017 ⁴	0.011/0.005 [*]	0.023 – 0.027

^{1,2,3,4}for O atoms in Fig.2; ^{*}for O-H...O; ^{**}for O atoms at bridging sites; a: angle (°); d: distance (Å)

As shown in Figure 2.7, the stable complexes obtained for two systems have similar geometrical structures, particularly for **AP-1** and **AX-1**, **AP-2** and **AX-2**, **AP-3** and **AX-3**. Table 3.6 indicates that the distances of Ti...O and O/N/C-H...O contacts are in range of 2.11 to 2.43 Å and 1.49 to 2.28 Å, respectively. These values are smaller than the total of van der Waals radii of atoms involved in contacts including Ti and O (3.82 Å), O and H (2.72 Å), C and O (3.22 Å) atoms [11]. Besides, the angles of C-O...Ti and O/N/C-H...O are corresponding to values of 125.9-163.8° and 142.1-164.2°, consistent with binding angles of C=O interactions or hydrogen bonds. Therefore, it can be suggested that the Ti...O and O/N/C-H...O intermolecular interactions are formed following complexation. Also, the geometrical changes for the surface and molecule are quite small in comparison with their initial structures. The change of Ti-O, C=O, X-H bonds is *ca.* 0.07 Å, 0.04 Å, and 0.07 Å, respectively.

The AP, AX molecules tend to arrange in horizontal sequence onto a-TiO₂ to form various intermolecular contacts, similarly to r-TiO₂ systems.

2.3.2. Adsorption energy

The adsorption energies (E_{ads}) are presented in Table 2.7. The E_{ads} values for AP and AX systems range from -17.7 to -31.1 kcal.mol⁻¹. The strength of adhesion of AP, AX on a-TiO₂ is comparable to that of antibiotics on r-TiO₂. Accordingly, these processes are considered as chemical adsorptions and slightly stronger for a-TiO₂ than for r-TiO₂. Moreover, the adsorption ability of these molecules onto TiO₂ surfaces is weaker than that on vermiculite. This is understood by the significant contributions of electrostatic interactions between Mg²⁺ cation sites on vermiculite and O atoms in >C=O groups of molecules.

Table 2.7. Adsorption energy (E_{ads} , kcal.mol⁻¹) of stable complexes

i	1	2	3	4
AP-i	-22.9	-31.1	-18.6	
AX-i	-21.0	-29.3	-17.7	-25.5

In addition, the stability of configurations in this system is contributed by both Ti···O attractive interactions and O/N/C-H···O hydrogen bonds as displayed in Figure 2.7. The contributions of two Ti···O intermolecular contacts of >C=O groups and one N-H···O hydrogen bond lead to the considerable stability of **AP-2**, **AX-2** in comparison to the rest of the configurations for AP, AX systems. In the case of **AX-4**, one Ti···O interaction is formed by Ti_{5f} site and O in -OH group. As given in Table 2.7, **AX-4** is slightly less stable than **AX-2** of 4 kcal.mol⁻¹. This result is due to the proton affinity (PA) at B3LYP/6-31++G(d,p) level and charge density at O atoms in the C=O groups (PAs are in the range of 200-216 kcal.mol⁻¹) are higher than those in -OH group (PA is *ca.* 185 kcal.mol⁻¹), leading to the fact that Ti···O (C=O) becomes more stable than Ti···O (OH). Besides, the difference of E_{ads} values for **AP-2** and **AX-2** is small *ca.* 2 kcal.mol⁻¹. The approximation of PA and deprotonation enthalpy (DPE) values at O atoms and N-H bond in AP and AX molecules as analyzed in the

previous section indicates the equally stable interactions in these configurations. In general, the adsorption ability of AP and AX onto a-TiO₂ is slightly different.

On the other hand, one Ti···O and one O-H···O contacts (**AP-1**, **AX-1**) or two Ti···O and one C-H···O contacts (**AP-3**, **AX-3**) have important roles in their stability. The adsorption energy increases in the order of **AP-2** < **AP-1** < **AP-3** and **AX-2** < **AX-4** < **AX-1** < **AX-3** for AP, AX systems, respectively. This is explained by reducing the ability of forming stable hydrogen bonds in configurations. The strength of hydrogen bonds increases in going from C-H···O to N-H···O and finally to O-H···O as estimated in the vermiculite system. Following this report, the significant contribution of O-H···O hydrogen bonds leads to the more stable configurations of **AP-1** and **AX-1** as compared to **AP-3**, **AX-3**, respectively. In summary, the stability of configurations depends on the arrangement of molecules on the surface to form stable interactions and is resulted by significant contribution of Ti···O electrostatic interactions and addition of O/N-H···O hydrogen bonds.

2.3.3. AIM and NBO analyses

To gain an insight into the existence and role of adsorptive interactions, we perform topology analysis including electron density ($\rho(r)$), Laplacian of electron density ($\nabla^2(\rho(r))$), a total of electron density energy ($H(r)$) and electron density transfers for the first layer of **AP-2**, **AX-2** most stable structures as displayed in Figure 2.8. The electron density transfers between molecules and the surface are investigated further to confirm the existence of intermolecular contacts. Some characteristic parameters are gathered in Table 2.8.

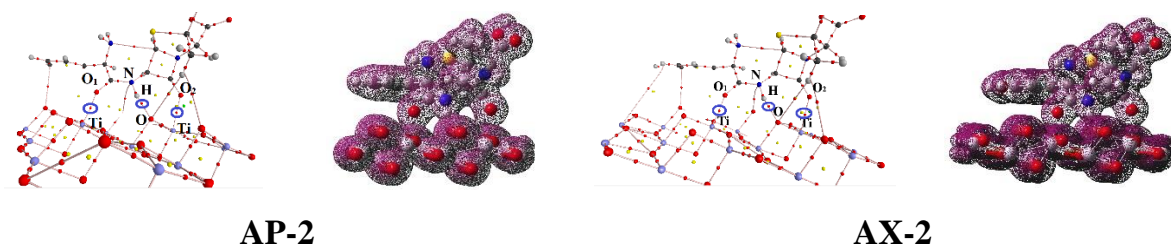


Figure 2.8. The topological geometries and EDT maps of the first-layered structures

Table 2.8. The topological analysis ($\rho(r)$, $\nabla^2(\rho(r))$, $H(r)$, au), electron density transfers (EDT, e), and hyper-conjugation energies (E^2 , kcal.mol⁻¹)

	BCPs	$\rho(r)$	$\nabla^2(\rho(r))$	$H(r)$	EDT	Transfers	E^2
AP-2	O ₁ ⋯Ti	0.056	0.325	0.004		$\pi(\text{C=O})/\text{LP}(\text{O}) \rightarrow$ $\text{LP}^*(\text{Ti})/\sigma^*(\text{Ti-O})$	23.6
	O ₂ ⋯Ti	0.039	0.204	0.004	0.12	$\pi(\text{C=O})/\text{LP}(\text{O}) \rightarrow$ $\text{LP}^*(\text{Ti})/\sigma^*(\text{Ti-O})$	16.9
	N-H⋯O	0.052	0.153	-0.008		$\text{LP}(\text{O}) \rightarrow \sigma^*(\text{N-H})$	22.6
AX-2	O ₁ ⋯Ti	0.058	0.340	0.003		$\pi(\text{C=O})/\text{LP}(\text{O}) \rightarrow$ $\text{LP}^*(\text{Ti})/\sigma^*(\text{Ti-O})$	22.6
	O ₂ ⋯Ti	0.037	0.194	0.004	0.10	$\pi(\text{C=O})/\text{LP}(\text{O}) \rightarrow$ $\text{LP}^*(\text{Ti})/\sigma^*(\text{Ti-O})$	17.0
	N-H⋯O	0.050	0.147	-0.007		$\text{LP}(\text{O}) \rightarrow \sigma^*(\text{N-H})$	19.3

The calculated results imply that the Ti⋯O and N-H⋯O intermolecular contacts exist. The electron density ($\rho(r)$) and Laplacian of electron density ($\nabla^2(\rho(r))$) values at Ti⋯O BCPs range from 0.037 to 0.058 au and from 0.194 to 0.340 au, respectively. Also, the $\rho(r)$ and $\nabla^2(\rho(r))$ at N-H⋯O BCPs correspond to 0.050-0.052 au and 0.147-0.153 au. All these values are within the region of $\rho(r)$ and $\nabla^2(\rho(r))$ for noncovalent interactions [9], [49]. Therefore, the Ti⋯O and N-H⋯O are regarded as noncovalent interactions and hydrogen bonds, respectively. The $H(r)$ values at BCPs of N-H⋯O contacts are slightly negative, indicating that these interactions have a small part of covalent nature. Besides, the stability of **AP-2**, **AX-2** is additionally contributed by O⋯C weak interactions with the small $\rho(r)$ of 0.01 au. The $\rho(r)$ values at Ti⋯O and N-H⋯O BCPs in **AP-2** and **AX-2** are mostly approximate, hence, strength of interactions in these configurations is nearly equal. As a result, the stability of **AP-2** and **AX-2** is considered to be approximate.

Furthermore, the formation of adsorptive interactions is clarified by electron density transfers from molecules to surface and vice versa (cf. Fig. 2.8). As given in

Table 2.8, the EDT value is small positive, of 0.1 e due to the prominent transfers from molecules to surface. The existence of $\text{Ti}\cdots\text{O}$ contacts is confirmed by the transfers of electron density from lone pair of O atoms ($\text{LP}(\text{O})$) and bonding orbitals of $\text{C}=\text{O}$ ($\pi(\text{C}=\text{O})$) in molecules to unoccupied lone pair of Ti sites ($\text{LP}^*(\text{Ti})$) and anti-bonding orbitals of $\text{Ti}-\text{O}$ ($\sigma^*(\text{Ti}-\text{O})$) of $\alpha\text{-TiO}_2$. The $\text{N}-\text{H}\cdots\text{O}$ hydrogen bonds is formed by the electron density transfers from $\text{LP}(\text{O})$ of surface to $\sigma^*(\text{N}-\text{H})$ of molecules. These transfers of electron density are evaluated clearly by hyper-conjunction energies (E^2) (cf. Table 2.8). Accordingly, the E^2 values for formations of $\text{Ti}\cdots\text{O}$ and $\text{N}-\text{H}\cdots\text{O}$ interactions are in the range of 17-24 kcal.mol^{-1} and 19-23 kcal.mol^{-1} , respectively. Moreover, the stability of interactions is determined by electrostatic term based on charge densities at sites of molecule and surface. The high charge density at sites leads to forming strong electrostatic interactions. Following NBO calculations, the charge densities at O, H atoms (in AP, AX) and Ti, O sites (in $\alpha\text{-TiO}_2$) are in the ranges of -0.65 to -0.74 e; 0.47 to 0.48 e; 1.61 to 1.72 e; -0.97 to -0.98 e, respectively. Therefore, $\text{Ti}\cdots\text{O}$ interactions are stronger than $\text{N}-\text{H}\cdots\text{O}$ hydrogen bonds upon complexations. This result also leads to the fact that EDT values are positive values for **AP-2** and **AX-2**.

2.3.4. Summary

In the present work, we investigated the adsorption of ampicillin and amoxicillin molecules on anatase- TiO_2 (101) surface ($\alpha\text{-TiO}_2$) using density functional theory calculations. Obtained results show that the adsorption of these antibiotics on the $\alpha\text{-TiO}_2$ is considered as chemical adsorption. The stable complexes are contributed significantly by $\text{Ti}\cdots\text{O}$ electrostatic interactions along with $\text{O}/\text{N}/\text{C}-\text{H}\cdots\text{O}$ hydrogen bonds. The existence and role of adsorptive interactions in the most stable structures **AP-2** and **AX-2** are clarified on the basis of the electron density transfers and charge density distribution. Generally, the adsorption of ampicillin on $\alpha\text{-TiO}_2$ surface is slightly stronger than that of amoxicillin, *ca.* 2 kcal.mol^{-1} . The arrangement of molecules on the $\alpha\text{-TiO}_2$ tends to be preferable in a horizontal configuration and occurs on a large surface area to form stable interactions.

2.4. Adsorption of chloramphenicol molecule on a vermiculite surface

2.4.1. Geometrical structures

Geometry optimization of chloramphenicol (CP) and vermiculite surface was performed using the PBE functional, and their most stable conformation on the potential energy surface is presented in Figure 2.9. The MEP map of chloramphenicol calculated at the B3LYP/6-31++G(d,p) level with an electron density of 0.02 au and the region of -5.10^{-5} to $+0.15$ au is also illustrated in Figure 2.9. The adsorption of CP molecule to the vermiculite surface was studied using the GPAW program and the results are shown in Figure 2.10. Remarkably, the optimized structure of CP in this work is in good agreement with the experimental data in ref. [79].

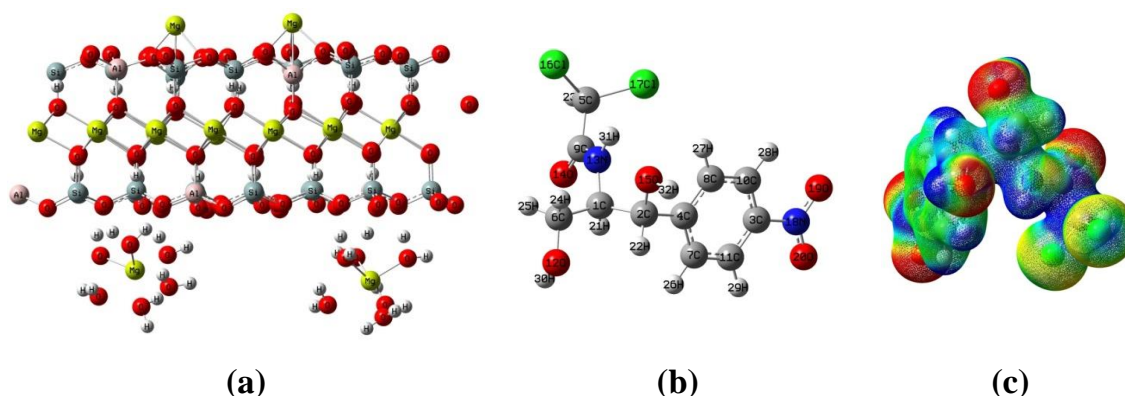


Figure 2.9. Optimized structures of **a)** vermiculite surface, and **b)** chloramphenicol molecule, and **c)** the MEP map of chloramphenicol (electron density of 0.02 au, from -5.10^{-5} to 0.15 au region).

Four stable complexes, denoted as **CP1**, **CP2**, **CP3**, and **CP4**, arising from adsorption and interaction of chloramphenicol with the surface of vermiculite were found. In these structures, the adsorption sites of chloramphenicol on vermiculite are located on either the Mg^{2+} ions external to the surface (without water molecules) or the O^{2-} ions on the surface. Conversely, the molecule attaches to these sites on the surface through its high charge density regions. The stabilizing interactions for this adsorption process are formed between the Mg^{2+} ion (surface) and O, Cl atoms at negatively charged regions (molecule); and between O atom (surface) and H atoms of positively charged regions (molecule).

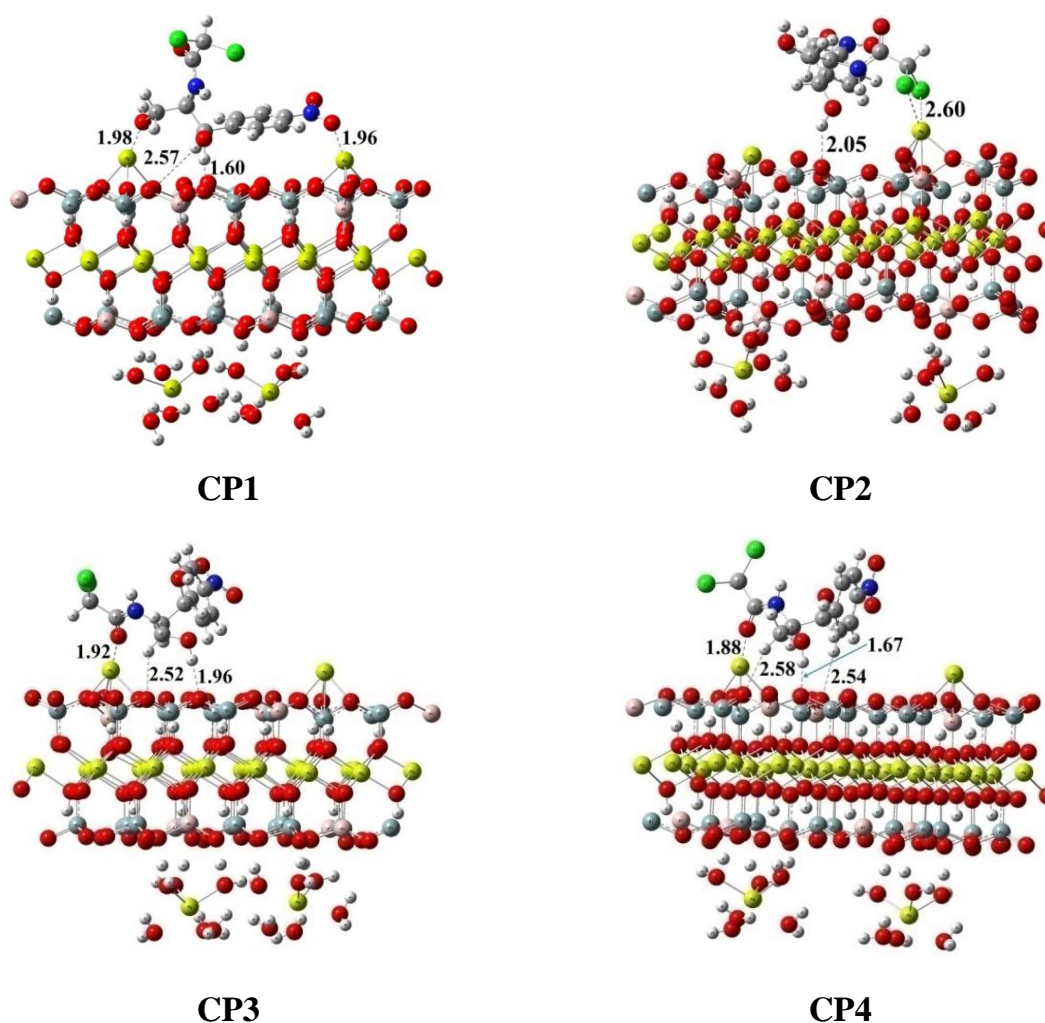


Figure 2.10. Stable adsorption configurations of chloramphenicol on the vermiculite surface

As shown in Figure 2.10, the distances of Mg \cdots O, Mg \cdots Cl, O-H \cdots O, and C-H \cdots O intermolecular contacts are relatively short, in the range of 1.88-1.98 Å, ~2.60 Å, 1.60-2.05 Å, and 2.52-2.58 Å, respectively. These values are in agreement with previous studies on the adsorption of organic compounds on clay mineral surfaces [20], [35]. For adsorption of (4-chloro-2-methylphenoxy) acetic acid (MCPA) and 2-(4-chlorophenoxy)-2-methylpropionic acid (clofibric acid, CA) on a mica surface, the stable complexes are formed by O-H \cdots O and O \cdots K intermolecular interactions. The corresponding intermolecular distances are in the range of 2.35-2.52 Å and 2.64-2.67 Å, respectively [111]. In addition, the distances related to the N \cdots Mg interactions in the stable complexes of benzodiazepines and vermiculite surface are from 2.11 to

2.17 Å [20]. All distances of O··Mg and O-H··O interactions are longer than those in our investigated system, and as a result, the stable configurations in the present work turn out to be more stable than those in previous studies.

2.4.2. Adsorption, interaction, and deformation energies

To get some insights into the adsorption process and the interactions of the adsorbed molecule on the solid surface, we performed calculations on their characteristics such as adsorption energy (E_{ads}), interaction energy (E_{int}), and deformation energies of the molecule ($E_{\text{def-mol}}$), and surface ($E_{\text{def-surf}}$). The deformation energy is also one of the important parameters to emphasize the requirements for the chloramphenicol molecule and the vermiculite surface to adjust (deform) their geometries, with the aim to better fit and interact with each other. All these values are calculated at PBE and vdW-DF-C09 functionals and listed in Table 2.9.

Table 2.9. Energetic aspects of adsorption of chloramphenicol on the vermiculite surface (all in kcal.mol⁻¹)

	PBE functional				vdW-DF-C09 functional			
	E_{ads}	E_{int}	$E_{\text{def-surf}}$	$E_{\text{def-mol}}$	E_{ads}	E_{int}	$E_{\text{def-surf}}$	$E_{\text{def-mol}}$
CP1	-84.7	-109.0	11.9	12.4	-106.5	-128.4	12.9	9.0
CP2	-27.2	-44.1	9.3	7.6	-43.5	-57.8	10.3	4.0
CP3	-38.6	-71.3	19.8	12.9	-54.0	-83.4	20.5	8.9
CP4	-64.9	-84.7	11.2	8.6	-81.9	-99.0	12.6	4.6

Table 2.9 shows that the adsorption energies of the located configurations, calculated with both the PBE and C09-vdW functionals, are large and increase in the order: **CP1** < **CP4** < **CP3** < **CP2**. This energetic quantity lies in the range of -43.5 to -106.5 kcal.mol⁻¹ by the vdW-DF-C09 functional, and of -27.2 to -84.7 kcal.mol⁻¹ by the PBE functional. It is noteworthy that using the vdW-DF-C09 functional that includes a consideration of van der Waals interactions, results in energy values *ca.* 12 - 22 kcal.mol⁻¹ more negative than with the PBE counterparts. The **CP1** configuration emerges as the most stable and favorable structure for adsorption of

chloramphenicol on vermiculite, with a larger adsorption energy of about 20-25 kcal.mol⁻¹ than the second stable configuration **CP4**. The formation of interactions upon the adsorption process is illustrated in Figure 2.10. According to results shown in Table 2.9, the interaction energies are significantly negative in the range of -44 to -109 kcal.mol⁻¹ by the PBE functional and -58 to -128 kcal.mol⁻¹ for the vdW-DF-C09 functional. Accordingly, these processes can be assigned as chemical adsorption. The interaction energy decreases from **CP1** to **CP4** to **CP3** and finally to **CP2**, similarly to the order of adsorption energies. Accordingly, the stability of these configurations is in the decreasing ordering of **CP1** > **CP4** > **CP3** > **CP2**. The interaction energies are more negative than their corresponding adsorption energies because the adsorption process also involves the endothermic deformations of the separated monomers. However, the ratio of deformation on the adsorption energies is relatively small and does not affect qualitatively the comparison between the four configurations. Therefore, similar to the trend of adsorption energy, the interaction energy of **CP1** is more negative than that of **CP2**, **CP3**, and **CP4**. As a consequence, the interaction between chloramphenicol and vermiculite surface is also the most favorable for **CP1** which has two strong Mg···O electrostatic interactions and two H···O hydrogen bonds formed upon the adsorption process.

The deformation energies of surface and molecule range from 9 to 21 kcal.mol⁻¹ and from 4 to 13 kcal.mol⁻¹, respectively, for different configurations. This result indicates that the deformation of a molecule is more convenient than that for the vermiculite surface. Considering the vermiculite surface, the deformation energy obtained using vdW-DF-C09 functional is larger than that using PBE functional by ~ 1 kcal.mol⁻¹. Conversely, the deformation energy for chloramphenicol using vdW-DF-C09 functional is smaller than that using PBE functional by ~ 4 kcal.mol⁻¹.

Generally, the adsorption ability of the chloramphenicol molecule by the vermiculite surface is quite strong. The adsorption of chloramphenicol is thus stronger than those of other organic compounds on vermiculite and other clay mineral surfaces as reported in previous studies [20], [35], [92]. In particular, the adsorption

energies of gemfibrozil, mefenamic acid, and naproxen molecules on vermiculite surface using the PBE functional are -66.9, -41.8, and -46.4 kcal.mol⁻¹, respectively [35]. The stability of these structures is due to the contribution of interactions between the -COOH group of the molecules and the Mg²⁺ ions or O atoms on the surface. Unfortunately, the role of weak hydrogen bonds (e.g. C-H...O) and the nature of other interactions are not evaluated in the previous investigation. Carvalho and co-workers performed some calculations on the adsorption of benzodiazepines to vermiculite surface using the PBE functional. Reported results showed that the adsorption energy of configurations that are stabilized by N...Mg interactions is about -24 kcal.mol⁻¹ [20]. Additionally, the adsorption energies of 2-(4-chlorophenoxy)-2-methylpropanoic acid and (4-chloro 2-methylphenoxy) acetic acid on a mica surface calculated using the PBE functional ranges from -14 to -20 kcal.mol⁻¹ [111]. All these values are thus less negative than those of the present work. That can be understood considering the significant contributions of the Mg...O, O-H...O intermolecular interactions and cooperative C-H...O weak hydrogen bond to the stability of configurations. Moreover, Mignon and co-workers reported that the N-H...O and O-H...O hydrogen bonds play an important role in the stability of complexes of DNA bases including adenine, cytosine, guanine, and the surface of montmorillonite [92]. Their interaction energies are in the range of -44 to -50 kcal.mol⁻¹, about twice smaller than those of configurations found in the present work.

2.4.3. Characteristics of stable interactions upon adsorption process

To clarify the property of interactions, the vertical proton affinity (PA) and deprotonation enthalpy (without any re-optimization. DPE) are calculated at B3LYP/6-31++G(d,p) and gathered in Table 2.10.

As presented in Table 2.10, the PA(O) indicates the gas-phase basicity of the two O atoms of the -NO₂ group (201.1 kcal.mol⁻¹) is slightly larger than that of the O atom of the >C=O group (199.9 kcal.mol⁻¹) and larger than that of the hydroxyl group -OH (193.2 kcal.mol⁻¹) and Cl atoms of the -CHCl₂ group (171.1 kcal.mol⁻¹). This implies that an attractive interaction of each O atom of the -NO₂ group is slightly

stronger than that of the O atom of the >C=O group and much more than that of O(OH) or Cl (-CHCl₂) atoms in chloramphenicol. Consequently, the electrostatic interaction between both Mg²⁺ and the O atoms of -NO₂ is slightly stronger than that with the other O and Cl atoms. This leads to the larger strength of the Mg...O (-NO₂, >C=O) contact as compared to the Mg...O (-OH) and then to Mg...Cl (-CHCl₂).

Table 2.10. Proton affinity (PA) at O and Cl atoms and vertical de-protonation enthalpy (DPE) of O-H and C-H bonds of chloramphenicol molecule (in kcal.mol⁻¹)

O, Cl sites and O-H, C-H bonds						
PA	199.0 (at O ₁₄) ^a	201.1 (at O ₁₉) ^b	193.2 (at O ₁₂) ^c	171.1 (at Cl ₁₆) ^d		
DPE	356.0 (O-H) ^e	345.4 (O-H) ^f	380.5 (C-H) ^g	366.1 (C-H) ^h	375.8 (C-H) ⁱ	371.0 (C-H) ^j

^a-in >CO; ^b-in -NO₂; ^c-in -OH; ^d-in -CHCl₂; ^e-O₁₂-H₃₀; ^f-O₁₅-H₃₂; ^g-C₆-H₂₅; ^h-C₂-H₂₂; ⁱ-C₇-H₂₆; ^j-C₁-H₂₁

For the proton acceptor at vermiculite surface, the stronger hydrogen bond should be obtained with the participation of O₁₅-H₃₂ covalent bond as compared to O₁₂-H₃₀, and also C-H bonds. This can be understood from the fact that the O₁₅-H₃₂ bond is slightly more polarizable than the O₁₂-H₃₀ bond and much more than C-H bonds. The reason is due to the smaller DPE value for the former in comparison with the latter, corresponding to the values of 345, 356, and in the range of 366 - 381 kcal.mol⁻¹. Thus, the stability of the configurations obtained upon the interaction between the chloramphenicol molecule and the surface of vermiculite tends to decrease in going from **CP1** to **CP4** to **CP3** and finally to **CP2**.

In addition, different values of the MEPs at the surface are represented by different colors, with potential values increasing in the order: red (more negative) < orange < yellow < green < blue (more positive). As displayed in Figure 2.9, the H atoms of -OH groups have a considerably positive charge, whereas the O atoms of -OH, -NO₂ and >C=O groups carry a significantly negative charge. It can be seen that the green color surrounding H atoms in CH₂ of the -CH₂OH group and CH of the -CHOH group, which is lighter than that of H atom in -OH group, indicates electron density with the less positive charge on H atoms of the -CH and -CH₂ groups. Consequently, the hydrogen bonds involving a -CH group in -CH₂OH and -CHOH

groups are less stable than those in -OH groups. Otherwise, two Cl atoms surrounded by yellow color have much less negative potential, and their interaction with a positive counterpart becomes weaker than those of the O atoms of the -OH, -NO₂, and >C=O moieties in chloramphenicol. Thus, the stability of configurations decreases in going from **CP1** to **CP4** to **CP3** and finally to **CP2** (Table 2.9).

To elucidate the results on interaction strength and the order of configuration stabilization, an AIM analysis was performed for intermolecular contacts with the first layer of the vermiculite surface interacting with chloramphenicol, tabulated in Table 2.11 and also illustrated in Figure 2.11. The hydrogen bonding energy (E_B) formed upon the adsorption process is calculated with the expression: $E_B = -0.5V(r)$ [40] and also given in Table 2.11.

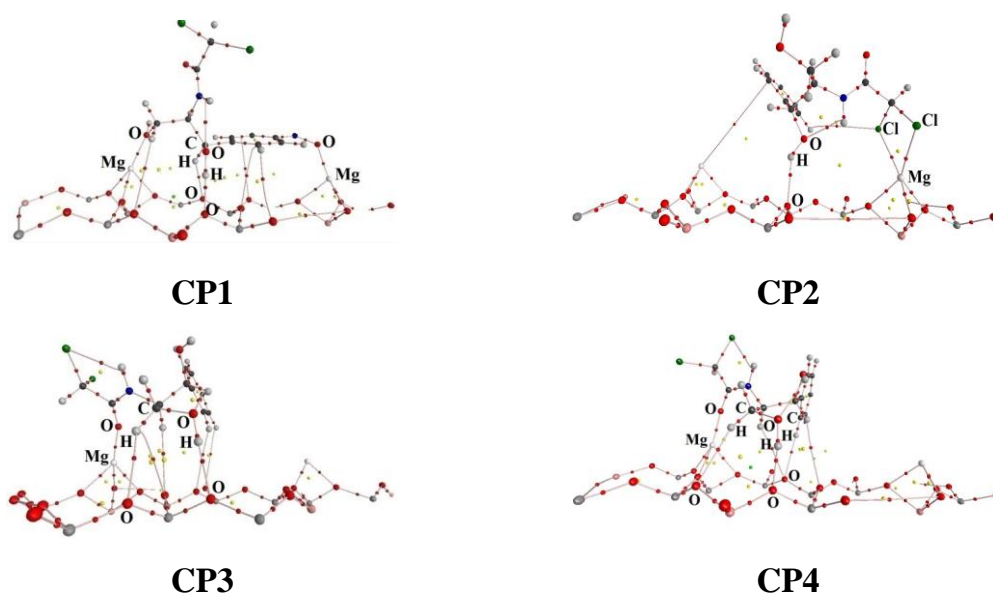


Figure 2.11. Topological features for the first layered structures of complexes

The presence of BCPs at intermolecular contacts as shown in Figure 2.11 and Table 2.11 implies that intermolecular interactions between atoms exist. The larger electron density at BCP points out to a stronger bond, and *vice versa*. Both values $\nabla^2\rho(r) > 0$ and $H(r) > 0$ imply a weak hydrogen bond and, conversely, $\nabla^2\rho(r) < 0$ and $H(r) < 0$ indicate a strong hydrogen bond. A hydrogen bond is partially strong when $\nabla^2\rho(r)$ is positive and $H(r)$ negative. The latter case represents a partly covalent bond in nature. For hydrogen bonds or weak interactions, the $\nabla^2\rho(r)$ and $\rho(r)$ are in the

range of 0.02-0.15 and 0.002-0.035 au, respectively [44]. In our studies, the $\nabla^2\rho(r)$ and $\rho(r)$ values at BCPs of blue-shifting hydrogen bonds are in the range close to these values [127].

Table 2.11. Topological analysis at the bond critical points (BCPs) of intermolecular contacts (in au), hydrogen bond energy (in kcal.mol⁻¹), and total electron density transfer (EDT, in e) of complexes

	BCP	$\rho(r)^a$	$\nabla^2(\rho(r))^b$	$G(r)^c$	$V(r)^d$	$H(r)^e$	E_B	EDT (e)
CP1	N-O...Mg	0.041	0.367	0.075	-0.059	0.017		
	H-O...Mg	0.042	0.359	0.074	-0.059	0.015		
	O-H...O	0.058	0.185	0.056	-0.065	-0.010	20.5	0.02
	C-H...O	0.008	0.031	0.006	-0.005	0.002	1.4	
CP2	O-H...O	0.021	0.071	0.017	-0.015	0.001	4.8	
	C-Cl1...Mg	0.017	0.088	0.018	-0.014	0.004		0.12
	C-Cl2...Mg	0.018	0.091	0.019	-0.014	0.004		
CP3	>C=O...Mg	0.045	0.433	0.088	-0.068	0.020		
	O-H...O	0.027	0.085	0.021	-0.021	0.001	6.5	0.02
	C-H...O	0.009	0.034	0.007	-0.005	0.002	1.6	
CP4	>C=O...Mg	0.050	0.499	0.103	-0.081	0.022		
	O-H...O	0.050	0.167	0.047	-0.053	-0.006	16.7	
	C-H(benz)...O	0.008	0.031	0.006	-0.005	0.002	1.4	-0.01
	C-H...O	0.008	0.029	0.006	-0.004	0.002	1.4	

^{a)} electron density; ^{b)} Laplacian of electron density; ^{c)} the electron kinetic energy density; ^{d)} the electron potential energy density; ^{e)} the total electron energy density

The hydrogen bond energies in both **CP1** and **CP4** configurations are quite large amounting up to 20.5 and 16.7 kcal.mol⁻¹ as given in Table 2.11. Additionally, the negative value of $H(r)$ at BCP of OH...O intermolecular contact indicates its partly covalent characteristic. The largest value of electron density at BCP (0.058 au) and hydrogen bond energy (20.5 kcal.mol⁻¹) of OH...O in **CP1** implies its significant strength relative to the rest of hydrogen bonds in the four configurations. Notably, in both **CP1** and **CP4** configurations, their stability is also contributed by strong Mg...O interactions with high electron densities (in the range of 0.041 to 0.050 au). Hence,

the intermolecular interactions in **CP1** are stronger than those in **CP4**, and significantly stronger than those in **CP2** and **CP3**.

Furthermore, the contribution of the strong Mg \cdots O interactions with 0.045 au electron density, and weak H \cdots O interactions with 0.009-0.027 au electron densities makes **CP3** quite stable, becoming stronger than **CP2** which has both weak Mg \cdots Cl and H \cdots O interactions. The energies of these hydrogen bonds are relatively small, in the range of 1.6 - 6.5 kcal.mol⁻¹. Thus, the interaction of chloramphenicol on a vermiculite surface is the most favorable for the **CP1** configuration as compared to the rest. Accordingly, the O-H \cdots O hydrogen bond formed between the O-H group of chloramphenicol molecule and the O site on the vermiculite surface plays a considerable role in stabilizing the complex configuration.

For a clearer understanding, the interaction on the first layer of the vermiculite surface is also considered from the natural bond orbital (NBO) approach. The total electron density transfer (EDT) between molecule and surface calculated at the B3LYP/6-31+G(d,p) level is illustrated at Figure 2.12 and presented in Table 2.11.

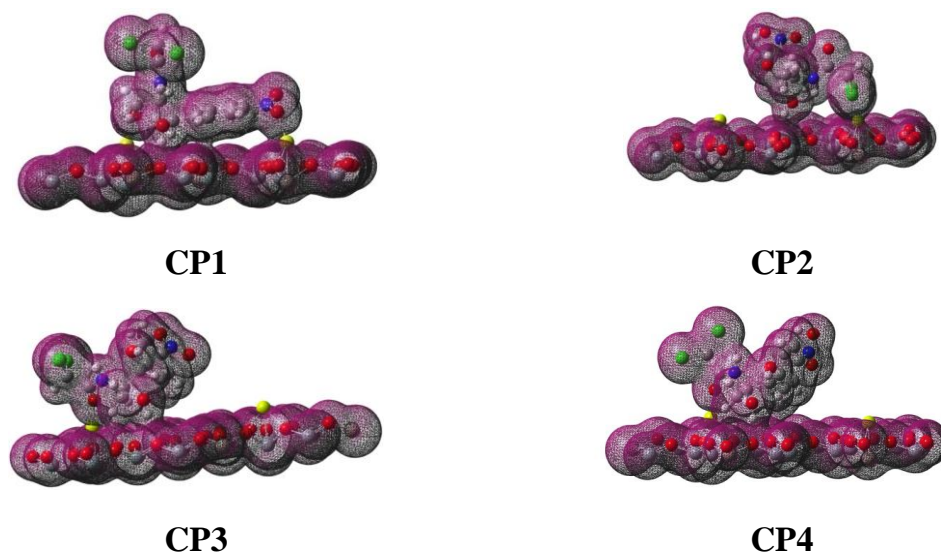


Figure 2.12. Total electron density distributions of the first-layered structures

The intermolecular interactions are formed in stable configurations because of the high electron density overlap between atoms involved in the interactions. The overlap of electron density in **CP1** is in fact larger than those for **CP2**, **CP3**, and **CP4**. NBO analysis results show that there are two transfers of electron density upon

complex formation in two opposing directions. The first transfer occurs from the lone pair of O atom ($n(\text{O})$) of chloramphenicol to the Mg^{2+} ion of the surface, thereby establishing the $\text{Mg}\cdots\text{O}$ interactions. The second transfer is from the $n(\text{O})$ atom of the surface to $\sigma^*(\text{O-H})$, $\sigma^*(\text{C-H})$ anti-bonding orbitals of the molecule to establish $\text{O}(\text{C})\text{-H}\cdots\text{O}$ hydrogen bonds. For **CP1**, **CP2**, and **CP3** the first transfer is slightly larger than the second one leading to their positive EDT values. For **CP4**, the first transfer is slightly smaller than the second one causing its negative EDT value. It is noted that the charge transfer from the $n(\text{O})$ atom of the surface to the $\sigma^*(\text{C-H})$ anti-bonding orbital of the molecule significantly contributes to the formation of $\text{C-H}\cdots\text{O}$ hydrogen bonds and EDT value. Consequently, the $\text{C-H}\cdots\text{O}$ hydrogen bonds act as an additional contribution to the stabilization of the investigated complexes.

2.4.4. Summary

In the present theoretical work, the adsorption of chloramphenicol to a vermiculite surface was studied using DFT calculations with the PBE and vdW-DF-C09 functionals. Four minima on the potential energy surface denoted as **CP1**, **CP2**, **CP3**, and **CP4**, are characterized as stable configurations upon interaction with the surface. Adsorption energies for these stable configurations are significantly negative and increase in the sequence **CP1** < **CP4** < **CP3** < **CP2**. The adsorption process is characterized as chemical adsorption, and largely favorable in the **CP1** configuration. The adherence of molecule to the surface is attained due to the effect of stabilized interactions between Mg^{2+} , O^{2-} ions of vermiculite surface and O, Cl, H atoms at the high charge density regions of chloramphenicol. The characteristics of $\text{Mg}\cdots\text{O}$, $\text{Mg}\cdots\text{Cl}$, and $\text{H}\cdots\text{O}$ interactions formed between molecule and surface were analyzed in some detail using the AIM, MEP and NBO approach. Remarkably, the $\text{O-H}\cdots\text{O}$ hydrogen bonds and $\text{Mg}\cdots\text{O}$ electrostatic interactions play an important role in the stability of adsorbate- surface complexes. The AIM analysis suggests that $\text{O-H}\cdots\text{O}$ hydrogen bonds in **CP1** and **CP4** have a part of covalent nature. The weaker $\text{C-H}\cdots\text{O}$ hydrogen bonds bring in also an important contribution to the complex stability and the charge transfer upon the adsorption process.

2.5. Adsorption of β -lactam antibiotics on vermiculite surface

2.5.1. Stable structures

Stable complex configurations formed from adsorption of β -lactam antibiotics molecules including ampicillin (AP), amoxicillin (AX), and benzylpenicillin (BP) on a vermiculite surface are optimized using the vdW-DF-C09 functional and performed by using the GPAW program. The minima on the potential energy surface located upon optimization are illustrated in Figure 2.13. Some characteristic parameters for optimized geometries are given in Table 2.12. The adsorption configurations for each interacting adsorbent-adsorbate system for the AP, AX, and BP molecules, denoted as **APi**, **AXi**, and **BPi**, respectively, with **i** = 1-5 corresponding to specific structures. The geometries for the AP system are in general similar to those for AX as well as BP following complexation.

Calculated results imply that the interactions in the resulting complexes are dominated by those between the Mg^{2+} ion (surface) and O, S atoms or π -electron aromatic ring at negatively charged regions (on molecules), and between the O^{2-} sites (surface) and H atoms at positively charged regions (on molecules). Details of the discussion are shown in the following section of MEP analysis. Consequently, the adhesion of these antibiotics molecules onto a vermiculite surface is favorable to form C-O/S \cdots Mg or Mg \cdots π and O-H \cdots O interactions between functional groups (eg. -COOH, -NH₂, -OH in most the complexes), especially in the horizontal arrangement of molecules, as illustrated in complexes **AP5**, **AX1**, **AX2**, **AX5**, **BP5**, which is in agreement with previous results. Furthermore, formation of electrostatic interactions or/and hydrogen bonds on material surface found here is also consistent with results in previous reports [16], [20], [23], [35], [53], [111], [141]. Noticeably, the Mg \cdots π intermolecular contact, which is observed for the first time, formed between cations and π -electron rings plays an additional role in stabilizing the structures. Accordingly, the attractive electrostatic interactions between cations (Mg^{2+}) on clay mineral surface and negative charge sites of the molecule (O, N, Cl), and hydrogen bonds of O/N/C-H \cdots O types tend to contribute significantly to the stabilization of complexes.

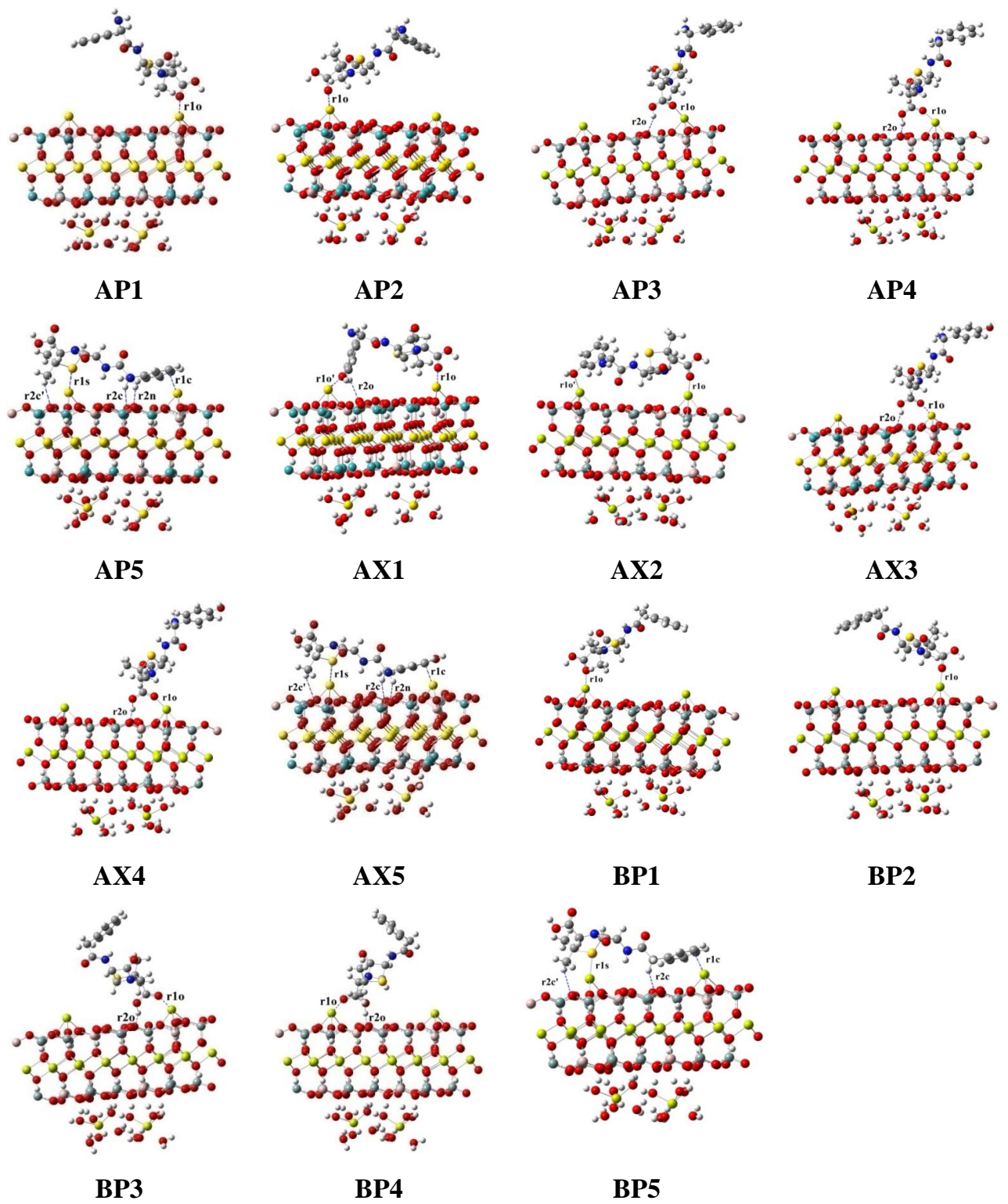


Figure 2.13. Stable complexes of adsorption of AP, AX and BP on a vermiculite surface

Table 2.12. Some selected parameters for optimized complexes shown in Figure 2.13 (bond distances in Angstrom (Å) and angles in degree (°), values from DFT computations) ^{*)}

	Mg...X (r1X)	Y-H...O (r2Y)	∠ C-X...Mg	∠ Y-H...O	Δr(C-X)	Δr(Y-H)
AP1	1.96 ^{a)}		159.0 ^{a)}		0.020 ^{a)}	
AP2	1.93 ^{a)}		178.2 ^{a)}		0.021 ^{a)}	
AP3	1.92 ^{a)}	2.56 ^{a)}	157.7 ^{a)}	138.7 ^{a)}	0.022 ^{a)}	0.012 ^{a)}
AP4	1.90 ^{a)}	1.49 ^{a)}	153.1 ^{a)}	167.5 ^{a)}	0.041 ^{a)}	0.095 ^{a)}
AP5	2.48 ^{d)} /2.40 ^{c)}	2.37/2.52 ^{b)} 2.34/2.67 ^{c)}	131.1/91.1 ^{d)} 76.1/70.3 ^{c)}	147.3 ^{b)} /122.3 ^{c)}	0.018 ^{a)}	0.012 ^{b)} /0.015 ^{c)}
AX1	1.92 ^{a)} /1.95 ^{a)}	2.64 ^{a)}	161.5/124.0 ^{a)}	147.4/88.1 ^{a)}	0.025/0.072 ^{a)}	0.008 ^{a)} /0.002 ^{d)}
AX2	1.94/2.04 ^{a)}		157.2/116.2 ^{a)}		0.030/0.076 ^{a)}	
AX3	1.93 ^{a)}	2.56 ^{a)}	157.5 ^{a)}	138.2 ^{a)}	0.027 ^{a)}	0.012 ^{a)}
AX4	1.90 ^{a)}	1.49 ^{a)}	153.0 ^{a)}	167.2 ^{a)}	0.046 ^{a)}	0.095 ^{a)}
AX5	2.47 ^{d)} /2.36 ^{c)}	2.50/2.46 ^{b)} 2.34/2.71 ^{c)}	130.6/92.9 ^{d)} 90.0 ^{c)}	117.5 ^{b)} /174.2 ^{c)}	0.024 ^{c)} /0.029 ^{d)}	0.008 ^{b)} /0.009 ^{c)}
BP1	1.96 ^{a)}		159.5 ^{a)}		0.021 ^{a)}	
BP2	1.93 ^{a)}		178.4 ^{a)}		0.024 ^{a)}	
BP3	1.95 ^{a)}	1.56 ^{a)}	128.8 ^{a)}	125.8 ^{a)}	0.042 ^{a)}	0.066 ^{a)}
BP4	1.91 ^{b)}	1.49 ^{a)}	127.5 ^{a)}	125.5 ^{a)}	0.047 ^{a)}	0.094 ^{a)}
BP5	2.48 ^{d)} /2.41 ^{c)}	2.31/2.67 ^{c)}	131.2/91.4 ^{d)} 70.0/99.8 ^{c)}	126.8/128.1 ^{c)}	0.023 ^{d)} /0.018 ^{c)}	0.009 ^{c)}

^{*)} X = O, S, C (in benzene ring); Y = O, N, C; ^{a), b), c), d)} for O, N, C, S atoms involving directly in intermolecular interactions

The distances of Mg...O(S,C) and O(N,C)-H...O intermolecular contacts range from 1.90 Å to 2.48 Å and from 1.49 Å to 2.71 Å, respectively (Table 2.12). All values are smaller than the sum of van der Waals radii of atoms involving in interactions. Particularly, the total radii of atoms are 3.25 Å, 3.53 Å, 3.43 Å and 2.72 Å corresponding to Mg...O, Mg...S, Mg...C, and H...O contacts [11]. Therefore, it is initially suggested that the Mg...O(S,C/π), O(N,C)-H...O intermolecular interactions

are formed between functional groups in antibiotic molecules with Mg^{2+} and O^{2-} sites on the vermiculite surface. Complex configurations obtained for AP, AX and BP systems are quite similar upon surface interactions and their stability is only slightly different from each other. In **AP5**, **AX1**, **AX2**, **AX5**, **BP5** configurations, the inclusion of interactions such as electrostatic, cation- π interactions, and hydrogen bonds is involved. Although these interactions are associated with large distances, the interacting molecule is horizontally arranged on the vermiculite surface in the most stable molecule-surface complex. This aspect will be analyzed in more detail in the following section.

Consideration of the changes of bonds upon formation of complexes, the C=O/S/C and O/N/C-H bonds involved in interactions are slightly elongated in the range of 0.02-0.08 Å and 0.00-0.10 Å, respectively. The COMg and C-S/CMg bond angles gathered in Table 2.12 are in the range of 116°-178° and 70°-131°, respectively. The COMg bond angles increase in the ordering of **AP4** < **AP3** < **AP1** < **AP2**, **AX4** < **AX2** < **AX3** < **AX1** and **BP4** < **BP3** < **BP1** < **BP2** for the complexes formed, and they are slightly different for those of monomers. The various arrangements of antibiotic molecules onto the surface and interactive effects of functional groups upon complexation can be correlated with the trend for bond angles. Moreover, the Mg \cdots S/ π electrostatic interactions found in **AP5**, **AX5**, and **BP5** complexes bring in a significant contribution to the stability of complexes. The CSMg angles are nearly equal in three molecules and the CCMg is smaller in **AP5** than in **AX5** or **BP5**. Besides, the O/N/CHO angles range from 88° to 174° in which the largest value is for N-H \cdots O angle in **AX5**, and the smallest one for O-H \cdots O in **AX4**. Further, the OCO and COH angles for the -COOH group change only slightly *ca.* 1°-5° and 1°-19° upon C=O \cdots Mg interactions and O-H \cdots O hydrogen bonds, respectively, in which the larger change in **BP1** implies the stronger O-H \cdots O hydrogen bonds. Overall, interactions that occurred on the surface lead to small changes in bond distances and angles in the resulting complexes.

2.5.2. Energetic aspects of the adsorption process

Some energetic parameters including adsorption energy (E_{ads}), interaction energy (E_{int}), and deformation energies of molecules ($E_{\text{def-mol}}$) and surface ($E_{\text{def-surf}}$) are calculated and shown in Table 2.13.

Table 2.13. Adsorption energies (E_{ads}), interaction energies (E_{int}) and deformation energies for antibiotics and vermiculite surface ($E_{\text{def-mol}}$, $E_{\text{def-surf}}$) (in kcal.mol⁻¹)

Complexes	E_{ads}	E_{int}	$E_{\text{def-mol}}$	$E_{\text{def-surf}}$
AP1	-34.7	-47.0	4.5	7.8
AP2	-37.8	-50.7	5.5	7.4
AP3	-35.6	-54.7	10.7	8.4
AP4	-47.2	-77.7	19.4	11.2
AP5	-77.6	-100.2	13.1	9.5
AX1	-67.2	-97.4	14.5	15.8
AX2	-71.7	-94.7	15.4	7.6
AX3	-57.2	-79.8	14.2	8.5
AX4	-42.6	-77.7	23.9	11.2
AX5	-67.9	-99.2	20.4	10.9
BP1	-35.2	-46.9	4.0	7.7
BP2	-38.5	-50.7	4.9	7.3
BP3	-46.9	-70.3	8.8	14.6
BP4	-58.3	-83.8	12.0	13.5
BP5	-72.5	-91.5	10.5	8.6

Adsorption of an antibiotic molecule on the surface is evaluated, per convention, as a strong process with a highly negative adsorption energy E_{ads} . The amount is in the range of -34.7 to -77.6 kcal.mol⁻¹; -42.6 to -71.7 kcal.mol⁻¹ and -35.2 to -72.5 kcal.mol⁻¹ for AP, AX and BP systems, respectively (Table 2.13). Hence, these processes can be assigned as strong chemical adsorptions. Besides, the adsorption energies decrease in the sequence of **AP1** > **AP3** > **AP2** > **AP4** > **AP5** for

AP system. As a matter of fact that the ampicillin molecule is favored to adsorb to the vermiculite surface by horizontal arrangement (in **AP5**).

Similarly, in AX system, the trend of adsorption energy is going in the decreasing ordering of **AX4** > **AX3** > **AX1** > **AX5** > **AX2**. The amoxicillin molecule is also adsorbed favorably to the vermiculite surface by a horizontal arrangement (in **AX1**, **AX2**, **AX5**). Such a trend of changes in adsorption energy values for the AP and AX systems is again found out for the BP system. The adsorption energy E_{ads} is decreased in going from **BP1** to **BP2** to **BP3** to **BP4** and finally to **BP5** (for the benzylpenicillin molecule). Consequently, it should be underlined that the horizontal attachment appears to induce the most stabilizing interaction, likely due to the fact that in this configuration, the molecule is placed on a larger surface area upon adsorption process as compared to other possible arrangements.

The **AP5**, **AX2**, and **BP5** configurations emerge as the most favorable and thus stable structures characterized by the largest negative adsorption energies. In each of these complexes, stabilization is contributed by the $\text{Mg}\cdots\text{S}/\pi$ electrostatic interactions for **AP5**, **BP5**, and $\text{Mg}\cdots\text{O}$ one for **AX2**. The adsorption energy E_{ads} tends to increase in the sequence of ampicillin (**AP5**) < benzylpenicillin (**BP5**) < amoxicillin (**AX2**), even though their difference is quite small. This suggests that there is only a small difference in the adsorption ability of antibiotics molecules on the vermiculite surface, which marginally decreases in going from AP to BP and then to AX molecule.

Generally, adsorptions of the AP, AX, and BP molecules on the vermiculite surface are quite strong with large negative values. and more substantial than for other organic compounds [20], [35], [111]. In particular, the adsorption energies calculated using the PBE functional of gemfibrozil, mefenamic acid, and naproxen molecules adsorbed on the similar vermiculite surface amount to -67, -42, and -46 ($\text{kcal}\cdot\text{mol}^{-1}$), respectively [35]. Similarly, adsorption of benzodiazepines onto vermiculite surface was investigated by Carvalho and co-workers in which the complexes are mainly stabilized by $\text{Mg}\cdots\text{N}$ interactions, leading to adsorption energy of *ca.* $-24 \text{ kcal}\cdot\text{mol}^{-1}$

using the PBE functional [20]. Attachment of 2-(4-chlorophenoxy)-2-methylpropanoic acid and (4-chloro 2-methylphenoxy) acetic acid on a mica surface was observed and the corresponding adsorption energy values range from -19 to -20 kcal.mol⁻¹ (using the PBE functional) [111]. The N-H...O and O-H...O hydrogen bonds significantly contribute to the stability of complexes of RNA/DNA bases including adenine, cytosine, guanine, and the montmorillonite surfaces, an important type of clay mineral [92], [93]. The adsorption of the antibiotics on the vermiculite surface in the present work is estimated to be significantly stronger than that on activated carbons with an adsorption energy of *ca.* 10 kcal.mol⁻¹ which can be regarded as physisorption [114]. This observation can result from a considerable electrostatic attraction of Mg²⁺ sites of the vermiculite surface on the adsorption process as reported similarly for Na⁺, Ca²⁺ cations on kaolinite, pyrophyllite, montmorillonite surfaces [53], [95]. Therefore, it would be noteworthy for the adsorption process that one needs to consider the important role of both Mg...S and Mg...π or two Mg...O electrostatic interactions in the stabilization of structures.

The appearance of interactions from adsorption processes of antibiotic molecules is illustrated in Figure 2.13. The strength of interactions formed on the material surface is also given. Interaction energies of complexes range from -46.9 to -100.2 kcal.mol⁻¹ and increase from AP to AX and finally to BP system (Table 2.13). The interaction energies of complexes decrease in the ordering of **AP1 > AP2 > AP3 > AP4 > AP5**; **AX4 > AX3 > AX2 > AX1 > AX5** and **BP1 > BP2 > BP3 > BP4 > BP5**. The most negative values are obtained for **AP5**, **AX5**, and **BP5** configurations that are induced in horizontal arrangements. In other words, adhesion of antibiotic molecules onto vermiculite is preferred at both Mg²⁺ sites on the surface. Molecules containing the -COOH, -CS-, -OH groups, or π-electron rings could also strongly interact with vermiculite surface at its Mg²⁺, O²⁻ ions sites.

On the other hand, interaction energies are more negative than the corresponding adsorption energies, due to the inherent endothermic deformations of separate monomers. This effect is consistent with previous reports of adsorption of

the organic molecules on the mineral surfaces [20], [148]. Deformation energies are in the range of from 4.0 to 23.9 kcal.mol⁻¹ and 7.3 to 15.8 kcal.mol⁻¹ for molecules ($E_{\text{def-mol}}$) and surface ($E_{\text{def-surf}}$), respectively. Geometrical changes in both molecule and material surface are important characteristics. The molecular structure is, as expected, distorted more conveniently than that of the surface because of its freedom of motion. Structural changes in complexes are larger for AX than those for AP and BP systems. As a consequence, the complexes of AX have less negative adsorption energies than those of BP although they receive more negative interaction energies. In addition, the change of geometrical structure of monomers in **AX2** is less than that in **AX5**, leading to the more negative adsorption energy of **AX2** as compared to **AX5**.

2.5.3. Existence and role of different interactions upon complexation

2.5.3.1. Characteristic properties of molecules

To have a deeper understanding of the formation and strength of surface interactions, and also to evaluate the stability of complexes, we carry out calculations for the molecular electrostatic potential (MEP) maps (isovalues = 0.01 e/Å³; charge regions taken from -5.10⁻⁵ to 0.15 electron) as well as the DPE, the PA at different atoms and bonds of the free antibiotic molecules at the B3LYP/6-31++G(d,p) level. All results are illustrated in Figure 2.14 and listed in Table 2.14.

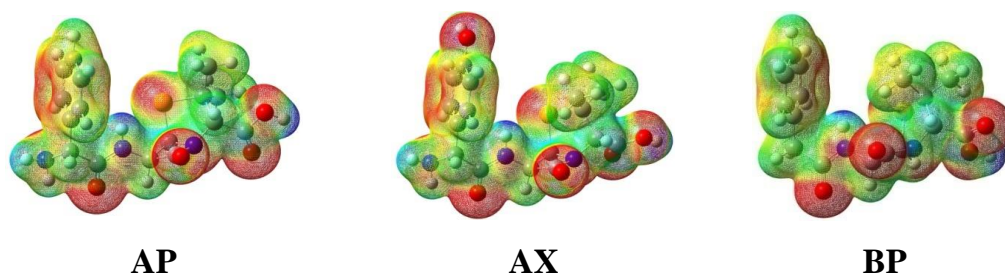


Figure 2.14. Molecular electrostatic potential (MEP) of free antibiotic molecules

The different colors of the MEPs represented to potential values in Figure 2.14 change from red (more negative) < orange < yellow < green < blue (more positive). Accordingly, the negative charge density (red color) is mostly located at O sites of C=O, C-O groups and higher than that at S atom (in C-S bond) or N atoms (in C-N, N-H bonds). Furthermore, the high negative charge density regions are located at π -

electron rings (benzene rings) in Figure 2.14. Conversely, positive charge density regions (blue color) are found predominantly at H atoms, higher in O-H than in N-H, C-H bonds. For the vermiculite surface, the high charge densities are, as expected, focused at Mg sites (positive charge) and O sites (negative charge). Hence, the electrostatic interactions are formed favorably between O/N/S or benzene ring, H atoms in molecules, and Mg^{2+} , O^{2-} sites in vermiculite surface. This result is further specified by DPE and PA analyses at different sites of the molecule.

Table 2.14. Proton affinity (PA) at atoms or π -ring and deprotonation enthalpy (DPE) of O(N,C)-H bonds of molecules ($kcal.mol^{-1}$, obtained from B3LYP/6-311++G(d,p) computations^{*)}

	PA						DPE				
	O1	O2	O3	O4	S	N	π -ring	C-H	N-H	O1-H	O2-H
AP	182.8	200.3	215.6		200.6	202.8	223.2	389.5	355.4	333.4	
AX	183.0	200.6	216.2	184.8	201.1	203.2	224.0	389.7	355.7	333.6	351.4
BP	183.6	200.9	216.1		200.0	203.0	218.0	385.3/369.5	352.8	335.2	

^{*)}(O1, O2, O3, O4 at $-COOH$, $>C=O_{ring}$, $>C=O$, $-OH$ groups; C-H, N-H, O1-H, O2-H in $-CH_3$, $-NH-$, $-COOH$, $-OH$ groups, respectively)

Calculated results tabulated in Table 2.14 indicate that DPE values of C-H bonds are in the range of 369.5 – 389.7 $kcal.mol^{-1}$. Corresponding values for N-H bonds are from 352.8 to 355.7 $kcal.mol^{-1}$. Similarly, the DPEs amount to 333.4 – 351.4 $kcal.mol^{-1}$ for O-H bonds. Accordingly, DPEs tend to decrease in the ordering of C-H > N-H > O-H leading to an increase of deprotonation ability to form $H \cdots O_{surf}$ (O_{surf} : O sites on vermiculite surface) hydrogen bonds in going from C-H to N-H and finally to O-H bonds. In addition, the PA is decreased from π -electron ring to O atoms of the $>C=O$ groups, to S, N atoms of the C-S, C-N groups, and finally to O atoms in $-OH$ groups. Remarkably, the PA at a π -electron ring is larger by ca. 10-20 $kcal.mol^{-1}$ than those at other sites (O, S, N atoms). Attractive interactions of π -electron ring with a positive charge region are thus considerably stronger than other interactions. This result specifies further for the difference of adsorption energies ca. 10-20 $kcal.mol^{-1}$ found for **AP5**, **AX5**, **BP5** with respect to other complexes (excepted for

AX1, **AX2**) as given in Table 2.13. Attractive interactions at O atoms (in $>C=O$ groups) with positively charged species are slightly stronger than those at S, N atoms. Consequently, the strength of $Mg\cdots\pi/O$ interactions is more significant than that of $Mg\cdots S/N$ ones. A combination of $Mg\cdots\pi$ and $Mg\cdots S$ or two $Mg\cdots O$ electrostatic interactions leads to higher stability of **AP5**, **AX5**; **AX1**; **AX2**, **BP5** complexes as compared to the rest of the structures. This is overall in good agreement with the analysis given above. In short, the MEP maps and DPE, PA parameters specified for the β -lactam antibiotics indicate that the $Mg\cdots\pi$ intermolecular interactions found in the **AP5**, **AX5**, and **BP5** structures play a considerable role in the stabilization of structures due to the adsorption process.

2.5.3.2. AIM and NBO analyses

To further probe the strength and role of interactions in the most stable complexes **AP5**, **AX2**, and **BP5**, an AIM analysis including the evolution of electron density ($\rho(r)$), Laplacian of electron density ($\nabla^2(\rho(r))$) and total electron energy density ($H(r)$) is now carried out for intermolecular contacts in the first layered structures. Some special parameters are tabulated in Tables 2.15, S4, S5, S6 (Appendix), and their topologies are displayed in Figure 2.15 and Figure S6 (Appendix). The hydrogen bonding energies (E_B) are also considered following the expression: $E_B = -0.5V(r)$ [88]. The presence of $Mg\cdots O/S/\pi$ and $O/N/C-H\cdots O$ BCPs at intermolecular contacts as shown in Figures 2.15, S6 (Appendix) and electron density values in Table 2.15 and Tables S4, S5, S6 (Appendix) implies the existence of these interactions.

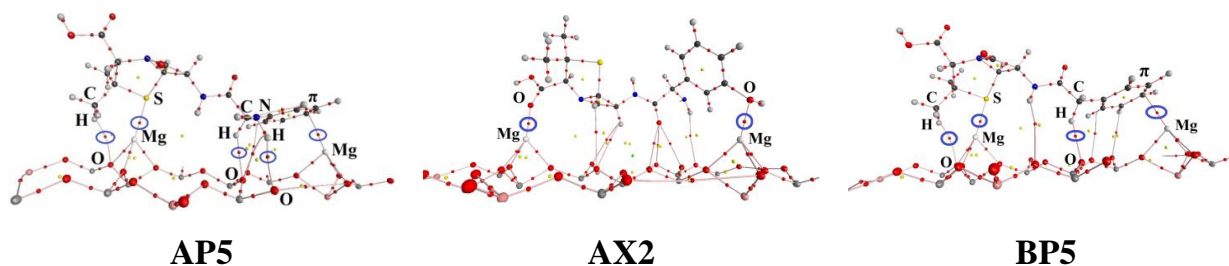


Figure 2.15. Topological features for the most stable adsorption configurations

Table 2.15. Topological analysis ($\rho(r)$, $\nabla^2\rho(r)$, au) at the bond critical points (BCPs), hydrogen bond energy (E_B , kcal.mol⁻¹) and total electron density transfer (EDT, e) of the most stable complexes at the B3LYP/6-31+G(d,p) level

	BCP	$\rho(r)$	$\nabla^2(\rho(r))$	H(r)	E_B	EDT
	Mg...S	0.031	0.132	0.002		
	C-H ¹ ...O	0.009	0.036	0.001	-1.4	
	C-H ² ...O	0.014	0.047	0.002	-2.7	
AP5	N-H...O	0.010	0.035	0.002	-1.7	0.16
		0.011	0.036	0.001	-2.0	
	C...O	0.008	0.027	0.001		
	Mg...C/ π	0.025	0.099	0.002		
	Mg...O*	0.045	0.387	0.016		
AX2	Mg...O**	0.039	0.282	0.011		0.08
	O...O	0.009	0.032	0.002		
	Mg...S	0.031	0.131	0.002		
	C-H ^a ...O	0.010	0.026	0.001	-1.4	
BP5	C-H ^b ...O	0.014	0.048	0.002	-2.8	0.16
	Mg...C/ π	0.024	0.097	0.002		
	C...O	0.008	0.027	0.001		

^{a,b}for H atoms in -CH₃ and -CH groups, *,** for O atoms in -C=O/-COOH, -OH groups

The electron density values at BCPs of intermolecular contacts in the complexes ranging from 0.039 – 0.052 (au), 0.031 – 0.032 (au), 0.024 – 0.027 (au) and 0.064 – 0.077 (au) for Mg...O, Mg...S, Mg... π . O-H...O, respectively, are within values of electron density for strong interactions [10]. Besides, the electron density values of 0.010 – 0.011 (au), 0.006 – 0.014 (au), 0.008 – 0.009 (au) correspond to N-H...O, C-H...O, C/O...O contacts. All these values are lying within the typical non-covalent interactions (the $\nabla^2\rho(r)$ and $\rho(r)$ are in the range of 0.020-0.150 and 0.002-0.035 (au), respectively) [10], [87]. Therefore, the stability of investigated complexes

arises considerably from Mg \cdots O/S/ π , O-H \cdots O strong interactions, and cooperative addition from N/C-H \cdots O, C/O \cdots O weak interactions.

Considering the **AP5**, **AX2**, **AX5**, and **BP5** highly stable configurations, it can be suggested the Mg \cdots O/S/ π intermolecular contacts with high electron density ranging from 0.024 to 0.052 (au) play an extremely important role in their stability. The electron density values at C/N-H \cdots O BCPs in the range of 0.006 – 0.014 (au) and the values of hydrogen bonding energy are small, in the range of 1.4 – 2.8 kcal.mol⁻¹. Hence, these hydrogen bonds additionally contribute to the stabilization of complexes along with the Mg \cdots O/S/ π interactions. Furthermore, as the $\rho(r)$ values at BCPs in **AP5**, **BP5**, **AX5** are nearly similar, the strengths of interactions in these complexes are only slightly different from each other. The high electron density values of 0.039 – 0.045 (au) at BCPs of Mg \cdots O contacts indicate a considerable contribution of the Mg \cdots O interactions in stabilizing **AX2**; this complex is thus slightly more stable than **AX5**. A stronger electrostatic attraction of Mg \cdots O as compared to Mg \cdots S contacts also lends support for this trend.

Notably, the hydrogen bond energies in configurations for **AP4**, **AX4**, and **BP3**, **BP4** are quite large ranging from 22.1 to 28.4 kcal.mol⁻¹ (cf. Tables S4, S5, S6). The negative values of H(r) at BCPs of these O-H \cdots O intermolecular contacts indicate their partly covalent nature. The large values of electron density at BCPs and binding energy of O-H \cdots O hydrogen bonds in these complexes specify their high strength as compared to the rest of hydrogen bonds in investigated systems. The stability of **AP4**, **AX4**, and **BP3**, **BP4** complexes is also cooperatively contributed by Mg \cdots O interactions with high electron densities (in the range of 0.047 to 0.052 (au)). Consequently, interactions between -COOH groups in AP, AX, BP molecules with the vermiculite surface are stabilized by both Mg \cdots O and O-H \cdots O intermolecular contacts upon complexation.

On the other hand, the genesis of interactions on the vermiculite surface can be revealed by using the NBO approach. Total electron density transfer (EDT) maps between molecules and surface are illustrated in Figures 2.16 and S7 (Appendix), and

typical values are given in Table 2.15 and Tables S4, S5, S6 (Appendix). More importantly, the molecular orbitals responsible for electron density transfer to induce interactions in complexes are displayed in Figures S8, S9, and S10 (Appendix). Intermolecular contacts are formed due to an electron density transfer and overlap between species involved in interactions (cf. Figure 2.16 and Figures S7, S8, S9, and S10 (Appendix)).

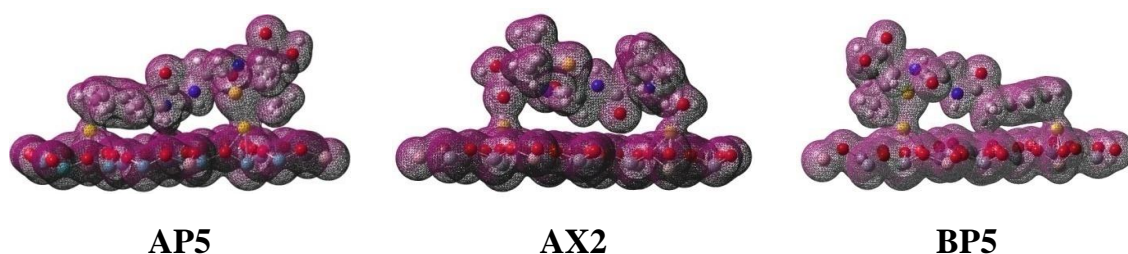


Figure 2.16. Total electron density maps of the most stable complexes

The overlaps of electron density in **AP5**, **AX1**, **AX2**, **AX5**, and **BP5** are in fact larger than those for the rest of the structures. Hence, these complexes are expected to be more stable. NBO results show two distinct electron density transfers upon complexation. The first transfer is from the lone pair of O atoms LP(O) on the surface to $\sigma^*(\text{O/N/C-H})$ anti-bonding orbitals of molecules to form O/N/C-H \cdots O hydrogen bonds. This is confirmed further by MOs images in Figures S8, S9, and S10 (Appendix). The second one is originated from bonding orbitals of $\pi(\text{C=O})$ in $-\text{COOH}$, $\sigma(\text{C-O/S})$ in $-\text{COH}$, $-\text{CS}$ groups, $\pi(\text{C=C})$ in benzene ring and lone pair of O, S atoms (LP(O/S)) in molecules to the Mg sites (LP*(Mg)) at the surface to form Mg \cdots O/S/ π intermolecular interactions. This result is displayed by the MOs images in Figure S8, S9, and S10 (Appendix). In addition, the overall EDT values become slightly positive ranging from 0.003 to 0.160 e for most of the complexes (given in Tables 2.15, S4, S5, and S6), because the first transfer is slightly smaller than the second. Conversely, EDT values for **AP4**, **AX4**, and **BP3**, **BP4** complexes are negative, ca. -0.070 e, since the first transfer is slightly stronger than the other counterpart. Moreover, the weak EDT from the n(O) orbital at the surface to the $\sigma^*(\text{C/N-H})$ anti-bonding orbitals of antibiotics forming C/N-H \cdots O hydrogen bonds adds an extra term to EDT values, and in the stabilization of complexes.

2.5.4. Summary

In the present theoretical work, the adsorptions of β -lactam antibiotics onto a vermiculite surface were investigated in detail by using DFT calculations. The minima on the potential energy surfaces were located upon interactions between the ampicillin (AP), amoxicillin (AX), and benzylpenicillin (BP) antibiotic molecules and the vermiculite surface. A horizontal trend of antibiotic molecules is geometrically preferred when they are adsorbed on the vermiculite surface. Adsorption energies for these stable complexes are large, in the range of -35 to -78 kcal.mol⁻¹, and slightly increase in the sequence of AP < BP < AX. Such stabilizing quantities confer these processes as strong chemical adsorption. Adhesion of antibiotics to vermiculite is favorable at the Mg²⁺, O²⁻ sites of the surface, and the >C=O, C-O, C-S, π -electron ring, O/N/C-H groups with the highly charged regions of the molecules. It is found that the Mg \cdots O/S/ π electrostatic interactions and O-H \cdots O hydrogen bonds determine the stability of complexes, in which the Mg \cdots π interaction has been detected for the first time, and plays an important role in the complexes stabilization.

The existence and stabilizing factors of interactions in complexes were thoroughly analyzed based on the AIM and NBO approaches. Remarkably, an AIM analysis indicates that most of these interactions have a non-covalent nature. NBO results also show that transfers of electron density from π (C=O/C), σ (C-S/C) and LP(O/S) orbitals in the molecules to the LP*(Mg) orbital to form Mg \cdots O/S/ π intermolecular interactions and from the LP(O) orbital in the surface to the σ^* (O/N/C-H) orbital to form O/N/C-H \cdots O hydrogen bonds are confirmed by the orbital shapes and electron density transfer maps.

CONCLUSIONS AND OUTLOOK

1. Conclusions

In this doctoral study, we performed quantum chemical calculations, using mainly density functional theory (DFT), to determine the main characteristics of the adsorption processes of organic and antibiotic molecules on materials surfaces including TiO₂ (both anatase and rutile forms) and clay minerals (such as kaolinite, vermiculite). The most important results have emerged as follows:

1. Concerning the mechanism of the adsorption of organic molecules including benzene derivatives and formic, acetic acids on rutile-TiO₂ (110) and anatase-TiO₂ (101) surfaces (r-TiO₂ and a-TiO₂), the adsorption processes are determined as chemisorptions characterized by high adsorption energies in the range of -10 to -31 kcal.mol⁻¹. Stability of the adsorptive configurations is mainly contributed by Ti···O/N electrostatic interactions with addition of O-H···O hydrogen bonds. Computed results indicate that the adsorption ability of these molecules on both r-TiO₂ and a-TiO₂ surfaces decreases in the order of -SO₃H > -COOH > -NH₂ > -NO₂ > -CHO > -OH. Besides, the adsorption of these molecules on r-TiO₂ is slightly stronger than that on a-TiO₂.

2. For kaolinite, calculated results on the adsorption of benzene derivatives on H-slab and K⁺-slab surfaces show that adsorption energies of the resulting complexes range from -3 to -25 kcal.mol⁻¹ (PBE functional) for H-slab and from -5 to -21 (PBE), -9 to -23 (vdW) kcal.mol⁻¹ for K⁺-slab. The stability of the configurations is mainly governed by O/N-H···O intermolecular contacts for H-slab and by O/N-H···O and K···O/N/C(π) for K⁺-slab. The adsorption ability of these molecules on kaolinite decreases in the order of -SO₃H > -COOH > -OH > -CHO > -NH₂ (H-slab) and -COOH ≥ -CHO > -NH₂ > -OH (K⁺-slab).

3. Regarding the adsorption of antibiotics molecules, including ampicillin (AP), amoxicillin (AX), enrofloxacin (ENR), and tetracycline (TC) on r-TiO₂ and a-TiO₂, it is found that adsorption of these molecules occurred onto r-TiO₂ and a-TiO₂

are characterized as chemisorption processes with associated energies of ca. -24 to -35 kcal.mol⁻¹ and -29 to -31 kcal.mol⁻¹ (PBE), respectively. The adsorption ability of these antibiotics on r-TiO₂ slightly decreases in the order of TC ≥ AX ≥ AP ≥ ENR, while for a-TiO₂, the adhesion of AP is slightly more favorable than that of AX. Quantum chemical analyses further illustrate the significant contributions of Ti···O electrostatic interactions and O/N/C-H···O hydrogen bonds to the stabilization of adsorption configurations. Remarkably, the most stable complexes tend to be formed preferably in horizontal arrangement along with Ti⁴⁺ sites on the r-TiO₂ and a-TiO₂ to form Ti···O strong electrostatic interactions. Moreover, the adsorption of AP and AX antibiotics on r-TiO₂ is slightly weaker than that on a-TiO₂.

4. The adsorption processes of chloramphenicol (CP) and β-lactam antibiotics, including ampicillin (AP), amoxicillin (AX), and benzylpenicillin (BP), on the vermiculite surface were thoroughly investigated. They are strong chemisorption processes characterized by large adsorption energies of ca. -72 to -107 kcal.mol⁻¹. The stability of the configurations mainly arises from Mg···O/Cl/S/π attractive electrostatic interactions and O/C-H···O hydrogen bonds. Each molecule prefers to arrange horizontally on the surface to form Mg···S and Mg···π contacts, or two Mg···O electrostatic interactions between S atom in -CS, π-electrons of a benzene ring or O atoms of -COOH, -OH groups in molecules and Mg²⁺ sites on the surface. Noticeably, an important role of the Mg···π interaction in the complex stabilization has been observed in the β-lactam antibiotics systems for the first time.

5. Some intermolecular contacts, including Ti···O, O/N-H···O, have slightly negative H(r) values at their BCPs and thus, they have a small covalent part. The existence of cations such as K⁺, Mg²⁺ on clay minerals surfaces (kaolinite, vermiculite) plays a crucial role in the adsorption ability of organic compounds.

From a methodological viewpoint, the vdW forces included in computations induce a considerable effect on geometrical structure, adsorption energy, and the nature of interactions between functional groups and surfaces. Overall, vermiculite

emerges to offer an efficient adsorption surface and can be used as a suitable material to remove antibiotics from wastewaters in comparison to kaolinite and TiO₂.

2. Outlook

Reactions and processes that occurred at materials surface phenomenon represent an important field of current research, and theoretical studies are expected to play a key role in the understanding of inherent mechanisms that are in turn of importance in materials science. Hence, we would suggest the following theoretical studies on different subjects such as:

1. Investigation of other surfaces of TiO₂ in adsorption of organic molecules;
2. The cations exchange on clay minerals to enhance the efficient adsorption and removal ability of antibiotics and organic molecules;
3. Theoretical calculations to evaluate the adsorption ability of antibiotics containing in wastewater (eg. tetracycline, enrofloxacin) on other materials such as graphene, graphene oxide, and activated carbon;
4. Study of 2D materials for photocatalytic activities, chemical and biochemical sensors, batteries, and many other applications;
5. Use of DFT methods in conjunction with vdW functionals, hybrid functionals in order to evaluate the structure and energy properties of adsorption of molecules and ions on material surfaces.

LIST OF PUBLICATIONS USED FOR THIS THESIS

1. **Nguyen Ngoc Tri**, Dai Q. Ho, A.J.P. Carvalho, Minh Tho Nguyen and Nguyen Tien Trung, Insights into adsorptive interactions between antibiotic molecules and rutile-TiO₂ (110) surface, *Surface Science*, **2021**, 703, 121723(1-8).
2. **Nguyen Ngoc Tri**, Nguyen Tien Trung, Theoretical study of geometry, stability and interaction in configurations of ampicillin and amoxicillin molecules on the surface of anatase-TiO₂ (101), *Quy Nhon University Journal of Science*, **2020**, 14(3), 71-77.
3. Nguyen Thi Thuy, **Nguyen Ngoc Tri**, Nguyen Tien Trung, A theoretical study on adsorption of organic molecules containing benzene ring onto kaolinite surface, *Quy Nhon University Journal of Science*, **2020**, 14(1), 5-14.
4. **Nguyen Ngoc Tri**, Minh Tho Nguyen and Nguyen Tien Trung, A molecular level insight into adsorption of β -lactam antibiotics on vermiculite surface, *Surface Science*, **2020**, 695, 121588(1-8).
5. **Nguyen Ngoc Tri**, Huynh Thi My Phuc, Nguyen Tien Trung, A theoretical investigation of interaction of organic molecules with anatase-TiO₂ (101) surface, *Vietnam Journal of Catalysis and Adsorption*, **2019**, 8(4), 42-48.
6. Huynh Thi My Phuc, **Nguyen Ngoc Tri**, Nguyen Tien Trung, Theoretical study on adsorption of organic molecules containing benzene ring onto rutile-TiO₂ (110) surface using density functional theory method, *Quy Nhon University Journal of Science*, **2019**, 13(5), 89-93.
7. **Nguyen Ngoc Tri**, Nguyen Tien Trung, Theoretical study on adsorption of benzylpenicilin molecule onto vermiculite surface, *Vietnam Journal of Chemistry*, **2019**, 57(4), 514-519.
8. **Nguyen Ngoc Tri**, Ho Quoc Dai, Nguyen Tien Trung, Chemisorption of enrofloxacin on rutile-TiO₂ (110) surface: a theoretical investigation, *Vietnam Journal of Science and Technology*, **2019**, 57(4), 449-456.
9. **Nguyen Ngoc Tri**, Quoc Dai Ho, Nguyen Tien Trung, Insight into the adsorption of organic molecules on rutile TiO₂ (110) surface: A theoretical study, *Vietnam Journal of Chemistry*, **2018**, 56(6), 751-756.
10. **Nguyen Ngoc Tri**, A.J.P. Carvalho, A.V. Dordio, Minh Tho Nguyen and Nguyen Tien Trung, Insight into the adsorption of chloramphenicol on a vermiculite surface, *Chemical Physics Letters*, **2018**, 699, 107-114.

REFERENCES

1. Ahmed M.B., Zhou J.L., Ngo H.H., Guo W. (2015), "Adsorptive removal of antibiotics from water and wastewater: Progress and challenges", *Science of the Total Environment*, 532, pp. 112-126.
2. Ahmed M.J. (2017), "Adsorption of quinolone, tetracycline, and penicillin antibiotics from aqueous solution using activated carbons: Review", *Environmental Toxicology and Pharmacology*, 50, pp. 1-10.
3. Aksu Z., Tunc O. (2005), "Application of biosorption for penicillin G removal: comparison with activated carbon", *Process Biochemistry*, 40, pp. 831-847.
4. Ali I., Asim M., Khan T.A. (2012), "Low cost adsorbents for the removal of organic pollutants from wastewater", *Journal of Environmental Management*, 113, pp. 170-183.
5. Amin M.T., Alazba A.A. and Manzoor U. (2014), "A review of removal of pollutants from water/wastewater using different types of nanomaterials", *Advances in Materials Science and Engineering*, 1, pp. 1-24.
6. Asim M., Khan T.A., Ali I. (2012), "Low cost adsorbents for the removal of organic pollutants from wastewater", *Journal of Environments*, 113, pp. 170-183.
7. Awad M. E., Galindo A. L., Setti M., Rahmany M. M. E., Iborra C. V. (2017), "Kaolinite in pharmaceutics and biomedicine", *International Journal of Pharmaceutics*, 533, pp. 34-48.
8. Awad M. E., Roa E. E., Sanchez A. B., Viseras C., Laguna A. H. and Diaz C. I. S. (2019), "Adsorption of 5 aminosalicylic acid on kaolinite surfaces at a molecular level", *Clay Minerals*, 54, pp. 49-56.
9. Bader R.F.W. (1995), *Atoms in molecules: A quantum theory*, Oxford: Oxford University Press.
10. Bankiewicz B., Matczak P. and Palusiak M. (2012), "Electron Density Characteristics in Bond Critical Point (QTAIM) versus Interaction Energy

- Components (SAPT): The Case of Charge-Assisted Hydrogen Bonding”, *Journal of Physical Chemistry A*, 116, pp. 452-459.
11. Batsanov S.S. (2001), “Van der Waals Radii of Elements”, *Inorganic Materials*, 37(9), pp. 871-885.
 12. Biegler-König F., Schonbohm J. (2000), *AIM 2000*, University of Applied Sciences, Bielefeld, Germany.
 13. Binh V. N., Dang N., Anh N. T. K., Ky L. X., Thai P. K. (2018), “Antibiotics in the aquatic environment of Vietnam: Sources, concentrations, risk and control strategy”, *Chemosphere*, 197, pp. 438-450.
 14. Bottero J.-Y., Rose J., and Wiesner M.R. (2006), “Nanotechnologies: tools for sustainability in a new wave of water treatment processes”, *Integrated Environmental Assessment and Management*, 2, pp. 391-395.
 15. Buchholz M., Xu M., Noei H., Weidler P., Nefedov A., Fink K., Wang Y., Wöll C. (2016), “Interaction of carboxylic acids with rutile TiO₂ (110): IR-investigations of terephthalic and benzoic acid adsorbed on a single crystal substrate”, *Surface Sciences*, 643, pp. 117-123.
 16. Budi A., Stipp S.L.S. and Andersson M.P. (2018), “Calculation of Entropy of Adsorption for Small Molecules on Mineral Surfaces”, *Journal of Physical Chemistry C*, 122, pp. 8236-8243.
 17. Busayaporn W., Torrelles X., Wander A., Tomić S., Ernst A., Montanari B., Harrison N. M., Bikondoa O., Joumard I., Zegenhagen J., Cabailh G., Thornton G., and Lindsay R. (2010), “Geometric structure of TiO₂ (110) (1x1): Confirming experimental conclusions”, *Physical Review B*, 81, pp. 153404 (1-4).
 18. Cabailh G., Torrelles X., Lindsay R., Bikondoa O., Joumard I., Zegenhagen J., and Thornton G. (2007), “Geometric structure of TiO₂ (110) (1x1): Achieving experimental consensus”, *Physical Review B*, 75, pp. 241403(1-4).
 19. Carretero M.I. (2002), “Caly minerals and their beneficial effects upon human health. A review”, *Applied Clay Science*, 21, pp. 155-163.

20. Carvalho A.J.P., Dordio A.V., Ramalho J.P.P. (2014), "A DFT study on the adsorption of benzodiazepines to vermiculite surfaces", *Journal of Molecular Modelling*, 20, pp. 2336 (1-8).
21. Carvalho E.D., David G.S. and Silva G.J. (2012), *Health and Environment in Aquaculture*, Janeza Trdine 9, 51000, Rijeka, Croatia.
22. Catauro M., Papale F., Roviello G., Ferone C., Bollino F., Trifuoggi M., Aurilio C. (2014), "Synthesis of SiO₂ and CaO rich calcium silicate systems via sol-gel process: bioactivity, biocompatibility, and drug delivery tests", *Journal of Biomedical Materials Research Part-A*, 102, pp. 3087-3092.
23. Chen J., Min F., Liu L., Liu C., Lu F. (2017), "Experimental investigation and DFT calculation of different amine/ammonium salts adsorption on kaolinite", *Applied Surface Sciences*, 419, pp. 241-251
24. Cigala R.M., Crea F., Stefano C.D., Sammartano S. and Vianelli G. (2017), "Thermodynamic Parameters for the Interaction of Amoxicillin and Ampicillin with Magnesium in NaCl Aqueous Solution, at Different Ionic Strengths and Temperatures", *Journal of Chemical and Engineering Data*, 62, pp. 1018-1027.
25. Cooper V.R. (2010), "Van der Waals density functional: An appropriate exchange functional", *Physical Review B*, 81, pp. 161104 (1-4).
26. Cramer C. J. (2004), *Essentials of Computational Chemistry*, John Wiley & Sons Ltd, England.
27. Deblonde T., Leguille C. C., Hartemann P. (2011), "Emerging pollutants in wastewater: A review of the literature", *International Journal of Hygiene and Environmental Health*, 214, pp. 442-448.
28. Dehghani M., Nasser S., Ahmadi M., Samaei M.R. and Anushiravani A. (2014), "Removal of penicillin G from aqueous phase by Fe³⁺-TiO₂/UV-A process", *Journal of Environmental Health Science & Engineering*, 12, pp. 56(1-7).
29. Deiana C., Fois E., Martra G., Narbey S., Pellegrino F. and Tabacchi G. (2016), "On the Simple Complexity of Carbon Monoxide on Oxide Surfaces: Facet-

- Specific Donation and Backdonation Effects Revealed on TiO₂ Anatase Nanoparticles”, *ChemPhysChem*, 17, pp. 1-6.
30. Deng L., Yuan P., Liu D., Bergaya F. A., Zhou J., Chen F., Liu Z. (2017), “Effects of microstructure of clay minerals, montmorillonite, kaolinite and halloysite, on their benzene adsorption behaviors”, *Applied Surface Science*, 143, pp. 184-191.
 31. Dias N.C., Steiner P.A., Braga M.C.B. (2015), “Characterization and Modification of a Clay Mineral Used in Adsorption Tests”, *Journal of Minerals and Materials Characterization and Engineering*, 3, pp. 277-288.
 32. Diebold U. (2003), “Structure and Properties of TiO₂ Surfaces: A Brief Review”, *Applied Physics A: Materials Science & Processing*, 76, pp. 681-687.
 33. Diebold U. (2003), “The surface science of titanium dioxide”, *Surface Science Reports*, 48, pp. 53-229.
 34. Dion M., Rydberg H., Schroder E., Langreth D. C. and Lundqvist B. I. (2004), “Van der Waals Density Functional for General Geometries”, *Physical Review Letters*, 92, pp. 246401.
 35. Dordio A. V., Miranda S., Ramalho J.P.P., Carvalho A.J.P. (2017), “Mechanisms of removal of three widespread pharmaceuticals by two clay materials”, *Journal of Hazardous Materials*, 323, pp. 575-583.
 36. Downs R.T., Wallace M.H. (2003), “The American Mineralogist crystal structure database”, *American Mineralogist*, 88, pp. 247-250.
 37. Dronskowski R. (2005), *Computational Chemistry of Solid State Materials*, Wiley, USA.
 38. Droge S.T.J. and Goss K.U. (2013), “Sorption of Organic Cations to Pyrophyllite Clay Minerals: CEC-Normalization, Salt Dependency, and the Role of Electrostatic and Hydrophobic Effects”, *Environmental Science and Technology*, 47, pp. 14224-14232.

39. Enkovaara I. and et al. (2010), "Electronic structure calculations with GPAW: a real-space implementation of the projector augmented-wave method", *Journal of Physics: Condensed Matter*, 22, pp. 253202 (1-24).
40. Espinosa E., Molins E., Lecomte C. (1998), "Hydrogen bond strengths revealed by topological analyses of experimentally observed electron densities", *Chemical Physics Letters*, 285, pp. 170-173.
41. Franco M.A.E., Carvalho C.B., Bonetto M.M, Soares R.P., Feris L.A. (2017), "Removal of amoxicillin from water by adsorption onto activated carbon in batch process and fixed bed column: Kinetics, isotherms, experimental design and breakthrough curves modelling", *Journal of Cleaner Production*, 161, pp. 947-956.
42. Frisch M.J. and et al. (2016), *Gaussian 09 (Revision A.02)*, Gaussian, Inc., Wallingford CT.
43. Fujishima A., Zhang X., Tryk D.A. (2008), "TiO₂ Photocatalysis and Related Surface Phenomena", *Surface Science Reports*, 63, pp. 515-582.
44. Fuster F., Grabowski S.J. (2011), "Intramolecular Hydrogen Bonds: the QTAIM and ELF Characteristics", *Journal of Physical Chemistry A*, 115, pp. 10078-10086.
45. Gaetano F.D, Ambrosio L., Raucci M.G., Marotta A., Catauro M. (2005), "Sol-gel processing of drug delivery materials and release kinetics", *Journal of Materials Science – Materials in Medicine*, 16, pp. 261-265.
46. Gao T., Pedersen J. A. (2005), "Adsorption of Sunfonamide Antimicrobial Agents to Clay Minerals", *Environmental Science and Technology*, 39, pp. 9509-9516.
47. Gaynes R. (2017), "The Discovery of Penicillin - New Insights After More Than 75 Years of Clinical Use", *Emerging Infectious Diseases*, 23(5), pp. 849-853.
48. Ghauch A., Tuqan A., Assi H.A. (2009), "Antibiotics removal from water: Elimination of amoxicillin and ampicillin by microscale and nanoscale ion particles", *Environmental Pollution*, 157, pp. 1626-1635.

49. Grabowski S.J. (2006), *Hydrogen Bonding - New Insights*, Springer, Dordrecht, Netherlands.
50. Grabowski S.J. (2013), "Non-covalent interactions - QTAIM and NBO analysis", *Journal of Molecular Modelling*, 19(11), pp. 4713-21.
51. Graslund S., Bengtsson B.E. (2001), "Chemicals and biological products used in south-east Asian shrimp farming, and their potential impact on the environment - a review", *Science of the Total Environments*, 280, pp. 93-131.
52. Graslund S., Holmstrom K., Wahlstrom A. (2003), "A field survey of chemicals and biological products used in shrimp farming", *Marine Pollution Bulletin*, 46, pp. 81-90.
53. Greathouse J.A., Cygan R.T., Fredrich J.T. and Jerauld G.R. (2017), "Adsorption of Aqueous Crude Oil Components on the Basal Surfaces of Clay Minerals: Molecular Simulations Including Salinity and Temperature Effects", *Journal of Physical Chemistry C*, 121, pp. 22773-22786
54. Grenni P., Ancona V., Caracciolo A.B. (2018), "Ecological effects of antibiotics on natural ecosystems: A review", *Microchemical Journal*, 136, pp. 25-39.
55. Gu S., Kang X., Wang L., Lichtfouse E., Wang C. (2019), "Clay mineral adsorbents for heavy metal removal from wastewater: a review", *Environmental Chemistry Letters*, 17, pp. 629-654.
56. Ha N.N., Ha N.T.T., Khu L.V., Cam L.M. (2015), "Theoretical study of carbon dioxide activation by metals (Co, Cu, Ni) supported on activated carbon", *Journal of Molecular Modelling*, 21, pp. 322 (1-9).
57. Hafner J. (2008), "Ab-Initio simulations of materials using VASP: Density-Functional Theory and beyond", *Journal of Computational Chemistry*, 29, pp. 2044-2078.
58. Harris R.G., Wells J.D., Johnson B.B. (2001), "Selective adsorption of dyes and other organic molecules to kaolinite and oxide surfaces", *Colloids Surfaces A: Physicochemical and Engineering Aspects*, 180, pp. 131-140.

59. Hemeryck A., Motta A., Lacaze-Dufaure C., Costa D., Marcus P. (2017), "DFT-D Study of Adsorption of Diaminoethane and Propylamine Molecules on Anatase (101) TiO₂ Surface", *Applied Surface Science*, 426, pp. 107-115.
60. Henderson M.A. (2011), "A Surface Science Perspective on TiO₂ Photocatalysis", *Surface Science Reports*, 66, pp. 185-297.
61. Henderson M.A., Lyubinetsky I. (2013), "Molecular-level insights into photocatalysis from scanning probe microscopy studies on TiO₂ (110)", *Chemical Reviews*, 113, pp. 4428-4455.
62. Holmstrom K., Graslund S., Wahlstrom A., Pongshompoo S., Bengtsson B. E. and Kautsky N. (2003), "Antibiotic use in shrimp farming and implications for environmental impacts and human health", *International Journal of Food and Technology*, 38, pp. 255-266.
63. Ismadji S., Soetaredjo F.E., Ayucitra A. (2015), *Clay Materials for Environmental Remediation*, Springer Briefs in Green Chemistry for Sustainability.
64. Jensen F. (2007), *Introduction to Computational Chemistry*, Wiley, USA.
65. Ji L., Chen W., Duan L. and Zhu D. (2009), "Mechanisms for strong adsorption of tetracycline to carbon nanotubes: A comparative study using activated carbon and graphite as adsorbents", *Environmental Science and Technology*, 43, pp. 2322-2327;
66. Ji L., Wan Y., Zheng S. and Zhu D. (2011), "Adsorption of Tetracycline and Sulfamethoxazole on Crop Residue-Derived Ashes: Implication for the Relative Importance of Black Carbon to Soil Sorption", *Environmental Science and Technology*, 45, pp. 5580-5586
67. Johnson E.R. and Otero-De-La-Roza A. (2012), "Adsorption of organic molecules on kaolinite from the exchange-hole dipole moment dispersion model", *Journal of Chemical Theory and Computation*, 8, pp. 5124-5131.

68. Jurgen H. (2008), “Ab-Initio Simulations of Materials Using VASP: Density-Functional Theory and Beyond”, *Journal of Computational Chemistry*, 29, pp. 2044-2078.
69. Kamachi T., Tatsumi T., Toyao T., Hinuma Y., Maeno Z., Takakusagi S., Furukawa S., Takigawa I. and Shimizu K. (2019), “Linear Correlations between Adsorption Energies and HOMO Levels for the Adsorption of Small Molecules on TiO₂ Surfaces”, *Journal of Physical Chemistry C*, 123, pp. 20988–20997.
70. Karmous M.S. (2011), “Theoretical Study of Kaolinite Structure; Energy Minimization and Crystal Properties”, *World Journal of Nano Science and Engineering*, 1, pp. 62-66.
71. Kim B., Lee Y.-R., Kim H.-Y., Ahn W.-S. (2018), “Adsorption of volatile organic compounds over MIL-125-NH₂”, *Polyhedron*, 154, pp. 343-349.
72. Klimes J., Bowler D. R. and Michaelides A. (2011), “Van der Waals density functionals applied to solids”, *Physical Review B*, 83, pp. 195131(1-13).
73. Koch W., Holthausen M. C. (2001), *A Chemist’s Guide to Density Functional Theory*, Wiley-VCH Verlag GmbH, Germany.
74. Koppen S., Langel W. (2008), “Adsorption of small organic molecules on anatase and rutile surfaces: a theoretical study”, *Physical Chemistry Chemical Physics*, 10, pp. 1907-1915.
75. Kresse G., Joubert D. (1999), “From ultrasoft pseudopotentials to the projector augmented-wave method”, *Physical Reviews B*, 59(3), pp. 1758-1775.
76. Kumar P.S.V., Raghavendra V. and Subramanian V. (2016), “Bader’s Theory of Atoms in Molecules (AIM) and its Applications to Chemical Bonding”, *Journal of Chemical Sciences-Indian Academy of Sciences*, 128(10), pp. 1527-1536.
77. Landis C.R., Weinhold F. (2005), *Valency and bonding. a natural bond orbital donor acceptor perspective*, Cambridge Univ, Press Cambridge, U.K.
78. Lewars E.R. (2016), *Computational Chemistry*, Springer, Germany.

79. Liao P., Zhan Z., Dai J., Wu X., Zhang W., Wang K., Yuan S. (2013), "Adsorption of tetracycline and chloramphenicol in aqueous solutions by bamboo charcoal: A batch and fixed-bed column study", *Chemical Engineering Journal*, 228, pp. 496-505.
80. Liu H., Liew K.M. and Pan C. (2013), "Influence of hydroxyl groups on the adsorption of HCHO on TiO₂-B (100) surface by first-principles study", *Physical Chemistry Chemical Physics*, 15, pp. 3866-3880.
81. Liu X., Yang D., Li Y., Gao Y. and Liu W.-T. (2019), "Anisotropic Adsorption of 2-Phenylethyl Alcohol on a Rutile (110) Surface", *Journal of Physical Chemistry C*, 123, pp. 29759-29764.
82. Mahmood A., Shi G., Xie X. and Sun J. (2019), "Adsorption mechanism of typical oxygen, sulfur, and chlorine containing VOCs on TiO₂ (001) surface: First principle calculations", *Applied Surface Science*, 471, pp. 222-230.
83. Malandrino M., Abollino O., Giacomino A., Aceto M., Mentasti E. (2006), "Adsorption of heavy metals on vermiculite: Influence of pH and organic ligands", *Journal of Colloid and Interface Science*, 299, pp. 537-546
84. Manzhos S., Giorgi G., and Yamashita K. (2015), "A Density Functional Tight Binding Study of Acetic acid adsorption on crystalline and amorphous surfaces of Titania", *Molecules*, 20, pp. 3371-3388.
85. Maria B., Mingchun X., Heshmat N., Peter W., Alexei N., Karin F., Yuemin W. and Christof W. (2016), "Interaction of carboxylic acids with rutile TiO₂ (110): IR-investigations of terephthalic and axit benzoic adsorbed on a single crystal substrate", *Surface Science*, 643, pp. 117-123.
86. Martinez J. L. (2009), "Environmental Pollution by antibiotics and antibiotic resistance determinants", *Environmental Pollution*, 157, pp. 2893-2902.
87. Matta C.F., Boyd R.J. (2007), *The Quantum Theory of Atoms in Molecules: From Solid State to DNA and Drug Design*, WILEY-VCH Verlag GmbH & Co., KGaA, Weinheim.

88. Matta I., Alkorta I., Espinosa E., Molins E. (2011), "Relationships between interaction energy, intermolecular distance and electron density properties in hydrogen bonded complexes under external electric fields", *Chemical Physics Letters*, 507, pp. 185-189.
89. Mattsson A., Hu S., Osterlund L. and Hermansson K. (2014), "Adsorption of formic acid on rutile TiO₂ (110) revisited: An infrared reflection-absorption spectroscopy and density functional theory study", *Journal of Chemical Physics*, 140, pp. 034705(1-12).
90. Mattsson A., Osterlund L. (2017), "Co-adsorption of oxygen and formic acid on rutile TiO₂ (110) studied by infrared reflection-absorption spectroscopy", *Surface Science*, 663, pp. 47-55.
91. McKenzie M.E., Goyal S., Lee S.H., Park H., Savoy E., Rammohan A.R., Mauro J.C., Kim H., Min K. and Cho E. (2017), "Adhesion of Organic Molecules on Silica Surfaces: A Density Functional Theory Study", *Journal of Physical Chemistry C*, 121, pp. 392-401.
92. Mignon P. and Sodupe M. (2012), "Theoretical study of the adsorption of DNA bases on the acidic external surface of montmorillonite", *Physical Chemistry Chemical Physics*, 14, pp. 945-954.
93. Mignon P., Ugliengo P. and Sodupe M. (2009), "Theoretical Study of the Adsorption of RNA/DNA Bases on the External Surfaces of Na⁺-Montmorillonite", *Journal of Physical Chemistry C*, 113, pp. 13741-13749.
94. Naghdi M., Taheran M., Brar S.K., Kermanshahi-pour A., Verma M., Surampalli R.Y. (2018), "Removal of pharmaceutical compounds in water and wastewater using fungal oxidoreductase enzymes", *Environmental Pollution*, 234, pp. 190-213.
95. Nairi V., Medda L., Monduzzi M., Salis A. (2017), "Adsorption and release of ampicillin antibiotic from ordered mesoporous silica", *Journal of Colloid and Interface Science*, 497, pp. 217-225.

96. Nakata K., Fujishima A. (2012), "TiO₂ photocatalysis: Design and applications", *Journal of Photochemistry and Photobiology C: Photochemistry Reviews*, 13, pp. 169–189.
97. *NIST webpage*: <http://webbook.nist.gov/chemistry>; <http://cccbdb.nist.gov>.
98. Obare S.O. and Meyer G.J. (2004), "Nanostructured materials for environmental remediation of organic contaminants in water", *Journal of Environmental Science and Health - Part A*, 39, pp. 2549-2582.
99. Ornelas N.J.R., Aguiar C.R., Moraes S.M.O., Adriano W.S., Goncalves L.R.B. (2010), "Activated Carbon Adsorbent for the Aqueous Phase Adsorption of Amoxicillin in a fixed Bed", *Chemical Engineering and Technology*, 33, pp. 658-663.
100. Otker H.M. and Balcioglu I.A. (2005), "Adsorption and Degradation of Enrofloxacin, a Veterinary Antibiotic on natural Zeolite", *Journal of Hazardous Materials*, 122, pp. 251-258.
101. Pan X. and et al. (2013), "A DFT study of gas molecules adsorption on the anatase (001) nanotube arrays", *Computational Materials Science*, 67, pp. 174-181.
102. Pang C. L., Lindsay R. and Thornton G. (2008), "Chemical reactions on rutile TiO₂ (110)", *Chemical Sociality Reviews*, 37, pp. 2328-2353.
103. Parameswari A., Soujanya Y. and Sastry G.N. (2019), "Functionalized Rutile TiO₂ (110) as a Sorbent To Capture CO₂ through Noncovalent Interactions: A Computational Investigation", *Journal of Physical Chemistry C*, 123, pp. 3491-3504.
104. Perdew J.P., Burke K., Ernzerhof M. (1996), "Generalized Gradient Approximation Made Simple", *Physical Review Letters*, 77, pp. 3865-3868.
105. Peterson J.W., Petrasky L.J., Seymour M.D., Burkhart R.S., Schuiling A.B. (2012), "Adsorption and breakdown of penicillin antibiotic in the presence of titanium oxide nanoparticles in water", *Chemosphere*, 87(8), pp. 911-917.

106. Pico Y., Andreu V. (2007), Fluoroquinolones in soil—risks and challenges, *Analytical and Bioanalytical Chemistry*, 387, pp. 1287-1299.
107. Pouya E. S., Abolghasemi H., Assar M., Hashemi S.J., Salehpour A., Foroughidahr M. (2015), “Theoretical and experimental studies of benzoic acid batch adsorption dynamics using vermiculite-based adsorbent”, *Chemical Engineering Research and Design*, 93, pp. 800-811.
108. Pouya E. S., Abolghasemi H., Fatoorehchi H., Rasem B., Hashemi S.J. (2016), “Effect of dispersed hydrophilic silicon dioxide nanoparticles on batch adsorption of benzoic acid from aqueous solution using modified natural vermiculite: An equilibrium study”, *Journal of Applied Research and Technology*, 14, pp. 325-337.
109. Qin H. C., Qin Q. Q., Luo H., Wei W., Liu L. X., Li L. C. (2019), “Theoretical study on adsorption characteristics and environmental effects of dimetridazole on TiO₂ surface”, *Computational and Theoretical Chemistry*, 1150, pp. 10-17.
110. Ralf T. (2010), “Adsorption of Proline and Glycine on the TiO₂ (110) Surface: A Density Functional Theory Study”, *ChemPhysChem*, 11, pp. 1053-1061.
111. Ramalho J.P.P., Dordio A.V., Carvalho A.J.P. (2013), “Adsorption of two phenoxyacid compounds on a clay surface: a theoretical study”, *Adsorption*, 19, pp. 937-944.
112. Rautureau M., Gomes C.F., Liewig N. and Katouzian-Safadi M. (2017), *Clays and Health: properties and therapeutic uses*, Springer international publishing AG, Switzerland.
113. Sadegh H., Shahryari G.R., Masjedi A., Mahmoodi Z., Kazemi M. (2016), “A review on carbon nanotubes adsorbents for the removal of pollutants from aqueous solutions”, *International Journal of Nano Dimension*, 7, pp. 109-120.
114. Sellaoui L., Lima E.C., Dotto G.L., Lamine A.B. (2017), “Adsorption of amoxicillin and paracetamol on modified activated carbons: Equilibrium and positional entropy studies”, *Journal of Molecular Liquids*, 234, pp. 375-381.

115. Setvin M., Shi X., Hulva J., Simschitz T., Parkinson G. S., Schmid M., Valentin C. D., Selloni A. and Diebold U. (2017), "Methanol on Anatase TiO₂ (101): Mechanistic Insights into Photocatalysis", *ACS Catalysis*, 7, pp. 7081-7091.
116. Shen L., Liu Y., Xu H.L. (2010), "Treatment of ampicillin-loaded wastewater byh combined adsorption and biodegradation", *Journal of Chemical Technology and Biotechnology*, 85, pp. 814-820.
117. Singh R.K., Kim T.-H., Kim J.-J., Lee E.-J., Knowles J.C., Kim H.-W. (2013), "Mesoporous silica tubular nanocarriers for the delivery of therapeutic molecules", *RSC Advances*, 3, pp. 8692-8704.
118. Sowmiya M. and Senthilkumar K. (2016), "Adsorption of proline, hydroxyproline and glycine on anatase (001) surface: a first-principle study", *Theoretical Chemistry Accounts*, 135, pp. 12 (1-8).
119. Sushko M.L., Gal A.Y. and Shluger A.L. (2006), "Interaction of Organic Molecules with the TiO₂ (110) Surface: Ab Initio Calculations and Classical Force Fields", *Journal of Physical Chemistry B*, 110, pp. 4853-4862.
120. Tao J., Luttrell T., Bylsma J., Batzill M. (2011), "Adsorption of acetic acid on rutile TiO₂ (110) vs (011) - 2x1 Surfaces", *Journal of Physical Chemistry C*, 115, pp. 3434-3442.
121. Thomas A.G. and Syres K.L. (2012), "Adsorption of organic molecules on rutile TiO₂ and anatase TiO₂ single crystal surfaces", *Chemical Society Reviews*, 41, pp. 4207-4217.
122. Thomas A.G., Flavell W.R., Chatwin C.P., Kumarasinghe A.R., Rayner S.M., Kirkham P.F., Tsoutsou D., Johal T.K., Patel S. (2007), "Adsorption of Phenylalanine on Single Crystal Rutile TiO₂ (110) Surface", *Surface Science*, 601, pp. 3828-3832.
123. Tillotson M.J., Brett P.M., Bennett R.A., Crespo R.G. (2015), "Adsorption of organic molecules at the TiO₂ (110) surface: The effect of van der Waals interactions", *Surface Science*, 632, pp. 142-153.

124. Tonner R. (2010), “Adsorption of Proline and Glycine on the TiO₂ (110) Surface: A Density Functional Theory Study”, *ChemPhysChem*, 11, pp. 1053-1061.
125. Torelles X., Cabailh G., Lindsay R., Bikondoa O., Roy J., Zegenhagen J., Teobaldi G., Hofer W. A. and Thornton G. (2008), “Geometric structure of TiO₂ (011) (2x1)”, *Physical Review Letters*, 101, pp. 185501(1-4).
126. Treacy J.P.W. and et al. (2017), “Geometric structure of anatase TiO₂ (101)”, *Physical Review B*, 95, pp. 075416 (1-7).
127. Trung N. T., Minh T.N. (2013), “Interactions of carbon dioxide with model organic molecules: A comparative theoretical study”, *Chemical Physics Letters*, 581, pp. 10-15.
128. Tsuji Y., Yoshizawa K. (2018), “Adsorption and Activation of Methane on the (110) Surface of Rutile-Type Metal Dioxides”, *Journal of Physical Chemistry C*, 122, pp. 15359–15381.
129. Vorontsov A. V., Valdes H., Smirniotis P. G. and Paz Y. (2020), “Recent Advancements in the Understanding of the Surface Chemistry in TiO₂ Photocatalysis”, *Surfaces*, 2, pp. 72-92.
130. Wan Y., Fan Y., Dan J., Hong C., Yang S. and Yu F. (2019), “A review of recent advances in two-dimensional natural clay vermiculite based nanomaterials”, *Materials Research Express*, 6, pp. 102002 (1-30).
131. Wang A., Wang W. (2019), *Nanomaterials from Clay Minerals*, Elsevier Scientific publishing Company, Amsterdam, London, New York.
132. Wang G., Wu T., Li Y., Sun D., Wang Y., Huang X., Zhang G., Liu R. (2012), “Removal of ampicillin sodium in solution using activated carbon adsorption integrated with H₂O₂ oxidation”, *Journal of Chemical Technology and Biotechnology*, 87, pp. 623-628.
133. Wang J., Wang Z., Vieira C.L.Z., Wolfson J.M., Pingtian G., Huang S. (2019), “Review on the treatment of organic pollutants in water by ultrasonic technology”, *Ultrasonics – Sonochemistry*, 55, pp. 273-278.

134. Weinhold F., Glendening E.D. and et al. (2004), *NBO 5.G*, Wisconsin. Madison. WI.
135. Weng X., Cai W., Lan R., Sun Q., Chen Z. (2018), "Simultaneous removal of amoxicillin, ampicillin and penicillin by clay supported Fe/Ni bimetallic nanoparticles", *Environmental Pollution*, 236, pp. 562-569.
136. Wu G., Zhao C., Zhou X., Chen J., Li Y., Chen Y. (2018), "The interaction between HCHO and TiO₂ (101) surface without and with water and oxygen molecules", *Applied Surface Science*, 455, pp. 410-417.
137. Wu L., Wang Z., Xiong F., Sun G., Chai P., Zhang Z., Xu H., Fu C. and Huang W. (2020), "Surface chemistry and photochemistry of small molecules on rutile TiO₂ (001) and TiO₂ (011) - (2 x 1) surface: The crucial roles of defects", *Journal of Chemical Physics*, 152, pp. 044702.
138. Wurger T., Heckel W., Sellschopp K., Muller S., Stierle A., Wang Y., Noei H. and Feldbauer G. (2018), "Adsorption of Acetone on Rutile TiO₂: A DFT and FTIRS Study", *Journal of Physical Chemistry C*, 122, pp. 19481-19490.
139. Xiang Z. and David R.B. (2014), "DFT Studies of Adsorption of benzoic acid on the Rutile (110) Surface: Modes and Patterns", *Journal of Physical Chemistry C*, 9, pp. 1- 25.
140. Yadav S., Goel N., Kumar V., Tikoo K. and Singhal S. (2018), "Removal of Fluoroquinolone from Aqueous Solution using Graphene Oxide: Experimental And Computational Elucidation", *Environmental Science and Pollution Research*, 25, pp. 2942-2957.
141. Yang Z., Liu W., Zhang H., Jiang X., Min F. (2018), "DFT study of the adsorption of 3-chloro-2-hydroxypropyl trimethylammonium chloride on montmorillonite surfaces in solution", *Applied Surface Sciences*, 436, pp. 58-65
142. Yu C.H., Newton S.Q., Norman M.A., Schafer L. and Miller D.M. (2003), "Molecular dynamics Simulations of Adsorption of Organic Compounds at the Clay Mineral/Aqueous Solution Interface", *Structure Chemistry*, 14(2), pp. 175-185.

143. Yu F., Li Y., Han S. and Ma J. (2016), “Adsorptive removal of antibiotics from aqueous solution using carbon materials”, *Chemosphere*, 153, pp. 365-385.
144. Zaleska A. (2008), “Doped-TiO₂: A Review”, *Recent Patents on Engineering*, 2, pp. 157-164.
145. Zhang S., Sheng J.J., Qiu Z. (2016), “Water adsorption on kaolinite and illite after polyamine adsorption”, *Journal of Petroleum Science and Engineering*, 142, pp. 13-20.
146. Zhang X., Wang J., Dong X.-X., Lv Y.-K. (2020), “Functionalized metal-organic frameworks for photocatalytic degradation of organic pollutants in environment”, *Chemosphere*, 220, pp. 125114 (1-15).
147. Zhang Y., Zhang C.R., Wang W., Gong J.J., Liu Z.J., Chen H.S. (2016), “Density Functional Theory Study Of α -Cyanoacrylic Acid Adsorbed on Rutile TiO₂ (110) Surface”, *Computational and Theoretical Chemistry*, 1095, pp. 125-133.
148. Zhao H., Yang Y., Shu X., Wang Y., Ran Q. (2018), “Adsorption of organic molecules on mineral surfaces studied by first principle calculations: A review”, *Advances in Colloid and Interface Science*, 256, pp. 230-241.
149. Zhu D., Zhou Q. (2019), “Action and mechanism of semiconductor photocatalysis on degradation of organic pollutants in water treatment: A review”, *Environmental Nanotechnology, Monitoring & Management*, 12, pp. 100255 (1-11).
150. Zhu H., Chen T., Liu J. and Li D. (2018), “Adsorption of tetracycline antibiotics from an aqueous solution onto graphene oxide/calcium alginate composite fibers”, *RSC. Advances*, 8, pp. 2616-2621.

Appendix

1/ **Section 2.2.** From paper ‘Insights into adsorptive interactions between antibiotic molecules and rutile-TiO₂ (110) surface’, *Surface Science*, **2021**, 703, 121723(1-8).

Figures:

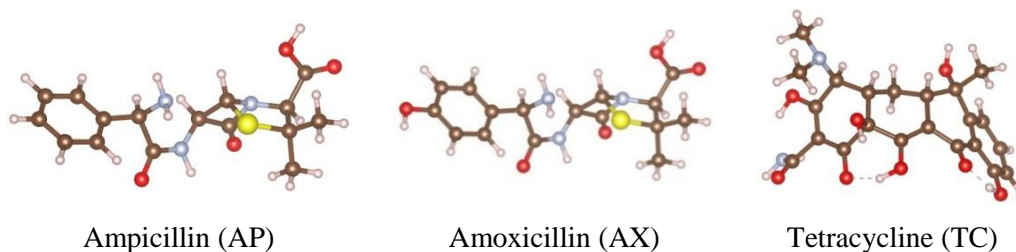


Figure S1. Optimized structures of antibiotic molecules using the PBE functional (C, H, O, N, F and S atoms are depicted in brown, white, red, cyan, green and yellow colors, respectively).

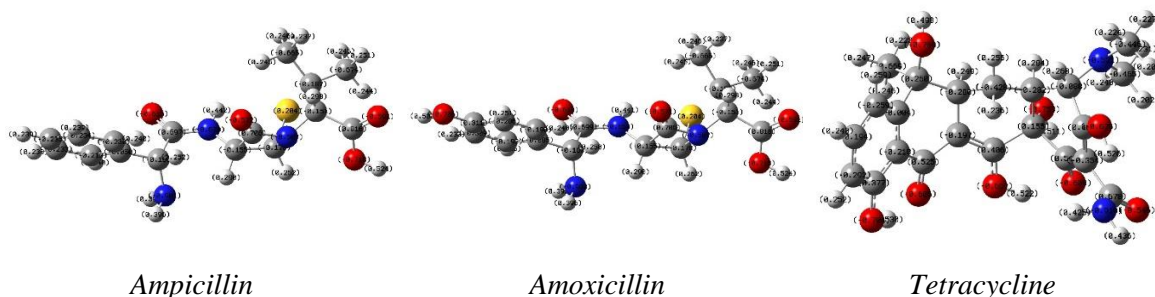


Figure S2. The distribution of NBO charge density for molecules at B3LYP/6-31++G(d,p) level.

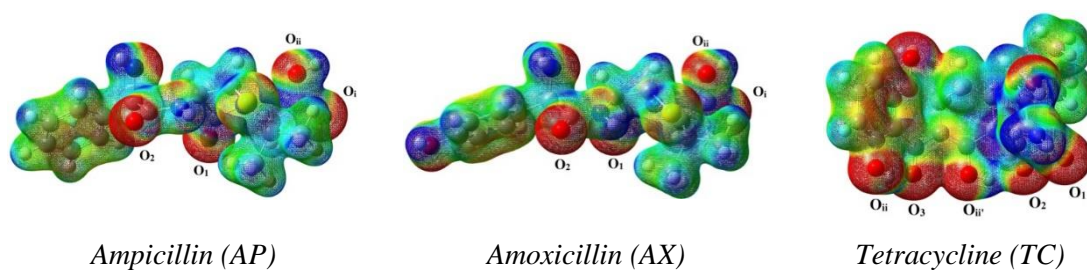


Figure S3. Molecular electrostatic potential maps for antibiotic molecules (isovalue = 0.01 au/Å³; charge regions: $-5 \cdot 10^{-5}$ to 0.10 e).

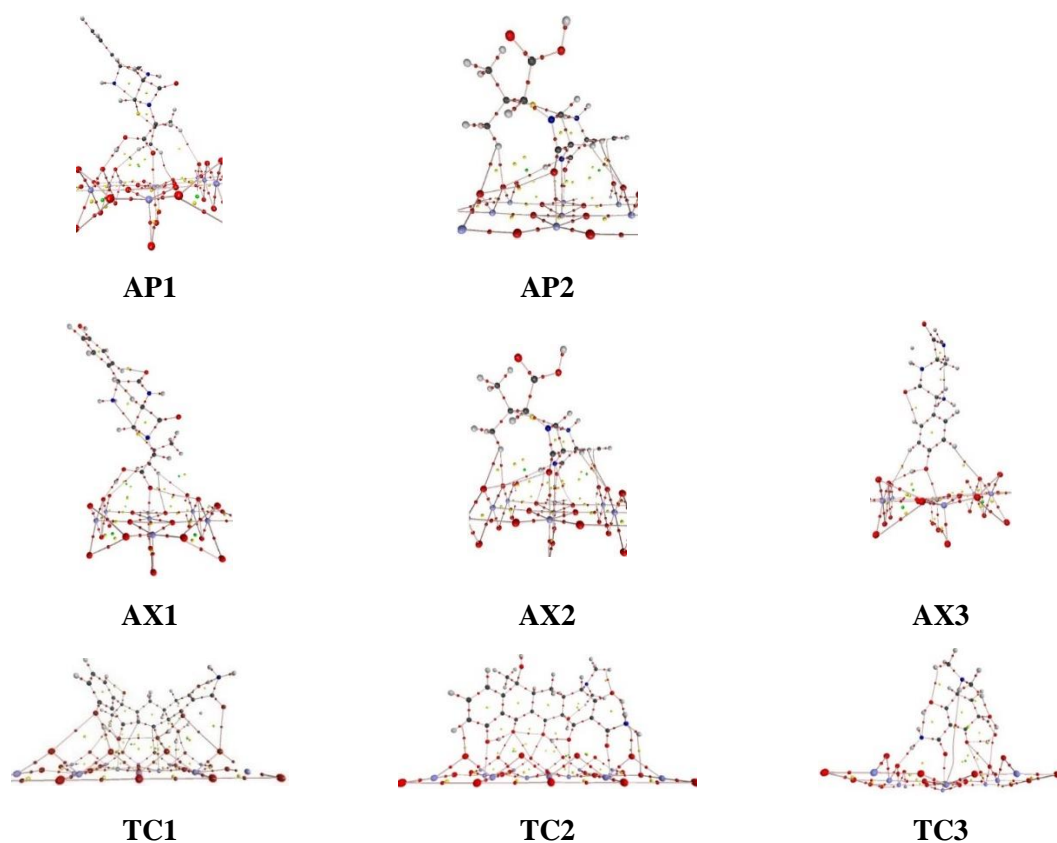


Figure S4. Topological analysis for complexes at B3LYP/6-31G(d,p) level.

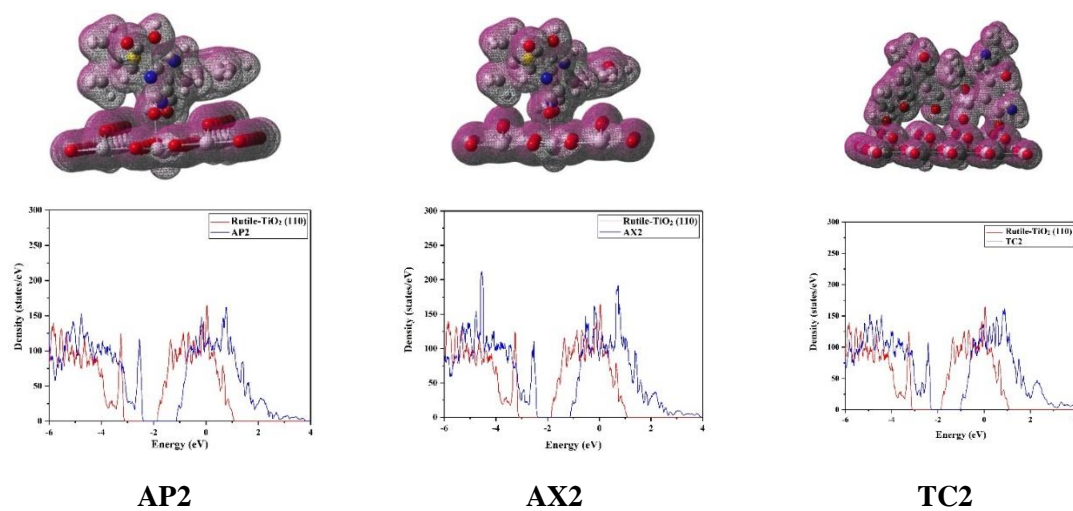


Figure S5. The total electron density transfer (EDT) and density of states (DOS) for the most stable configurations.

Tables:**Table S1.** Some parameters of the optimized structures for the molecules and r-TiO₂ (110) surface.

	C-H	N-H	O-H	C=O	C-S(F)	C-N	C-C
AP	1.09-1.10	1.02-1.02	0.98	1.22-1.36	1.82/1.87	1.40-1.47	1.40-1.58
	<i>1.09-1.10</i>	<i>1.02</i>	<i>0.98</i>	<i>1.21-1.36</i>	<i>1.83/1.86</i>	<i>1.36-1.47</i>	<i>1.38-1.54</i>
AX	1.09-1.10	1.02-1.02	0.97/0.981	1.22-1.36	1.82-1.87	1.40-1.47	1.40-1.58
	<i>1.09-1.10</i>	<i>1.02</i>	<i>0.97/0.98</i>	<i>1.21-1.36</i>	<i>1.83/1.86</i>	<i>1.36-1.47</i>	<i>1.38-1.54</i>
TC	1.09-1.11	1.02/1.02	0.97-1.02	1.22-1.46		1.41-1.48	1.37-1.58
	<i>1.09-1.10</i>	<i>1.01/1.02</i>	<i>0.97</i>	<i>1.23-1.43</i>		<i>1.37-1.46</i>	<i>1.34-1.56</i>
	Ti-Oa	Ti-Ob	TiOTi	OTiO			
		1.83		79.6			
	1.86	<i>1.79±0.09</i>		<i>81±7</i>			
	<i>1.84±0.03</i>	<i>1.87±0.03</i>	109.6	<i>80±2</i>			
	<i>1.85±0.02</i>	1.98	<i>106±2</i>	99.8			
r-TiO ₂	2.12	<i>1.92±0.08</i>	128.8	<i>101±3</i>			
(110)	(duoi)	<i>1.97±0.03</i>	<i>128±4</i>	<i>97±2</i>			
	<i>2.06±0.07</i>	2.07	<i>131±2</i>	99.1			
	<i>2.07±0.03</i>	<i>2.08±0.13</i>		<i>101±6</i>			
		<i>1.97±0.05</i>		<i>98±2</i>			

(*italic values are taken from the experiment in ref.46 and PubChem online*)

Table S2. Proton affinity (PA) at O atoms and de-protonation enthalpy (DPE, without re-optimization) of C/N/O-H bonds of molecules involved in interactions, all values are given in kcal.mol⁻¹.

PA	O _i /O _{ii(ii')} (for -OH)	O ₁ /O ₂ /O ₃ (for >C=O _{1/2/3})		
Amoxicillin	<i>183.0/184.8</i>	<i>200.6/216.2</i>		
Ampicillin	<i>182.8</i>	<i>200.3/215.6</i>		
Tetracycline		202.5-235.1		
DPE	O _i /O _{ii(ii')-H}	N-H	C-H	
Amoxicillin	<i>333.6/351.4</i>	<i>355.7</i>	<i>389.7</i>	
Ampicillin	<i>333.4</i>	<i>355.4</i>	<i>389.5</i>	
Tetracycline	333.1-359.0	344.2	362.1-391.9	

(^{1,2,3} for O atoms assigned in Figures 2,3,5; ^{i,ii(ii')} for O atoms in -COOH and -OH groups, respectively; *italic values is taken from ref.34*)

Table S3. The topological analysis of complexes at B3LYP/6-31G(d,p) level.

	BCPs	$\rho(\mathbf{r})$	$\nabla^2(\rho(\mathbf{r}))$	H(r)		BCPs	$\rho(\mathbf{r})$	$\nabla^2(\rho(\mathbf{r}))$	H(r)	
AP1	O...Ti	0.060	0.346	0.002	AX3	O...Ti	0.041	0.222	0.005	
	O-H...O	0.078	0.133	-0.030		O-H...O	0.044	0.111	-0.007	
	C-H...O(ch3)	0.009	0.030	0.001		O1...Ti	0.035	0.130	0.000	
	C-H...O2	0.008	0.025	0.001		O2...Ti	0.054	0.273	0.001	
AP2	O...Ti1	0.043	0.225	0.004	TC1	O1-H...O	0.025	0.069	0.000	
	O...Ti2	0.051	0.237	-0.001		C-H...O	0.005	0.018	0.001	
	N-H...O	0.006	0.022	0.001		O2-H...O	0.018	0.061	0.002	
	C-H...O	0.009	0.031	0.002		O1...Ti	0.053	0.286	0.003	
	O...C	0.007	0.024	0.001		O2...Ti	0.017	0.046	0.001	
AX1	O...Ti	0.065	0.378	0.002	TC2	O3...Ti	0.029	0.119	0.002	
	O-H...O	0.069	0.146	-0.022		N-H1...O1	0.007	0.026	0.002	
AX2	O...Ti1	0.043	0.244	0.005		N-H1...O2	0.014	0.053	0.002	
	O...Ti2	0.048	0.258	0.004		O-H...O	0.020	0.057	0.001	
	N-H...O	0.006	0.023	0.001		C-H...O	0.013	0.049	0.002	
	N-H...O2	0.010	0.037	0.002	TC3	O...Ti	0.070	0.367	-0.004	
	C-H...O	0.009	0.031	0.002		N-H...O	0.051	0.152	-0.008	
	C-H...O2	0.006	0.023	0.001						
	O...C	0.007	0.023	0.001						
	C-H...O3	0.005	0.020	0.001						

^{1,2}- for O atoms in >C=O and -COOH groups

2/ Section 2.5. From paper 'A molecular level insight into adsorption of β -lactam antibiotics on vermiculite surface', *Surface Science*, 2020, 695, 121588(1-8).

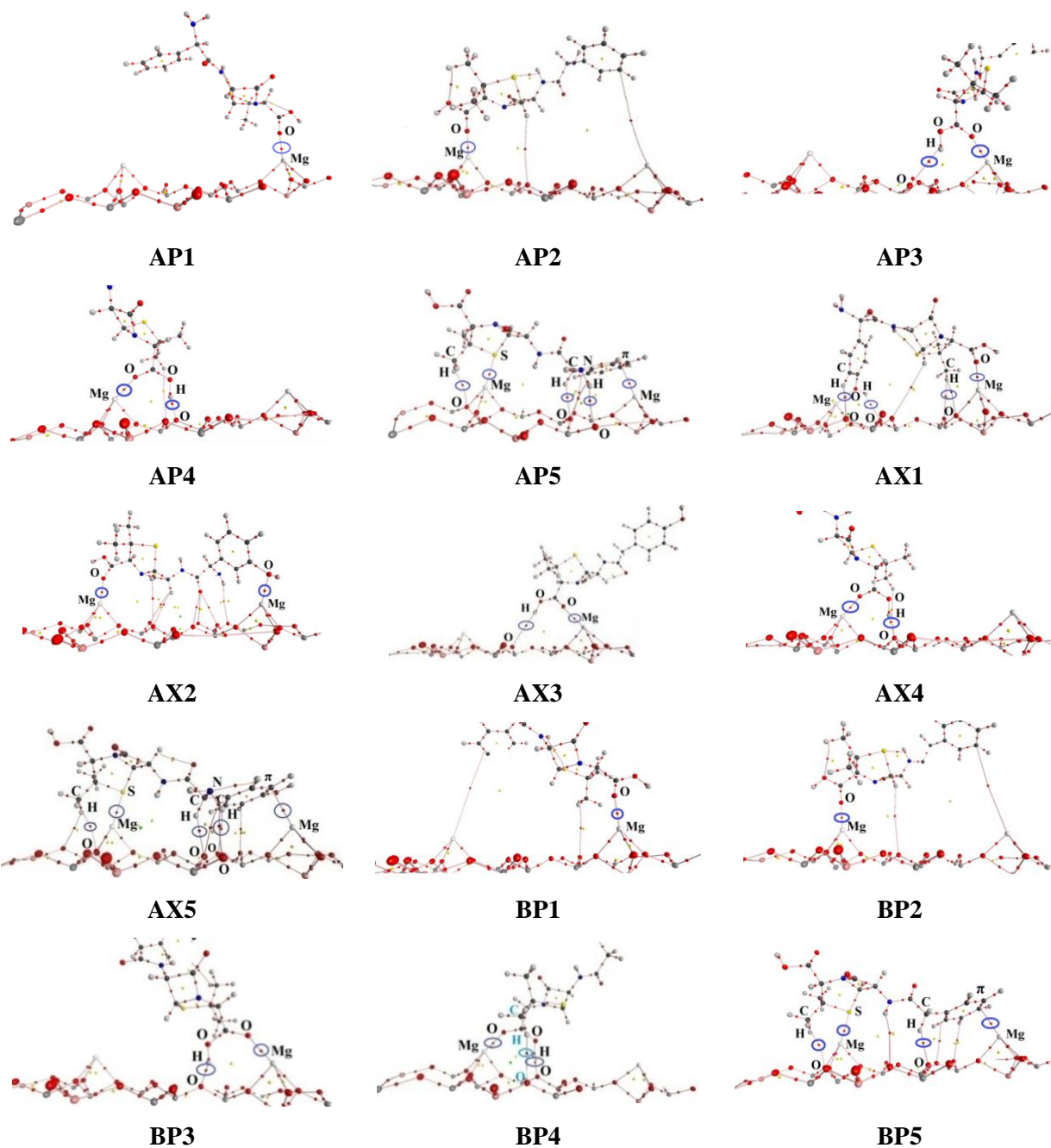


Figure S6. Topological features of all first layered structures.

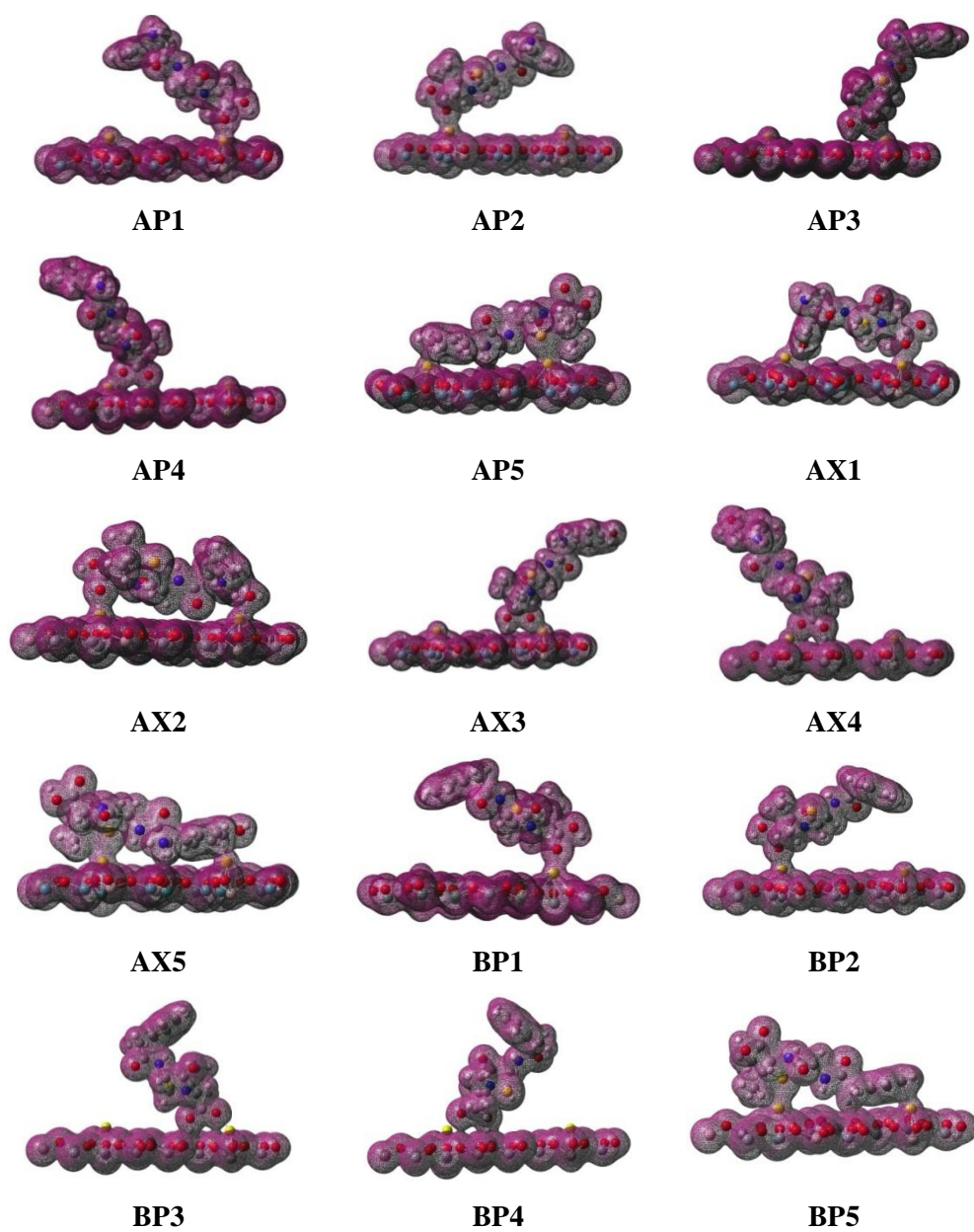


Figure S7. Total electron density maps of all first layered configurations (isovalue = $0.01 \text{ au}/\text{\AA}^3$).

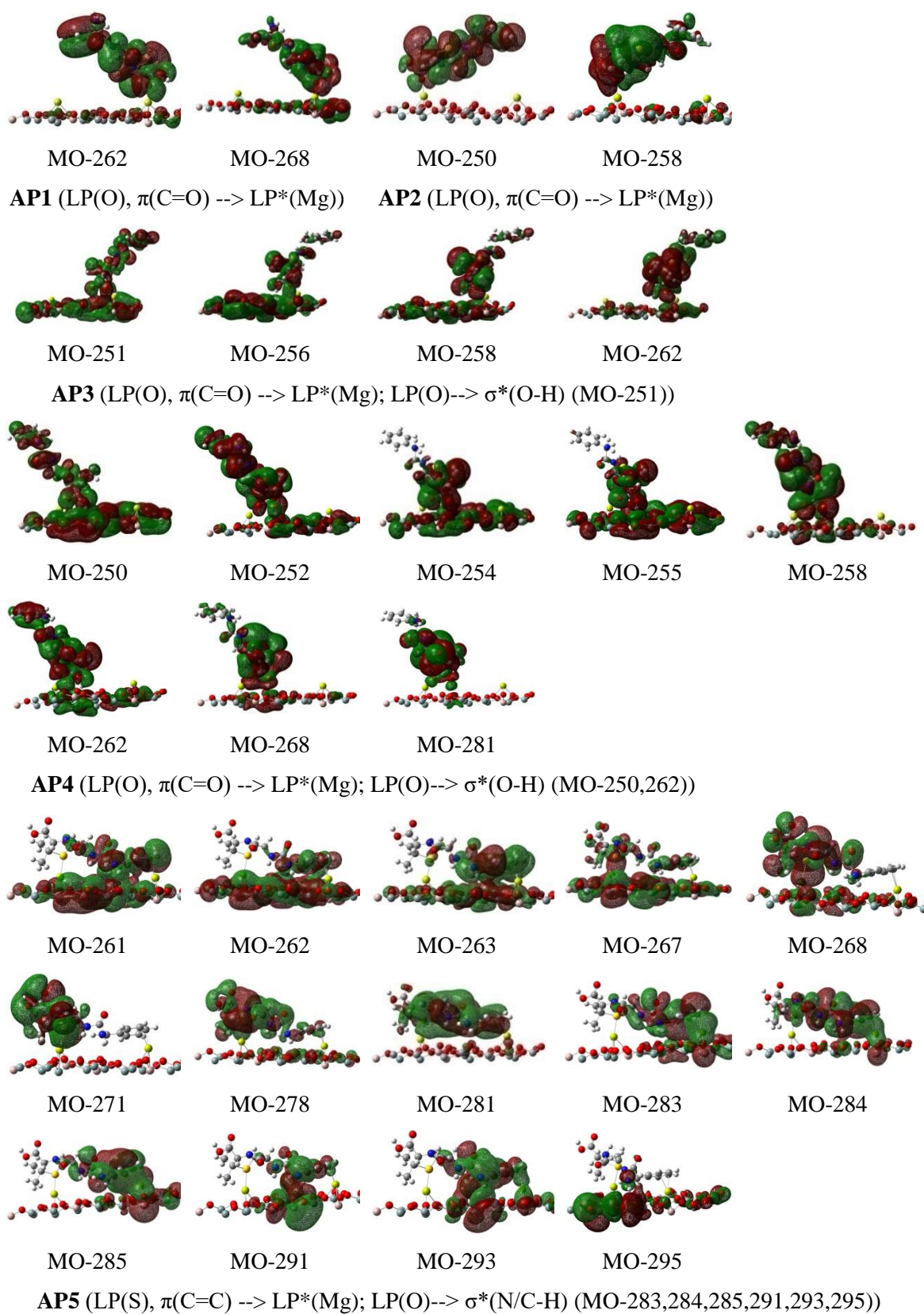


Figure S8. MOs specifying the formation of interactions in complexes observed for AP system (isovalue = 0.005 au/Å³) (*HOMO is MO-310*)

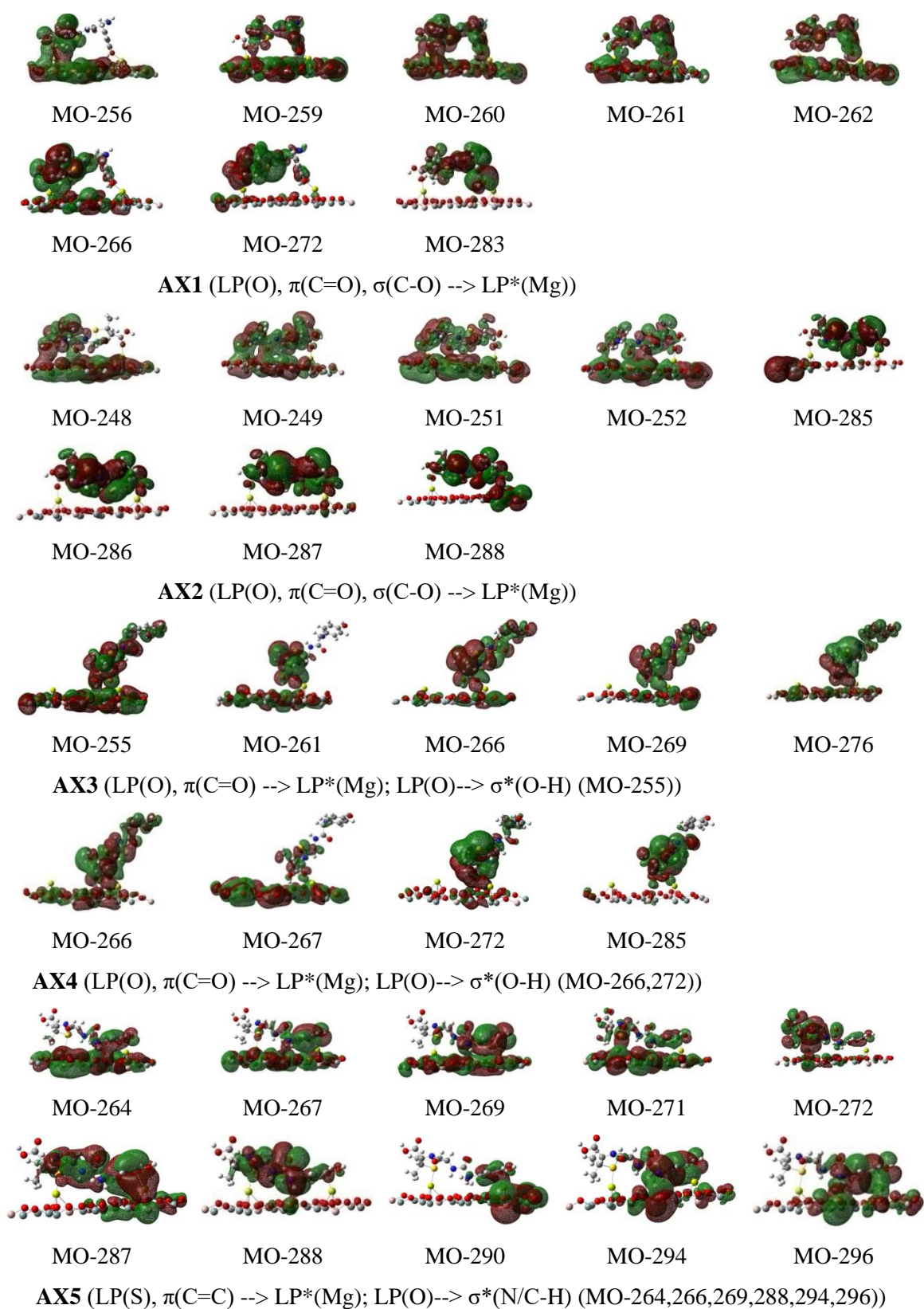


Figure S9. MOs specifying the formation of interactions in complexes observed for AX system (isovalue = 0.005 au/Å³) (HOMO is MO-314).

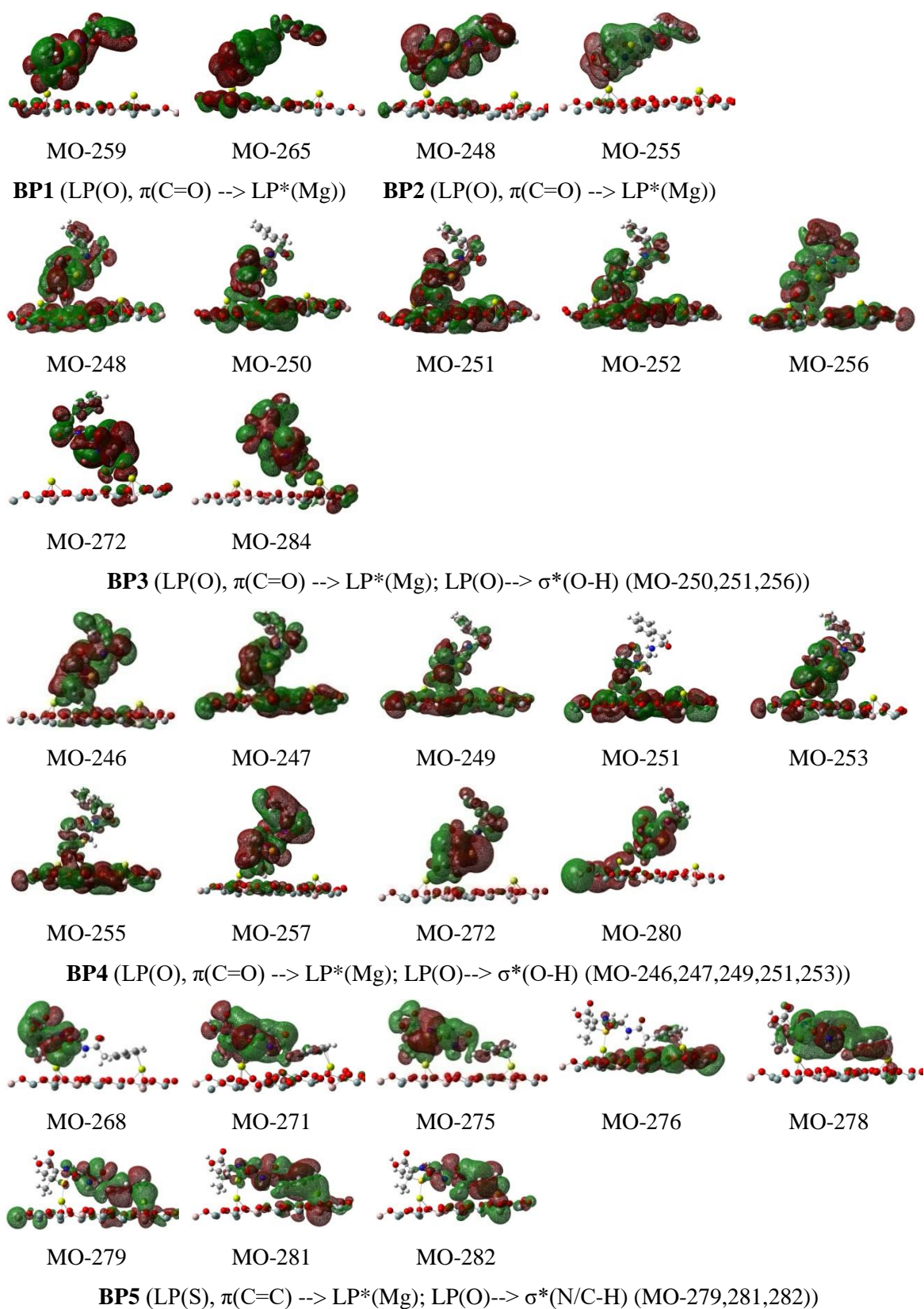


Figure S10. MOs specifying the formation of interactions in complexes observed for BP system (isovalue = 0.005 au/Å³) (*HOMO* is MO-306).

Table S4. Topological analysis at the bond critical points (BCPs) (10^{-3} au), hydrogen bonding energy (kcal.mol⁻¹) and total electron density transfer (EDT, 10^{-3} electron) of **AP** complexes.

	BCP	$\rho(\mathbf{r})$	$\nabla^2(\rho(\mathbf{r}))$	$\mathbf{H}(\mathbf{r})$	\mathbf{E}_B	EDT
AP1	Mg \cdots O	42.0	356.3	15.1		41.8
AP2	Mg \cdots O	45.7	407.1	17.2		39.8
AP3	Mg \cdots O	47.1	416.8	17.1		36.0
AP4	Mg \cdots O	52.2	464.2	17.7		-70.8
	O-H \cdots O	75.9	127.1	-28.4	-27.8	
	Mg \cdots S	31.3	131.8	2.0		
AP5	C-H ^{a)} \cdots O	9.4	35.7	0.9	-1.4	155.1
	C-H ^{b)} \cdots O	13.9	47.6	1.7	-2.7	
	N-H \cdots O	9.6	35.4	1.7	-1.7	
		11.2	36.1	1.4	-2.0	
	C \cdots O	7.6	27.3	1.4		
	Mg \cdots C/ π	25.0	99.4	2.2		

a),b) for H atoms in $-CH_3$ and $-CH$ groups**Table S5.** Topological analysis at the bond critical points (BCPs) (10^{-3} au), hydrogen bonding energy (kcal.mol⁻¹) and total electron density transfer (EDT, 10^{-3} electron) of **AX** complexes.

	BCP	$\rho(\mathbf{r})$	$\nabla^2(\rho(\mathbf{r}))$	$\mathbf{H}(\mathbf{r})$	\mathbf{E}_B	EDT
AX1	Mg \cdots O*	49.0	396.8	14.2		61.5
	Mg \cdots O**	46.0	411.0	17.3		
	Mg \cdots O*	45.0	387.1	15.9		
AX2	Mg \cdots O**	39.2	281.6	10.5		75.3
	O \cdots O	8.8	31.8	1.6		
AX3	Mg \cdots O	42.4	358.1	15.0		31.7
AX4	Mg \cdots O	52.2	463.4	17.7		-71.4
	O-H \cdots O	76.3	126.4	-28.9	-28.0	
	Mg \cdots S	31.9	134.7	2.0		
	C-H ^{a)} \cdots O	8.8	24.6	1.0	-1.3	
	C-H ^{b)} \cdots O	13.9	47.7	1.7	-2.7	
AX5	N-H \cdots O	9.6	32.5	1.5	-1.6	25.4
		9.7	35.8	1.7	-1.7	
	Mg \cdots C/ π	27.0	108.4	2.0		
	C \cdots O	8.4	28.7	1.4		

a),b) for H atoms in $-CH_3$ and $-CH$ groups; ** for O atoms in $-C=O/-COOH$, $-OH$ groups

Table S6. Topological analysis at the bond critical points (BCPs) (10^{-3} au), hydrogen bonding energy (kcal.mol^{-1}) and total electron density transfer (EDT, 10^{-3} electron) of **BP** complexes.

	BCP	$\rho(\mathbf{r})$	$\nabla^2(\rho(\mathbf{r}))$	$\mathbf{H}(\mathbf{r})$	\mathbf{E}_B	EDT
BP1	Mg \cdots O	42.2	358.3	15.2		41.8
BP2	Mg \cdots O	45.7	406.9	17.2		38.0
BP3	Mg \cdots O	46.9	388.8	14.9		-50.0
	O-H \cdots O	63.7	146.4	-17.0	-22.1	
BP4	Mg \cdots O	51.5	443.4	16.5		-69.1
	O-H \cdots O	77.0	126.9	-29.4	-28.4	
	C-H \cdots O	6.1	22.0	1.2	-0.9	
	Mg \cdots S	31.2	131.0	2.0		
BP5	C-H ^{a)} \cdots O	9.5	25.9	0.9	-1.4	160.1
	C-H ^{b)} \cdots O	14.3	48.0	1.6	-2.8	
	Mg \cdots C/ π	24.4	96.6	2.2		
	C \cdots O	7.6	27.0	1.4		

^{a),b)} for H atoms in $-\text{CH}_3$ and $-\text{CH}$ groups